University of California
Berkeley
Seismological Laboratory

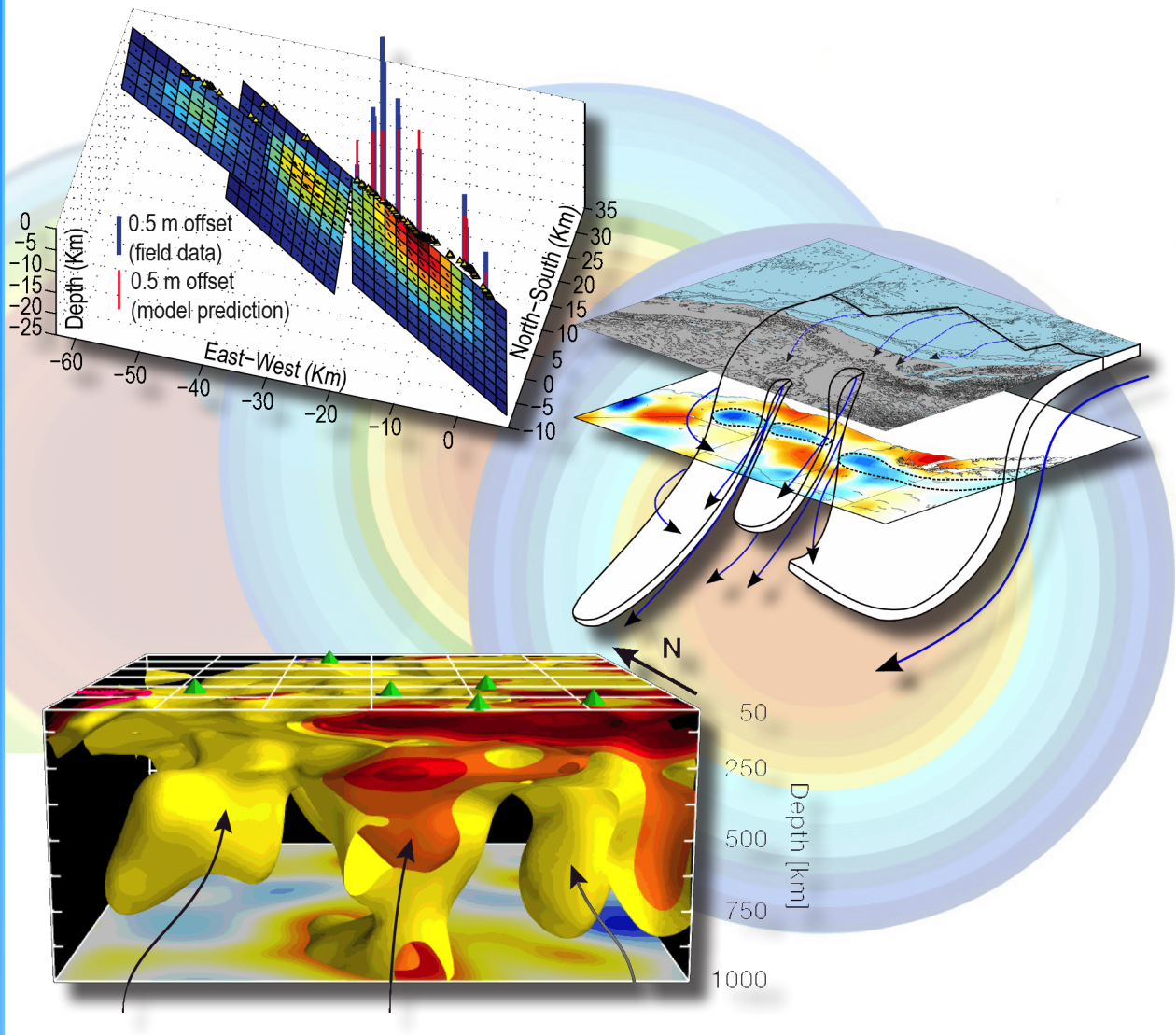

Annual Report

July 2012–June 2013

Berkeley Seismological Laboratory

Annual Report
July 2012—June2013

University of California
Berkeley
Seismological Laboratory

Contents

Chapter 1

Director's Report

Highlights

It is a great pleasure to present this year's Berkeley Seismological Laboratory (BSL) Annual Report. It is exhilarating to be reminded of the wide range of BSL activities, as captured in these pages. The BSL today fosters both an active solid Earth research program and a cutting-edge geophysical observing facility. Spanning both of these realms, BSL provides an environment in which the extramural research program is strengthened and broadened by the facility, and the facility continues to push the boundaries of terrestrial observations in response to research needs. In addition, the BSL continues to reach out and connect with the consumers of our data and our science. These include students, the public, and private or public sector institutions with a need and desire for an improved understanding of solid Earth processes. The contributions to this report are divided along these three lines. The research accomplishments are covered in Chapter 2, outreach efforts to broaden engagement are in Chapter 3, and progress in the development of our facilities is contained in Chapter 4. But first, I would like to highlight some of this year's activities.

Chapter 2 of the report contains 34 research summaries highlighting ongoing projects. In this year's report we have encouraged the submission of contributions from a broader spectrum of the BSL's 18 affiliated faculty and their students. The topics the summaries report on fall into five broad categories:

1. The mineral physics section includes experimental and numerical experiments on the properties of minerals found in the Earth's crust and beyond, to the cores of Mars and Mercury.

2. The Earth structure section includes new models of North America. Some focus on the old geologic and tectonic structures that underlie the eastern US. Others describe investigations of the actively deforming western US, including flow through the segmented Juan de Fuca plate. Other Earth structure studies model mantle flow beneath the oceans, including upwelling hotspots and anisotropy at the base of the mantle; and the structure of permafrost zones. Finally, this section also describes the development of new imaging techniques.

3. The rheology and fault mechanics section includes studies of lithospheric rheology based on the deformation induced by large earthquakes; studies of temporal changes in active geothermal regions; monitoring and modeling of landslide processes; and the detection of temporal changes in fault zone properties.

4. In the seismic source section, new techniques to characterize underground explosions are developed along with a study of the seismic characteristics of a sinkhole. Earthquake sources in the Geysers geothermal region are also investigated.

5. The final group of research papers focuses on efforts to enhance our observational systems. This includes the installation of a borehole plus surface instrument network to study tremor on the San Andreas Fault; a signal enhancement technology for OBS stations; and the ongoing development of a smartphone-based seismic network. Significant effort to design and build an earthquake early warning system is also covered in this section with papers on both seismic and GPS-based techniques; the design of optimal networks; the use of arrays to track large earthquakes; and a summary describing California's demonstration warning system.

Many of these research efforts are stimulated and inspired by our facilities. These include our geophysical networks that continuously collect a variety of data from across northern California, and the data center (http://www.ncedc.org/) that delivers the data to researchers around the world and within the BSL. More information about these networks and their development can be found in the Facilities Review below. Here I would like to note some key developments this year.

Our instrumentation along the San Andreas Fault in central California continues to play a key role in studies of earthquake fault processes conducted by researchers around the world. Data from the High Resolution Seismic Network (HRSN) located near Parkfield, California is highly used placing this network at the center of faulting studies. A high-profile Nature paper links laboratory results of fault healing to naturally occurring microearthquakes using data from the HRSN (*McLaskey et al.*, 2012). Other research efforts, both national and international, continue to rely on HRSN data for a variety of investigations including finite source modeling and scaling (BSL), tracking of repeating events (US Geological Survey, BSL), understanding the relationship between nonvolcanic tremor and low frequency earthquakes (ETH Zurich), ETAS forecasting and prediction modeling of recurrent earthquakes (Japan), and testing of forecasts/predictions with ongoing repeating microearthquakes (BSL, ETH Zurich). In response to the scientific opportunities presented along this section of the San Andreas Fault we are also expanding our network in the region with the development of "Tremorscope". This is a combined borehole and surface station network currently under construction by the BSL just south of the HRSN designed to focus in on the low amplitude seismic tremor that has been detected along the fault by the HRSN. This year the surface stations were completed and we anticipate drilling the borehole stations in the coming year.

Following the upgrade of our Bay Area Regional Deformation Network (BARD) last year, we have also made substantial progress in our real-time processing of these continuous high-accuracy GPS stations. For several years the data have been processed automatically to produce "daily time series". This is a procedure in which the one sample per second data

are combined with other information to provide a single average position for the day. This allows tracking of plate movement and other slow surface deformation caused by a variety of processes including land-use subsidence, landslides and aquifer inflation and deflation. The data are now also being processed much more rapidly in order to provide real-time information about earthquakes. Firstly, "Earthquake Rapid Response" processing is triggered by moderate and large earthquakes. One to two minutes of data are first accumulated following the earthquake. They are then processed to provide high accuracy position changes which can be used in a non-linear inversion for the size, orientation and distribution of slip on the active fault plane. This information, available within about five minutes, can then be used to improve the quality of ShakeMaps generated for the event. Secondly, inclusion of GPS data in the Earthquake Early Warning system is well underway. This processing proceeds even more rapidly so that information about large earthquakes can be extracted within seconds. The development of the G-larmS module that uses GPS data and complements the ElarmS seismic-based alerts is well underway and is expected to become operational next year.

This year's report includes a new chapter on "broadening engagement". This reflects the increase in activities at the BSL to reach out and engage with a broad spectrum of society interested in the data products and research efforts at the lab. With the addition of our new External Relations Officer, Dr Jennifer Strauss, to the BSL staff in November 2012, the lab has been able to increase the efforts of the Earthquake Research Affiliates (ERA) Program (http://earthquakes.berkeley.edu/ERA/). This program focuses on engaging public and private institutions with an interest in the development of new earthquake information products and research. Current members include the Bay Area Regional Transit (BART) District, Google, San Francisco's Department of Emergency Management, the UC Berkeley Police Department, and Deutsche Telekom's Silicon Valley Innovation Center. BART now uses our earthquake early warning feed to slow and stop trains automatically during earthquakes, while Deutsche Telekom is working with us on the development of smartphone seismic networks. The other groups are primarily interested in making use of earthquake early warning feeds and are currently in the process of identifying how they would make use of the feed. The BSL is also now better represented within the emergency response community as Strauss participates in conferences and exercises, including this year's Golden Guardian exercise that focused on a major earthquake in Northern California.

BSL's other efforts to broaden engagement are focused on the public. During this year the BSL developed a new webpage that is more focused on information for the public, while still providing information about BSL activities for the research community. The pages are now available at the URL http://earthquakes.berkeley.edu, which is hopefully easier for the public to remember than our http://seismo.berkeley.edu URL (which remains active). The front page shows a realtime map of earthquakes in California and zooms to the most recent significant earthquake reported. In addition, the BSL has a iOS (iPhone/iPad) app called MyQuake that delivers realtime earthquake information to users as well, and also provides information about past earthquakes in an effort to inform the public about the likely impact of future events. MyQuake is available for free at the iTunes store. Additional activities include public lectures, CalDay activities, tours, new displays at the BSL, a new art exhibit based on the real-time seismic data feed from the lab called Bloom, and new "Science on a Sphere" exhibits being developed in collaboration with the Lawrence Hall of Science.

Finally, during this year the BSL has been participating in the development of new Legislation in California relating to the development of a public earthquake early warning system. The legislation, know as Senate Bill 135, was introduced by Senator Alex Padilla in January 2013. Several members of the BSL participated in press conferences, in briefings for legislators, and in Senate and Assembly hearings on the legislation since its introduction. The bill passed the California Senate on May 28th, 2013, the Assembly on September 12th, 2013 and was signed into law by Governor Jerry Brown on September 24th, 2013. In addition to calling for a public state-wide warning system and naming the University of California as one of the participants, this is the first legislation in California that requires the state to play a role in monitoring earthquake activity. There is still much work to be done, however, as the legislation provides no funding. Instead, it calls on the Governor's Office of Emergency Services to develop plans for a system and to identify sources of funding. The BSL will continue to contribute to this development. More next year.

BSL Personnel News

Three new PhD graduate students joined the lab during the 2012/13 academic year: Meng Cai, Avinash Nayak, and Katie Wooddell. Also, two Postdoctoral Fellows joined: Ronni Grapenthin and Lingsen Meng. Five PhD student graduated, their names and thesis titles were: Holly Brown, "Evaluating and Improving the ElarmS Earthquake Early Warning Algorithm"; Sanne Cottaar, "Heterogeneity and Flow in the Deep Earth"; Rob Porritt, "Tracing the Farallon plate through seismic imaging with USArray"; Amanda Thomas, "Fact or Friction: Inferring Rheology from Nonvolcanic Tremor and Low-Frequency Earthquakes on the Deep San Andreas Fault"; and Kelly Wisemann, "The Far Reach of Megathrust Earthquakes: Evolution of Stress, Deformation and Seismicity Follwing the 2004 Sumatra-Andaman Rupture".

The BSL also continued to provide a range of research projects for undergraduate students. This year's cohort consisted of Rohan Agarwal, Cora Bernard, Voon Hui Lai, Kimberly Lin, Robert Martin-Short, Irene Munafo, and Michael Tran.

As usual, a stream of visitors spent varying amounts of time at the lab. These included Jamie Barron, Pierre Clouzet, Frances Leiva, Florian Rickers, and Sergi Ventosa visiting Barbara Romanowicz's group; Alistair Boyce, Ahyi Kim, and Seung-Hoon Yoo visiting Doug Dreger's group, and Simona Colombelli, William B. Hawley, and Robert Martin-Short visiting my group. One of our former graduate students, Aurelie Guilhem, returned to work with several members of the lab. Finally, Tea Godoladze spent a year at the lab on a Fulbright Fellowship.

During the year we also gained several new members of staff. Sarah Snyder and Nicole Crisosto joined the engineering staff, although Nicole departed towards the end of the year. Jennifer Strauss also joined as our new External Relations Officer. Aaron Enright who was on the engineering staff for several years departed, as did Huaiyu Yuan who was working as a researcher.

Facilities review

The Berkeley Seismological Laboratory (BSL) is an Organized Research Unit (ORU) on the UC Berkeley campus. Its mission is unique in that, in addition to research and education in seismology, geophysics, and earthquake-related science, it is responsible for providing real-time earthquake information. This information is required by the UC Berkeley constituency, various local and state government and private organizations including emergency response, and is consumed by the general public. The BSL is therefore both a research center and a facility/data resource, which sets it apart from most other ORUs. A major component of our activities is focused on developing and maintaining several regional observational networks, and participating, along with other agencies, in various aspects of the collection, analysis, archival, and distribution of data pertaining to earthquakes, while maintaining a vigorous research program on earthquake processes and Earth structure. In addition, the BSL staff spends considerable time on public relations activities, including tours, talks to public groups, response to public inquiries about earthquakes, and an informational web presence.

UC Berkeley installed the first seismograph in the Western Hemisphere at Mount Hamilton (MHC) in 1887. Since then, it has played a leading role in the operation of state-of-the-art seismic instruments and in the development of advanced methods for seismic data analysis and interpretation. Notably, the installation, starting in 1927, of Wood-Anderson seismographs at four locations in Northern California (BKS, ARC, MIN, and MHC) allowed the accurate determination of local earthquake magnitude from which a unique historical catalog of regional earthquakes has been maintained to this day, providing crucial input to earthquake probability studies.

Over the years, the Berkeley Seismographic Stations (BSS), as the BSL was then called, continued to drive technological improvements. The first centrally telemetered network using phone lines in an active seismic region was installed by BSS in 1960. The BSS was the first institution in California to operate a 3-component "broadband" system (1963). It played a major role in the early characterization of earthquake sources using "moment tensors" and source-time functions. The BSS also made important contributions to the early definitions of detection/discrimination of underground nuclear tests and, jointly with UCB Engineering, to earthquake hazards work.

Starting in 1986, the BSS acquired four state-of-the-art broadband instruments (STS-1), while simultaneously developing PC-based digital telemetry. These two developments laid the groundwork for the modern networks we operate today. As telecommunication and computer technologies made rapid progress, in parallel with broadband instrument development, paper record reading was abandoned in favor of automated analysis of digital data. One paper-based helicorder does remain operational, primarily for the press and visitors to view.

Today, the BSL's networks can be divided into three groups of instrumentation that are deployed at a total of ~70 sites across central and northern California. The instrumentation types predominantly consist of broadband plus strong motion seismic, borehole seismic, and GPS equipment, and are often co-located when appropriate. Data from all instrumentation streams continuously into the BSL's real-time monitoring system providing for earthquake warnings, notification and characterization. It is also delivered to the archive where it can be accessed immediately by researchers from around the world for scientific study.

The Berkeley Digital Seismic Network (BDSN) is our regional seismic network of about 40 sites where both broadband and strong motion seismic instrumentation is installed. This network is the backbone of the BSL's operations, feeding the necessary data for real-time estimation of location, size and rupture parameters for earthquakes in central and northern California. This network has been steadily growing since the 1990's and consists of very high quality, low noise sites making the data ideal for a range of research efforts. The array can be used to study local or global earthquake sources, and provides data for investigation of 3D crustal structure in California and its effects on regional waveform propagation, which in turn affect the intensity of ground shaking in larger earthquakes. Recent additions to the network include an ocean bottom seismometer in the Monterey Bay (MOBB) providing real-time data via an undersea cable (operated in collaboration with MBARI), and also the Tremorscope stations along the Cholame section of the San Andreas Fault just south of Parkfield, CA.

The real-time data is also Berkeley's contribution to the California Integrated Seismic Network (CISN), which is a federation of networks that jointly provide all real-time earthquake information in the state. Since 1996, the BSL and the USGS in Menlo Park have closely cooperated to provide the joint earthquake notification program for Northern California. This program capitalizes on the complementary capabilities of the networks operated by each institution to provide rapid and reliable information on the location, size and other relevant source parameters of regional earthquakes. The real-time earthquake information is made available through the BSL's website (http://earthquakes.berkeley.edu).

The BSL's borehole networks represent the second grouping of instrumentation. The High Resolution Seismic Network (HRSN) was installed in 1987 and now consists of 12 operating sites. Additional borehole sites will soon be added as part of the Tremorscope project. These instruments have led to wide-ranging research into earthquake processes due to their high sensitivity, low noise, and proximity to micro-earthquakes, clusters and tremor sources along the highly studied Parkfield section of the San Andreas Fault. In the Bay Area, the Hayward Fault Network also includes 15 borehole instruments that have been installed progressively since the 1990s. Again, the goal of this network is to collect high signal-to-noise data for micro-earthquakes along the Hayward Fault to gain insight into the physics that govern fault rupture and its nucleation.

The third instrumentation type is GPS. The BSL operates the Bay Area Regional Deformation (BARD) Network consisting of 32 primary sites, 18 collocated with BDSN seismometers. All sites record with a 1 Hz sample rate and telemeter the data to BSL in real-time. Continuous GPS data track the motion of the tectonic plates and allows us to assess the strain buildup along faults as well as its release either through creeping episodes or through earthquakes. The application of GPS data feeds to real-time earthquake information is also a relatively new development. Very rapid processing now generates displacement waveforms that in turn support the development of improved real-time earthquake analysis methods for significant earthquakes.

The BSL's IT group is active in the development of new software for the collection, archival and real-time analysis of the various geophysical data streams that we collect. In 2009, the new AQMS seismic network software package was rolled out following a multi-year development effort by the BSL in collaboration with other CISN partners. This software provides all the real-time processing components needed by regional seismic networks and is now being rolled-out across the US. The development of real-time GPS processing software is a current area of focus for the lab along with development and implementation of earthquake early warning algorithms that can process the data quickly enough to provide alerts to people a few seconds to tens of seconds before shaking is felt.

Archival and distribution of data from the BSL and other regional geophysical networks is performed at the Northern California Earthquake Data Center (NCEDC), operated at the BSL in collaboration with USGS Menlo Park. The data reside on a mass-storage device (current holdings ~70 Tb), and are accessible online (http://www.ncedc.org). In addition to BSL network data, data from the USGS Northern California Seismic Network (NCSN), and other northern California networks, are archived and distributed through the NCEDC. The NCEDC also maintains, archives and distributes various earthquake catalogs.

Finally, the field engineering team is responsible for maintaining our existing ~70 geophysical observatories across Northern California, and designing and installing new sites. Of particular note is the completion in 2011 of the ARRA-funded upgrades. These urgently needed equipment upgrades replaced aging dataloggers at almost all BSL observatories providing for more robust and more rapid transmission of data from the sites to the BSL real-time system. The group is now focused on the design and installation of the new Tremorscope borehole and surface stations just south of Parkfield along the Cholame section of the San Andreas Fault, and on upgrading the HRSN.

All of these operations are supported by an operations and research staff of 9, an IT staff of 7, an engineering staff of 3, and an administrative support group largely shared with the Department of Earth and Planetary Science consisting of 7. In addition, there are currently 6 Postdoctoral Scholars and 15 PhD graduate students associated with the lab, along with 18 affiliated faculty.

Core University funding to our ORU provides salary support for one staff scientist (shared by three researchers), one IT staff member, one engineer, our operations manager, and two administrative assistants, and represents about one fifth of the total infrastructure support budget. The remaining support comes from extramural grants and contracts, primarily from the USGS, DOE, NSF, and the State of California, through its Office of Emergency Services (CalOES). Currently, grants from the Gordon and Betty Moore Foundation contribute significantly to our operations as do the contributions from the members of our Earthquake Research Affiliates (ERA) Program. Additional extramural research funding to BSL affiliated faculty and staff conducting earthquake science more than doubles the total annual budget.

Acknowledgements

I would like to thank our technical and administrative staff, scientists and students for their efforts throughout the year and their contributions to this annual report. In particular I would like to thank our affiliated faculty, whose research groups are contributing to this report for the first time: Professors Steven Glaser, Raymond Jeanloz, Burkhard Militzer and Rudy Wenk. Individual contributions to activities and report preparation are mentioned in the corresponding sections, except for the appendix sections, which were prepared by Clay Miller.

The BSL Advisory Committee plays an important role providing feedback and guidance on BSL activities and priorities. The committee members are Prof. Steven Glaser (Chair – Civil and Environmental Engineering, UC Berkeley), Prof. Josh Bloom (Astronomy, UC Berkeley), Dr. Thomas Brocher (US Geological Survey), Prof. Michael Manga (Earth and Planetary Science, UC Berkeley), Prof. John Vidale (University of Washington). In particular I would like to thank them for their participation in the Advisory Meeting in June 2013 and the thoughtful preparation of the report that followed.

I also wish to especially thank the individuals who have regularly contributed to the smooth operation of the BSL facilities: Mario Aranha, Nicole Cristosto, Doug Dreger, Aaron Enright, John Friday, Peggy Hellweg, Ivan Henson, Ingrid Johanson, Clay Miller, Josh Miller, Pete Lombard, Bob Nadeau, Doug Neuhauser, Charley Paffenbarger, Jennifer Strauss, Sarah Snyder, Jennifer Taggart, Taka'aki Taira, Stephen Thompson, Bob Uhrhammer, and Stephane Zuzlewski, and, in the administrative office, Marion Banks, Matt Carli, Judith Coyote, Clarissa Foreman, Dawn Geddes, Raluca Iordache, and Gretchen von-Duering.

I am particularly grateful to Clay Miller, Jennifer Taggart and Peggy Hellweg for their help in putting together this annual report and bringing it to completion.

The Annual Reports of the Berkeley Seismological Laboratory are available on the web at http://earthquakes.berkeley.edu/annual_report.

Chapter 2

Research Studies

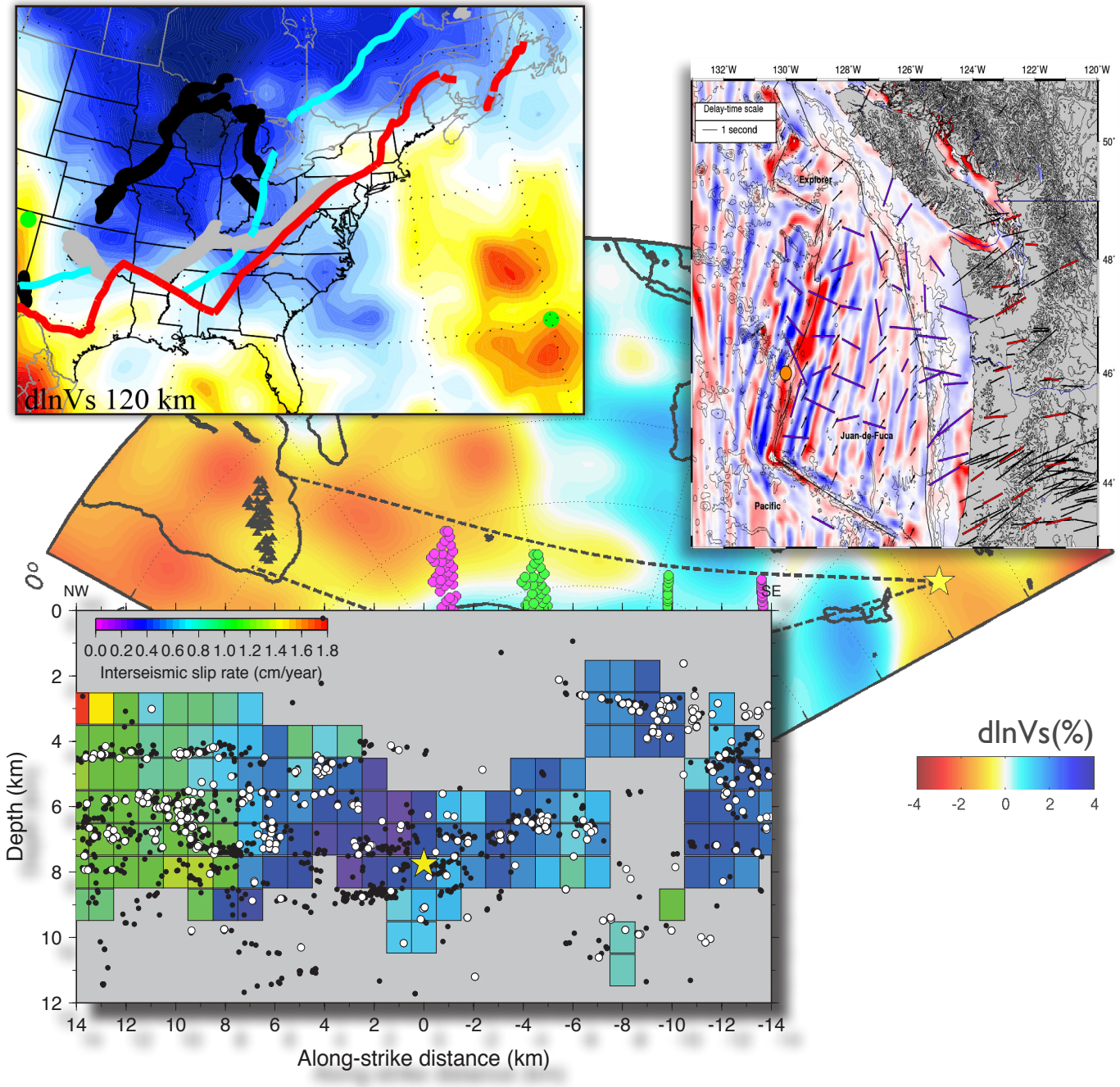

1 *Ab Initio* Calculations of Elastic Constants of Plagioclase Feldspars

Pamela Kaercher, Burkhard Militzer, Hans-Rudolf Wenk

Introduction

Plagioclase feldspars are one of the most important rock-forming minerals, comprising roughly 40% of the Earth's crust. Their elastic properties are essential for interpreting seismic data to determine the structure and deformation history of the Earth's crust, especially the seismically anisotropic lower crust. This anisotropy has been largely attributed to preferred orientation of plagioclase and orientation patterns have been investigated with advanced methods (*e.g., Ji and Mainprice,* 1988, *Seront et al.*, 1993) including work at Berkeley(*e.g., Xie et al.*, 2003, *Feinberg et al.*, 2006, *Gómez-Barreiro et al.*, 2007). However, to relate crystal orientation patterns to macroscopic seismic anisotropy, we need the elastic properties of plagioclase single crystals, which are not completely known.

Nearly all of the existing elastic constants for plagioclases (*e.g., Alexandrov and Ryzhova,* 1962, *Ryzhova,* 1964) were measured in highly twinned polycrystals, generating monoclinic symmetry for the truly triclinic plagioclase crystals. Only recently, *Brown et al.* (2006) measured velocities on untwinned albite and retrieved all 21 elastic constants to fully describe triclinic symmetry.

We have performed *ab initio* calculations using density functional theory to calculate elastic constants for albite $NaAlSi_3O_8$ (An0), andesine/laboradorite $NaCaAl_3Si_5O_{16}$ (An50), and anorthite $CaAl_2Si_2O_8$ (An100) in order to assess and improve upon the precision of existing elastic constants.

Method

We calculated the elastic constants of An0, An50, and An100 with density functional theory using the local density approximation within the Vienna *Ab-initio* Simulation Package (VASP). We used the finite strain approach with the experimentally-determined density (*e.g., Militzer et al.,* 2011) and calculated elastic constants (C_{ijkl}) with Hooke's Law.

The lattice vectors of the unit cells $(\vec{a},\vec{b},\vec{c}) \equiv \vec{A}$ were strained by $\vec{A'} = (\vec{I} + \vec{\varepsilon_i})\vec{A}$, where $\vec{I}$ is the identity matrix, and $\vec{\varepsilon_i}$ is the strain matrix, where the three diagonal (i = 1,2,3) and three off off-diagonal (i = 4,5,6) strain tensors are defined similarly to

$$\vec{\varepsilon_1} = \begin{pmatrix} \delta & 0 & 0 \\ 0 & 0 & 0 \\ 0 & 0 & 0 \end{pmatrix} \text{ and } \vec{\varepsilon_4} = \begin{pmatrix} 0 & 0 & 0 \\ 0 & 0 & \delta/2 \\ 0 & \delta/2 & 0 \end{pmatrix},$$

with δ = ±0.005, to define new lattice vectors $(\vec{a'},\vec{b'},\vec{c'}) \equiv \vec{A'}$.

We estimate total errors in elastic constants to be < ±2 GPa based on comparison of differences between C_{ij} and C_{ji} values and observations of the effect of different values of δ on elastic constants.

Results and Discussion

Most of our computed elastic constants for An0 are higher than those of *Ryzhova* (1964) and lower than those of *Brown et al.* (2006), but tend to be closer to those of *Brown et al.* (Figure 2.1.1). Our calculated An50 elastic constants are comparable to those of both *Alexandrov and Ryzhova* (1962) and *Ryzhova* (1964).

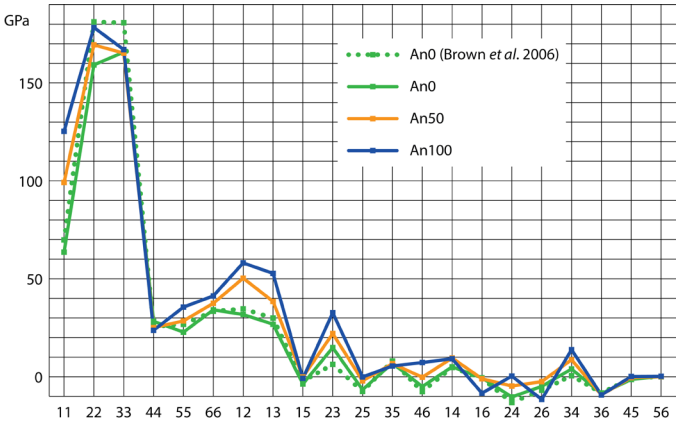

Figure 2.1.1: Comparison of measured An0 (*Brown et al.,* 2006) and computed An0, An50, and An100 elastic constants in gigapascals (GPa). The horizontal axis shows subscripts for elastic constants in Voigt notation.

Elastic properties and mineral density may be used to calculate wave velocities in different directions through a single crystal. *P*-wave and *S*-wave velocity maps (Figure 2.1.2) show seismic anisotropy generally decreases as An0 → An100, likely due to changes in bond lengths as Al substitutes in for Si, which in turn cause tetrahedra (with oxygen at the four corners and either Al or Si in the center cation position) to rotate. Specifically, *P*-wave velocity anisotropy (A_p) for our calculated An0, An50, and An100 is 39%. 26%, and 28%, respectively, where $A_P = \frac{V_{max} - V_{min}}{V_{max}} \times 100\%$. In comparison, other deep crustal minerals such as olivine and hornblende are 22% and 28%, respectively.

Elastic constants may also be combined with the orientation distribution of a polycrystal to model seismic anisotropy for a rock with preferred orientation. The relationship between preferred orientation and seismic velocities has been studied in a number of natural aggregates with high plagioclase content (*e.g., Wenk et al.*, 1986, *Ji and Mainprice,* 1988), which found that *P*-wave anisotropy in plagioclase amounts to 2-15% depending on the fabric, suggesting that an accurate and complete set of C_{ij}s for the plagioclase series is important for calculating seismic velocities through the lower mantle.

Summary

The 21 elastic constants were calculated for An0, An50, and An100 using DFT. Results for An0 and An50 agree well with experimental results. In addition we calculated C_{ij}s for An100, and results can be extrapolated for the entire plagioclase family. These C_{ij}s can be applied to model anisotropy of plagioclase-containing rocks, and are particularly useful to improving velocity calculations through the lower crust.

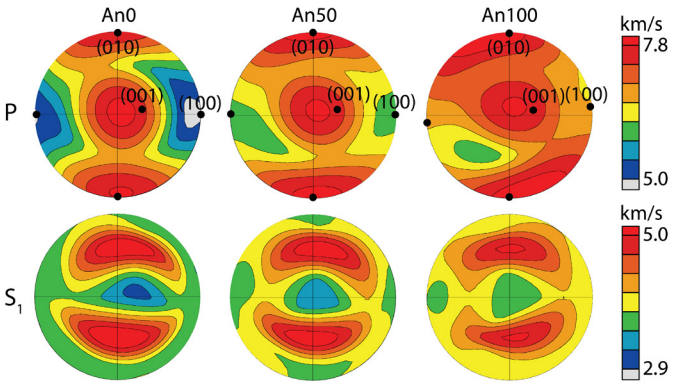

Figure 2.1.2: Velocity surface maps calculated from densities and the elastic constants calculated for An0, An50, and An100. The top row shows are P-wave velocities, and the bottom row shows fastest S-wave velocities. These are equal area projections.

Acknowledgements

P. Kaercher is grateful to Siegfried Matthies and Roman Vasin for help with this work. We also thank the Carnegie/Department of Energy Alliance Center (CDAC) for financial support.

References

Alexandrov, K.S., Ryzhova, T.V. , Elastic properties of rock-forming minerals: III feldspars, *Bull. Acad. Sci. USSR Geol. Ser. 10*, 129-131., 1962.

Brown, J.M., Abramson, E.H., Angel, R.J., Triclinic elastic constants forlow albite, *Physics and Chemistry of Minerals 33*, 256-265, 2006.

Feinberg J., Wenk H.-R., Scott G.R., Renne P.R., Preferred orientation and anisotropy of seismic and magnetic properties in gabbronorites from the Bushveld layered intrusion, *Tectonophysics, 420*, 345-356, 2006.

Gómez-Barreiro, J., Lenardelli, I., Wenk, H.-R., Dresen, G., Rybacki, E., Ren, Y., Tomé, C.N., Preferred orientation of anorthite deformed experimentally in Newtonian creep. *EPSL 264(1)*, 188-207, 2007.

Ji, S., Mainprice, D., Natural deformation fabrics of plagioclase: implications for slip systems and seismic anisotropy. *Tectonophysics 147*, 145–163, 1988.

Militzer, B., Wenk, H.-R., Stackhouse, S., Stixrude, L., First-principles calculation of the elastic moduli of sheet silicates and their application to shale anisotropy, *American Mineralogist, 96*, 125-137, 2011.

Ryzhova, T.V., Elastic properties of plagioclase, *Bull. Acad. Sci. USSR Geol. Ser. 7*, 633-635, 1964.

Seront, B., Mainprice, D., Christensen, N.I., A determination of the three-dimensional seismic properties of anorthosite: comparison between values calculated from the petrofabric and direct laboratory measurements, *J. Geophys. Res. 98*, 2209–2221, 1993.

Wenk, H.-R., Bunge, H.J., Jansen, E., Pannetier, J., Preferred orientation of plagioclase – neutron diffraction and U-stage data, *Tectonophysics 126*, 271-284, 1986.

Xie, Y., Wenk, H.-R., Matthies, S., Plagioclase preferred orientation by TOF neutron diffraction and SEM-EBSD, *Tectonophysics 370*, 269–286, 2003.

2 Laboratory Studies of Crystalline FeSi to 47 GPa and 2800 K

Zack Geballe and Raymond Jeanloz

Introduction

Equations of state, melting curves, mixing relations and solid-solid phase boundaries in iron and its alloys are the key equilibrium properties needed for modeling the constitution and evolution of planetary cores. Silicon is one element that is likely to be alloyed with iron in the cores of rocky planets; it is abundant in the rocks found on the surfaces of Mercury, Venus, Earth and Mars (*de Pater and Lissauer,* 2010), and in the laboratory it is known to alloy with liquid iron at high pressures (*Sanloup and Fei,* 2004) or at low oxygen fugacity (*McCoy et al.*, 1999).[1]

Recently, the cubic ε-phase of FeSi was found to transform to another cubic phase, B2, at 24 GPa and high temperature (*Dobson et al.,* 2002)—conditions that exist in the cores of Mars and Mercury. Yet several properties of the ε to B2 phase transition remain uncertain, including the location of the phase boundary in pressure-temperature space, and the entropy difference between the two phases.

Here we present X-ray diffraction data of hot, dense FeSi. First, we show that it remains solid up to at least 2350 ± 200 K at 23 GPa and 2770 ± 200 K at 47 GPa, which means that addition of silicon does not cause a large amount of melting point depression (the melting temperature of pure iron ranges from 2300 ± 100 K to 2700 ± 150 K between 20 and 50 GPa). Second, the ε to B2 crystal-crystal phase transition occurs at 30 ± 2 GPa at all temperatures from 1200 K to 2300 K. It results in a 5% density increase, which may cause an increase in the miscibility of silicon in iron at P > 30 GPa, with potential implications for the cores of small rocky planets such as Mars and Mercury.

Experimental Method

Stoichiometric FeSi was synthesized and given to us by Ravhi S. Kumar. It was ground to a fine powder and loaded into diamond anvil cells with rhenium gaskets. The samples were surrounded with an argon or neon pressure transmitting medium. High-pressure samples were laser-heated at GeoSoilEnviroCARS (GSECARS) end-station ID-D, and simultaneous emission spectra and X-ray diffraction images were collected (*Prakapenka et al.* 2008).

Details of temperature and pressure measurements and of their uncertainties will be presented in an upcoming publication.

Results and Discussion

The solid-solid phase transition from the low pressure ε phase to the high pressure B2 phase of FeSi occurs at 30 ± 2 GPa, the weighted average of the transition pressures detected in a neon pressure medium (31.2 ±1.7 GPa) and in an argon medium (28 ±1.9 GPa) (Figure 2.2.1). We detected no temperature dependence

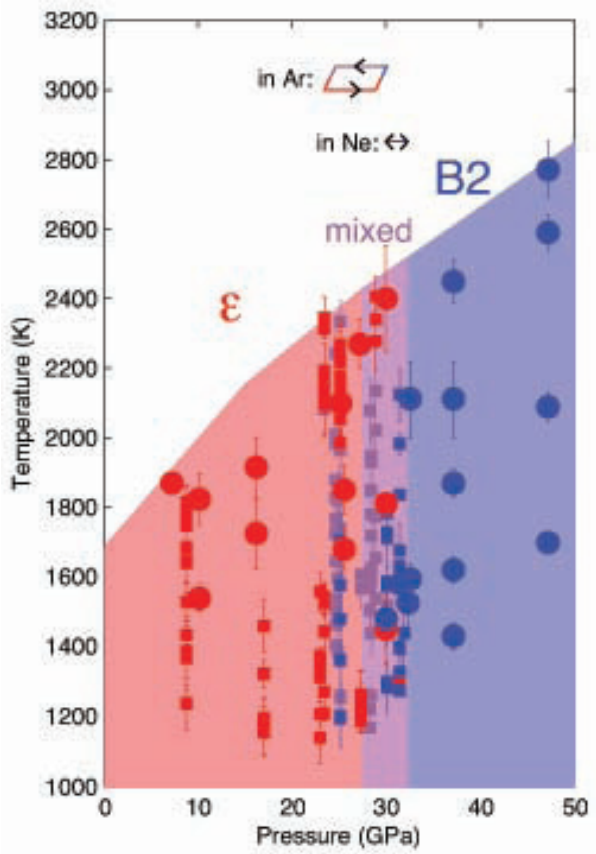

Figure 2.2.1: The ε-B2 phase transition of FeSi occurs at 30 ± 2 GPa, with no detectable temperature dependence between 1000 and 2400 K. Data using an argon pressure medium are represented by squares. Red symbols represent ε-FeSi, blue represents B2-FeSi, and purple indicates that a mixture of the two phases is seen in the diffraction data. Overlapping squares of various colors results from the hysteresis of the phase transition, revealed by reversing the transition multiple times. The phase boundary and hysteresis are summarized by the loop between 23 and 30 GPa, shown at the top of the figure. Data using a neon medium are represented by circles and summarized by the double-headed arrow from 30 to 32.3 GPa that indicates no observed hysteresis within our pressure intervals. Temperature uncertainties are indicated at each data point, whereas the typical pressure uncertainty is estimated to be 1.2 GPa.

of the ε-B2 transition in either pressure medium, despitecontrolling the temperature at 1200 ± 100 K for tens of seconds before increasing laser power: either the sample started transforming immediately upon heating to 1200 K, or it did not transform until pressure was increased. The ε-B2 transition was reversed multiple times in each pressure medium. Examples of the X-ray diffraction spectra that evidence the transition are shown in Figure 2.2.2. To constrain the hysteresis of the phase transition, we reversed the transition four times in a cell containing the neon pressure medium, and twice in a cell containing the argon medium. The reversals in neon showed no evidence of hysteresis once they were laser-heated, but rather bracket the

1. Much of this report is quoted from a manuscript submitted to American Mineralogist: paper #4612R

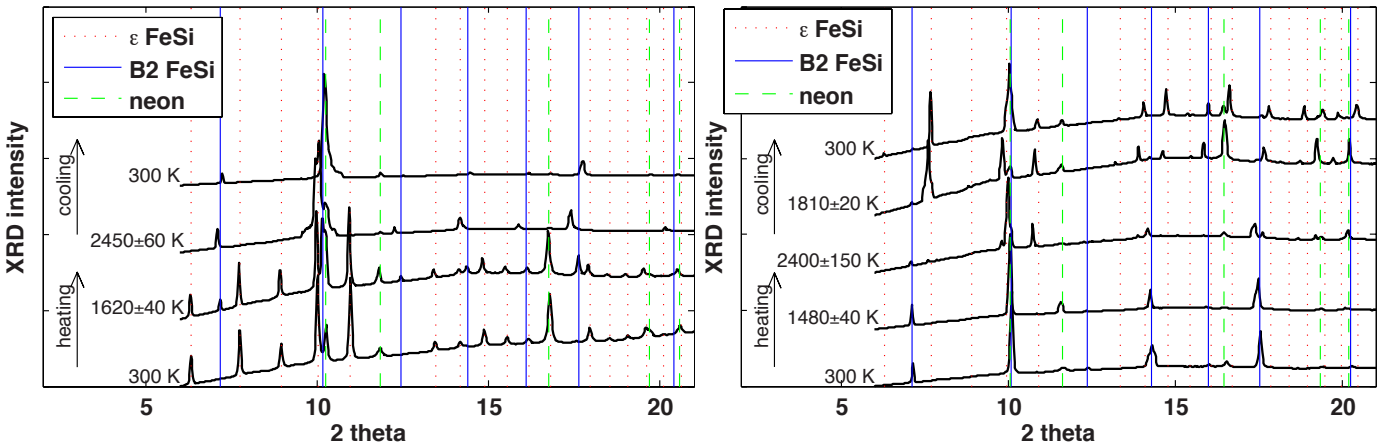

Figure 2.2.2: Diffraction pattern examples show a transition from the ε to the B2 phase of FeSi at 37 GPa (left) and the reverse transition, from B2 to ε at 30 GPa (right). Black curves show integrated powder diffraction data during the two heating/cooling cycles. Temperatures measured by spectroradiometry are shown to the left of diffraction patterns. Red dotted lines mark diffraction peak positions of FeSi lattice planes at 37 GPa or 30 GPa, while blue solid lines mark positions of B2-FeSi lattidce planes and green dashed lines mark positions of neon lattice planes. Deviations of high-temperature diffraction peaks from theoretical peak positions are mostly due to thermal expansion of sample and pressure medium..

transition to between 30 and 32.3 GPa. The reversals in argon, on the other hand, show hysteresis—upon laser-heating, the B2 phase is created at 32 GPa, transformed into the phase at 23 GPa on decompression, and transformed back into the B2 phase at 30 GPa upon re-compression.

X-ray diffraction patterns of samples at room temperature provide data to constrain the P-V equation of state of both phases of FeSi and show that density increases by 5% during the phase transition at 30 GPa, which may have implications for the cores of Mercury ($P_{core} \sim$ 10 to 40 GPa) and/or Mars ($P_{core} \sim$ 24 to 40 GPa) if silicon is an abundant alloying element. Qualitatively, the miscibility of silicon in crystalline iron may increase at ~30 GPa due to the increase in the effective hard sphere radius of silicon in the FeSi lattice as its coordination changes from 7-fold (ε-phase) to 8-fold (in the B2 structure), thereby improving the similarity of the radii of silicon and iron. Specifically, the immiscibility gap documented between iron-rich and iron-poor iron-silicon alloys at < 50 mol% Si may be reduced at pressures above 30 GPa.

Acknowledgements

We thank Ravhi Kumar for the sample material, Laura Robin Benedetti for help designing the study, and Sergey Tkachev and Vitali Prakapenka for help loading the samples. We acknowledge the support of GeoSoilEnviroCARS, which is supported by the NSF- Earth Sciences (EAR-1128799), and the DOE, Geosciences (DE-FG02-94ER14466). Use of the Advanced Photon Source, an Office of Science User Facility operated for the U.S. DOE Office of Science by Argonne National Laboratory, was supported by the U.S. DOE under Contract No. DE-AC02-06CH11357. Support for Z. M. Geballe was provided in part by an NSF Graduate Fellowship.

References

de Pater, I. and Lissauer, J. J., *Planetary Sciences*, 2nd ed. (Cambridge University Press, New York), 2010.

Dobson, D. P., Vocadlo, L. and I. G. Wood, A new high-pressure phase of FeSi: *American Mineralogist*, *v. 87*, p. 784–787, 2002.

McCoy, T. J., Dickinson, T. L., and Lofgren, G. E., Partial melting of the Indarch (EH4) meteorite: A textural, chemical, and phase relations view of melting and melt migration: *Meteoritics and Planetary Science*, *v. 746*, p. 735–746, 1999.

Prakapenka, V. B., Kubo, A., Kuznetsov, A., Laskin, A., Shkurikhin, O., Dera, P., Rivers, M. L., and Sutton, S. R., Advanced flat top laser heating system for high pressure research at GSECARS: application to the melting behavior of germanium. *High Pressure Research*, *v. 28*, p. 225–235, 2008.

Sanloup, C., and Fei, Y., Closure of the Fe-S-Si liquid miscibility gap at high pressure: *Physics of the Earth and Planetary Interiors*, *v. 147*, p. 57–65.58, 2004.

3 Shear Wave Velocity Model of the Eastern North America Upper Mantle Using Full Waveform Tomography

Huaiyu Yuan, Scott French, Paul Cupillard and Barbara Romanowicz

Summary

The EarthScope Transportable Array (TA) deployment has provided dense array coverage across the continental US and with it, the opportunity for high resolution 3D seismic velocity imaging of both the lithosphere and asthenosphere in the continent. Building upon our previous work, we present a new 3D isotropic and radially anisotropic shear wave model of the North American (NA) lithospheric mantle, using full waveform tomography and shorter-period (40 s) waveform data. Our model exhibits pronounced spatial correlation between major tectonic localities of the eastern NA continent, as evidenced in the geology, and seismic anomalies. This suggests recurring episodes of tectonic events are not only well exposed at the surface, but also leave persistent scars in the continental lithosphere mantle, marked by isotropic and radially anisotropic velocity anomalies that reach as deep as 100-150 km. In eastern North America, our tomographic images distinguish the fast velocity cratonic NA from the deep rooted large volume high velocity blocks which are east of the continent rift margin, and extend 200-300 km offshore into the Atlantic Ocean. In between is a prominent narrow band of low velocities that roughly follows the south and eastern Laurentia rift margin and extends into New England. The lithosphere associated with this low velocity band is thinned likely due to combined effects of repeated rifting processes along the rift margin and northward extension of the Bermuda low–velocity channel across the New England region. Deep rooted high velocity blocks east of the Laurentia margin are proposed to represent the Proterozoic Gondwanian terranes of pan-African affinity, which were captured during the Rodina formation but left behind during the opening of the Atlantic Ocean.

Full waveform inversion

We present a new high-resolution 3D tomographic model of shear velocity in the cratonic North American mantle (Figure 2.3.1), developed using long-period full waveform inversion. The new inversion shares many of the methodological features of our previous continental scale time-domain 3D waveform tomographic inversions for isotropic and radially anisotropic structure (*Yuan et al.*, 2011). We largely mirror the processing performed in the global SEM (spectral element method)-based hybrid modeling approach (*Lekic and Romanowicz*, 2011), except the global SEM synthetic code is replaced by RegSEM (*Cupillard et al.*, 2012).

Tomographic Results

The cratonic root has been affected by the recurring episodes of tectonism, however its eastern margin seems largely intact

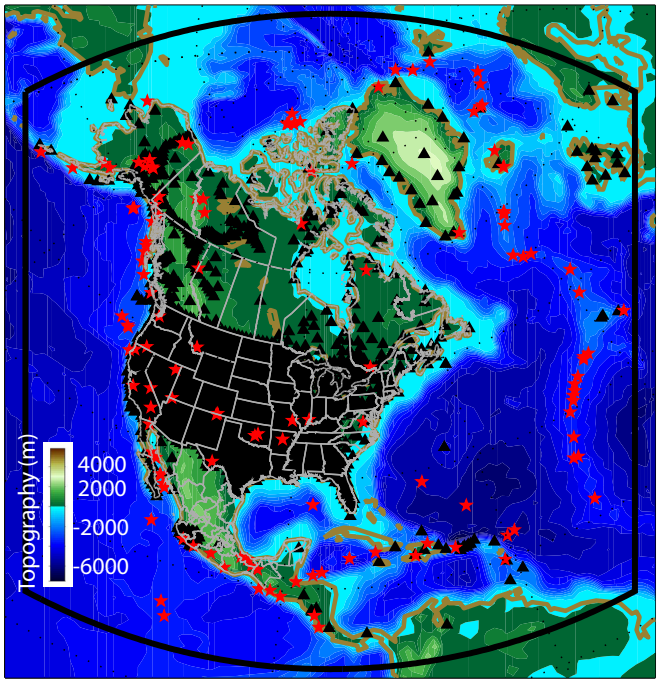

Figure 2.3.1: Source and station distribution for the new North American inversion. The black triangles show the seismic stations and the red stars show 136 local events in addition to our global and NA regional/teleseismic dataset. The thick black line indicates the model boundaries used for RegSEM forward modeling. The background shows the topography

west of the Grenville deformation front. The Archean lithosphere may have extended further outboard of the Proterozoic Grenville deformation front, as indicated by a high velocity Archean-like structure that extruded beyond the deformation front. Across the continental margin, thinning of the lithosphere is evident in our new tomographic images as well as discontinuity–sensitive receiver functions (*Rychert et al.*, 2007) and local Rayleigh wave dispersion inversion (*Li et al.*, 2003). A thinning process is likely further facilitated in New England by the passage of the Bermuda low velocity channel, which connects to the Bermuda hotspot in the Atlantic Ocean, and extends farther east in to the Atlantic Ocean.

Our new tomographic image reveals deeply rooted Gondawanian blocks that were captured during the North American/African collision that closed the Iapetus Ocean, but stayed behind when the present Atlantic Ocean was formed (*e.g.*, *Nance and Murphy*, 1994). These exotic terranes are clearly separated from the Laurentia core along the east continent margin, and extend greatly outboard into the Atlantic Ocean, reaching out to the oldest Atlantic oceanic crust. The presence of large segments of fossil continents off cratonic margins is thus not uncommon,

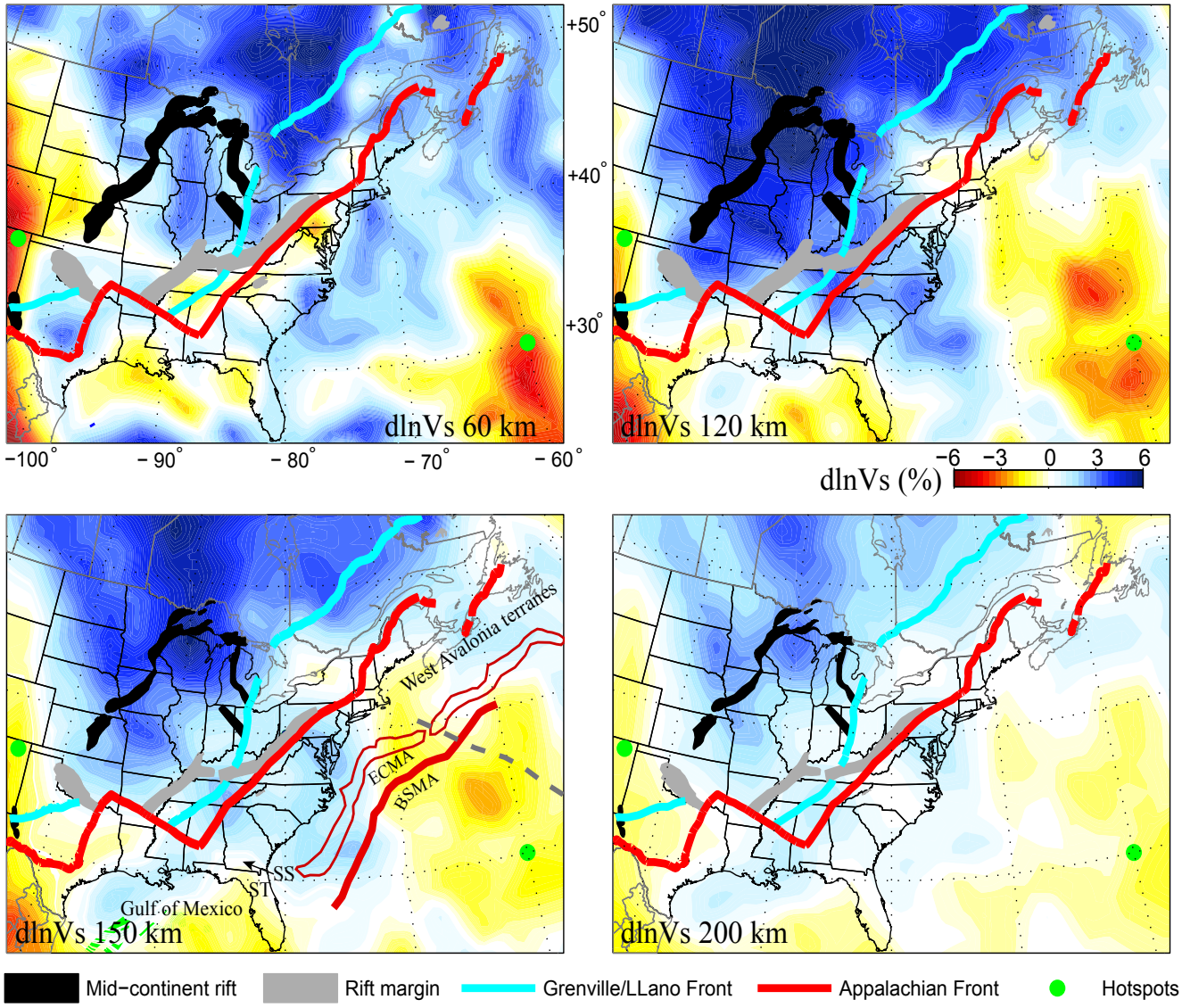

Figure 2.3.2: 3D isotropic Vs and radial anisotropy structure in eastern North America. The depth of each map is indicated. The Grenville/Llano deformation front is coded in cyan and continental rift margin in red. Green dots are hotspot locations; the Bermuda hotspot is near the lower right corner. The top four subpanels are for isotropic Vs; the bottom two are for radial anisotropy, ξ. Note the eastern edge of the high velocity craton closely follows the eastern continental rift margin (red line).

and may suggest greater roles in the global crustal-growth models (*e.g.*, *Griffin et al.*, 2011).

References

Griffin, W.L., Begg, G.C., Dunn, D., O'Reilly, S.Y., Natapov, L.M., Karlstrom, K., Archean lithospheric mantle beneath Arkansas: Continental growth by microcontinent accretion, *Geological Society of America Bulletin* 123, 1763-1775, 2011.

Li, A., Forsyth, D.W., Fischer, K.M., Shear velocity structure and azimuthal anisotropy beneath eastern North America from Rayleigh wave inversion, *J. Geophys. Res.* 108, 24 PP, 2003.

Nance, R.D., Murphy, J.B., Contrasting basement isotopic signatures and the palinspastic restoration of peripheral orogens: Example from the Neoproterozoic Avalonian-Cadomian belt, *Geology*, 22, 617-620, 1994.

Rychert, C.A., Rondenay, S., Fischer, K.M., P-to-S and S-to-P imaging of a sharp lithosphere-asthenosphere boundary beneath eastern North America, *J. Geophys. Res.* 112, B08314, 2007.

Yuan, H., Romanowicz, B., Fischer, K.M., Abt, D., 3-D shear wave radially and azimuthally anisotropic velocity model of the North American upper mantle, *Geophys. J. Int.* 184, 1237-1260, 2011.

4 Slab fragments in the western U.S.

Robert Porritt and Richard Allen

Introduction

The USArray deployment has provided new details of the seismic wave-speed structure of the western United States. The western U.S. is generally characterized as a low wave-speed region in global models (e.g. *Lekic and Romanowicz, 2011*) with relatively thin (~70km) lithosphere (e.g. *Levander and Miller, 2012*). This relatively unusual geologic context is ideally suited for asthenospheric mantle imaging with teleseismic travel times as the background 1D model is simple and only a small proportion of the travel time delays can be accounted for by the lithosphere. Within this low velocity region, there exist several isolated high velocity bodies, which have been interpreted as either lithospheric delaminations (e.g. *Zandt et al., 2004; West et al., 2009; Frassetto et al., 2011; Darold and Humphreys, 2013*), or slab fragments (e.g. *Obrebski et al., 2010; Schmandt and Humphreys, 2011; Pikser et al., 2012; Wang et al., 2013*). In this contribution we explore the argument between delaminations or slab fragments as seen by our compressional wave-speed model, DNA13-P.

Imaging

We employ the multi-channel cross correlation method (*VanDecar and Crosson, 1990*) to measure relative P wave arrival times for 76,322 station and event pairs within the 0.4-0.8 Hz band during the USArray deployment. The station coverage extends across the entire United States and events are chosen to be between 30 and 80 degrees epicentral distance from the station providing ample path coverage to fully image the western portion while avoiding waveform complications. The sensitivity matrix of the delays is populated using finite frequency kernels (*Dahlen et al., 2000; Hung et al., 2000*) and then solved for compressional wave-speed variations with a least squares iterative solver (*Dahlen et al., 2000; Hung et al., 2000*). We also solve for station corrections representing the vertically averaged lithosphere structure under a given station where crossing ray coverage is poor. The full model is available for download at the IRIS Earth Model Collaboration website (http://www.iris.edu/dms/products/emc/).

Discussion

Figure 2.4.1 provides a broad view of the wave-speed structure of the U.S. The eastward dipping plane illustrates three main features: (1) the high velocity anomalies in the western U.S. are short lateral wavelength features, (2) the high velocity body in the eastern U.S. is continuous, and (3) the Isabella Anomaly is the only shallow high velocity anomaly south of the Gorda plate. Based on paleoseismic evidence, the Juan de Fuca-Gorda system is well characterized as a subduction zone, but the limited depth extent of the high wave-speed body is inconsistent with ongoing subduction for the past 150+ Ma.

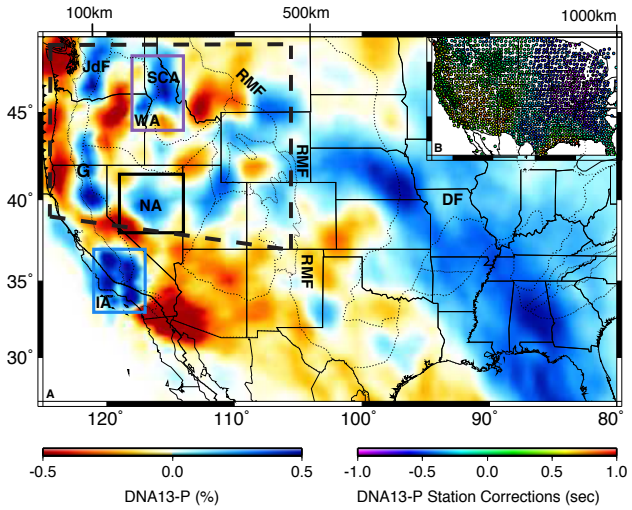

Figure 2.4.1: (A) An east-dipping plane through DNA13-P. Color scale gives relative compressional wave-speed (left color-bar). Purple, black, and blue boxes respectively outline the Siletzia Curtain Anomaly and Wallowa Anomaly, Nevada Anomaly, and Isabella Anomaly. The scale across the top edge of the map displays the depth of the tomography slice. Dotted lines mark the US physiographic boundaries (*Fenneman and Johnson*, 1946). Bold dashed outline displays the area considered in the calculation of expected western U.S. slab. (B) Inset map displays the station data used in the inversion and are color-coded according to station correction terms of DNA13-P (right color-bar). Abbreviations are given for the Juan de Fuca plate (JdF), Gorda plate (G), Isabella Anomaly (IA), Siletzia Curtain Anomaly (SCA), Wallowa Anomaly (WA), Nevada Anomaly (NA), Rocky Mountain Front (RMF), and Deep Farallon (DF).

However, the uplift of the modern Rocky Mountains and the distributed mantle high velocity anomalies suggest the slab was flat for a significant period of the subduction history. When we compare the expected amount of slab material from the coast to the Rocky Mountain Front (Figure 2.4.1, dashed box) against the observed amount of slab material, we find that ~80% of the expected material is observed as high velocity anomalies. If these anomalies are actually lower continental lithosphere in origin, it becomes unclear where the Farallon plate is currently.

Continental plate delamination has also been proposed due to observations of anomalous shear wave splitting (*West et al., 2009*), topography (*Saleeby and Foster, 2004*), and receiver function imaging (*Zandt et al., 2004*). However the regional anisotropy pattern identified in West et al. (*2009*) as due to vertical flow can also be readily reproduced by flow around the Gorda slab edge and the North American craton (*Yuan and Romanowicz, 2010*). Additionally, the topographic expression and receiver function images for the Isabella Anomaly are identical to those found in the Cascadia Subduction Zone (*Bostock et al., 2002*). Therefore, the primary pieces of evidence for delamination do not provide a unique fingerprint of the process.

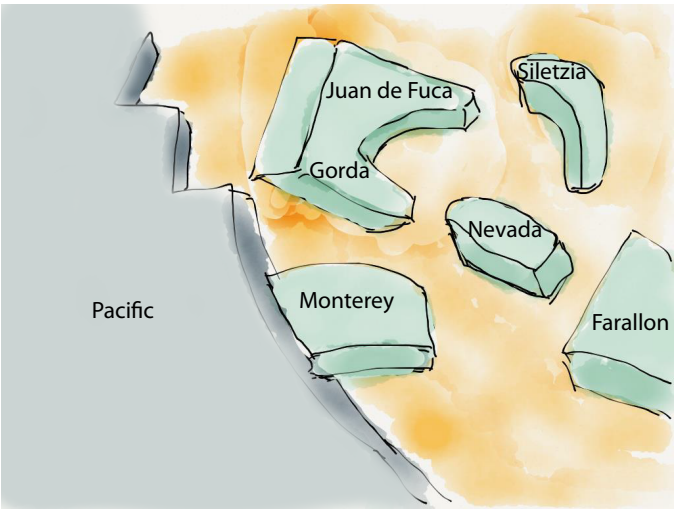

Figure 2.4.2: Schematic representation of high velocity anomalies of the western U.S. The Monterey Microplate labeled here is also referenced as the Isabella Anomaly. All of the labeled blue bodies are interpreted here to be ocean lithosphere.

Conclusion

Ambiguous evidence prevents determining if high wave-speed anomalies in the upper mantle are drips or remnant slabs when considered as individual geologic objects. When the western U.S. is considered as a whole, the theory that continental lithosphere drips are the source for all of these anomalies becomes unreasonable. Conversely, an oceanic lithosphere origin, such as the western Farallon slab, provides a viable source of high wave-speed material. Indeed, if the observed high-wave-speed anomalies are not interpreted as remnant slabs, we must identify where the Farallon slab went. Relatively young oceanic lithosphere has less rheological contrast to typical asthenosphere and is more readily able to founder in the upper mantle, rather than sink into the lower mantle (*Pikser et al., 2012*). With time, the eastward progression of the Farallon ridge toward North America provided younger and younger oceanic lithosphere into the subduction zone (*Atwater and Stock, 1998*). While the evidence does not show conclusively that these features must all be slabs, the slab hypothesis is consistent with the observations and follows naturally from the 150+ Ma subduction history. Therefore, analysis of high velocity anomalies in the western U.S., and elsewhere, must start with the hypothesis of an oceanic lithosphere origin before a delamination hypothesis should be invoked.

Acknowledgements

We would like to thank the UC-Berkeley regional imaging group (Cheng Cheng, Qingkai Kong, and William Hawley) for discussion of this work. We would also like to thank Jenny Taing for assistance in measuring arrival times. We thank IRIS and Earthscope for the USArray dataset. This work was funded by National Science Foundation grants EAR-0643077 and EAR-0745934.

References

Atwater, T., and Stock, J.M., Pacific-North America plate tectonics of the Neogene southwestern United States – an update, *Int. Geol. Rev., v. 40*, p. 375-402, 1998

Bostock, M.G., Hyndman, R.D., Rondenay, S.J., and Peacock S.M., An inverted continental Moho and the serpentinization of the forearc mantle, *Nature., v. 417*, p. 536-538, 2002

Dahlen, F. A., Hung, S.-H. and Nolet, G., Fréchet kernels for finite-frequency traveltimes—I. Theory,*Geophysical Journal International*, 141: 157–174. doi: 10.1046/j.1365-246X.2000.00070.x, 2000.

Darold, A., and Humphreys, E., Upper mantle seismic structure beneath the Pacific Northwest: A plume-triggered delamination origin for the Columbia River flood basalt eruptions: Earth Planet. *Sci. Lett*,, *v. 365*, p. 232-242, 2013.

Fenneman, N.M., and Johnson, D. W., Physiographic divisions of the conterminous U. S.: *USGS Water Resources,* 1946

Frassetto, A.M., Zandt, G., Gilbert, H., Owens, T.J., and Jones, C.H., Structure of the Sierra Nevada from receiver functions and implications for lithospheric foundering: *Geosphere*, *v. 7, no. 4*, p. 898-921, 2011.

Hung, S.-H., Dahlen, F.A. and Nolet, G., Fréchet kernels for finite-frequency traveltimes—II. Examples, *Geophysical Journal International*, *141*: 175–203. doi: 10.1046/j.1365-246X.2000.00072.x, 2000.

Lekic, V. and B. Romanowicz, Inferring upper-mantle structure by full waveform tomography with the spectral element method,*Geophys. J. Int. 185(2)*, 799-831, 2011.

Levander, A., and Miller, M.S., Evolutionary aspects of lithosphere discontinuity structure in the western U.S., *Geochem., Geophys., and Geosys., v. 13*, Q0AK07, doi:10.1029/2012GC004056, 2012.

Obrebski, M., Allen, R.M., Xue, M., and Hung, S-H., Slab-plume interaction beneath the Pacific Northwest: *Geophys. Res..Lett., v. 37*, L14305, doi:10.1029/2010GL043489, 2010.

Pikser, J.E., Forsyth, D.W., and Hirth, G., Along-strike translation of a fossil slab: *Earth Planet. Sci. Lett., v. 331–332*, p. 315-321, 2012.

Saleeby, J. and Foster, Z., Topographic response to mantle lithosphere removal in the southern Sierra Nevada region, *California. Geology, V. 32; no. 3*; p. 245-248; doi: 10.1130/G19958.1, 2004.

Schmandt, B., and Humphreys, E., Seismically imaged relict slab from the 55 Ma Siletzia accretion to northwest United States, *Geology, v. 39, no. 2*, p. 175–178, 2011.

Wang, Y., Forsyth, D.W., Rau, C.J., Carriero, N., Schmandt, B., Gaherty, J., and Savage, B., Fossil Slabs Attached to Unsubducted Fragments of the Farallon Plate, P*roc. Natl. Acad. Sci. U.S.A,. v. 110, no. 14*, p. 5342-5346, 2013.

West, J.D., Fouch, M.J., Roth, J.B., and Elkins-Tanton, L.T., Vertical mantle flow associated with a lithospheric drip beneath the Great Basin, *Nature Geosci., v. 2*, p. 439–444, 2009.

Yuan, H. and Romanowicz, B., Depth dependent azimuthal anisotropy in the western US upper mantle, *Earth Planet Sci. Lett., v. 300*, p. 385-394, 2010.

Zandt, G., Gilbert, H., Owens, T.J., Ducea, M., Saleeby, J., and Jones, C.H., Active foundering of a continental arc root beneath the southern Sierra Nevada in California, *Nature, v. 431*, p. 41–46, 2004.

5 Mantle Flow Geometry Through the Segmented Juan de Fuca Plate

Robert Martin-Short, Richard M Allen

Introduction

The Juan de Fuca slab is a remnant of the ancient Farallon plate, which has been subducting beneath the North American continent over the past 150 million years (*Eakin et al.*, 2010). Complete subduction of parts of this giant plate has split it into several sections. The northern unit is bounded to the south by the Mendocino Triple Junction (MTJ) and to the north by the Queen Charlotte Triple Junction off Vancouver Island (*Porritt*, 2013). This unit is divided into the Gorda, Juan de Fuca and Explorer slabs, which descend along the Cascadia subduction zone.

This subduction zone features some unusual characteristics, the most notable of which include a lack of earthquake activity below a depth of 100km (*Porritt*, 2013), a lack of slab material below 400km and the possibility of segmentation. Various models of slab-mantle interaction have been proposed to explain such observations, but more data is required to constrain these ideas.

This article presents the shear wave splitting measurements determined at 27 onshore seismometers situated along the subduction zone and 43 offshore instruments deployed across the Juan de Fuca plate. These measurements are used to infer the direction and extent of aethenospheric anisotropy and thus to determine mantle flow geometry in the region. This study assumes the existence of a type-A olivine crystal fabric, meaning that the anisotropy should be parallel to flow.

Method

This study analyzed waveform data from 27 onshore Transportable Array (TA) instruments and 57 ocean bottom seismometers deployed as part of the Cascadia Initiative between 2010 and 2012. Shear wave splitting observations were obtained for all of the TA instruments and 43 of the OBS devices.

Measurements of fast axis (φ) and delay time (δt) were carried out using the *Splitlab* software package (*Wustefeld et al.*, 2008). Teleseismic events of magnitudes greater than 5.75 and with epicentral distances of 85-130° were utilized, and each event was bandpass filtered between 0.02 and 0.3Hz.

The observations were rated 'good', 'fair' or 'poor' according to the criteria of *Wustefeld and Bokelmann* (2007). Average values of φ and δt for each instrument were then determined by stacking the error matrices resulting from a grid-search for the best parameter values from each observation followed by a determination of the global minimum.

In order to obtain useful results from the OBS data the orientations at which these devices settled on the seabed were calculated (*Frassetto et al.*, 2013). The splitting fast axis orientations were then determined relative to each station using the un-rotated seismograms and then rotated by the angle provided by *Frassetto et al.* (2013).

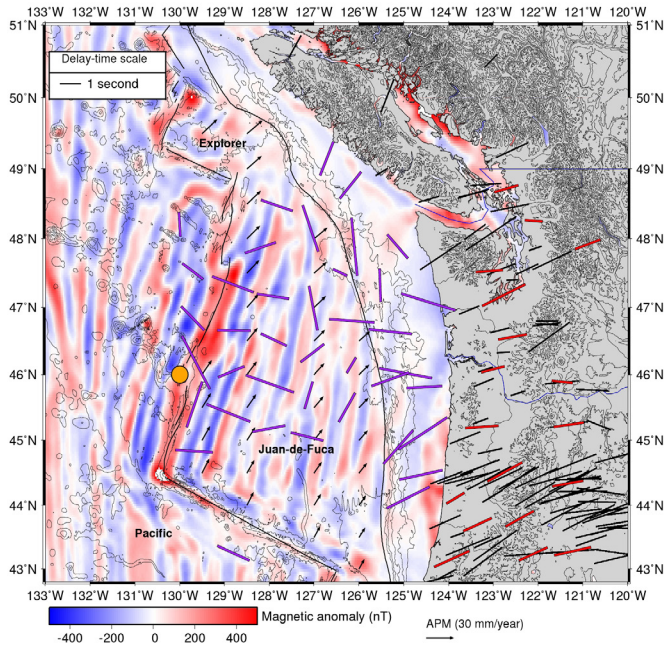

Figure 2.5.1. Map of the study region showing the oceanic crust magnetic anomoly pattern (*Maus et al.*, 2009) in additon to all available splitting results for the area. The onshore red splits are clearly trench-perpendicuar, while the offshore results are sub-perpendicular to the magnetic striping pattern within about 2° of the ridge axis, but then appear to be affected by the presence of the subduction zone. There is also some indication of a superposition of ridge perpendicular and radial splitting close to Cobb Hotspot, whose rough position is shown by the orange mark.

Results

Figure 2.5.1 shows the stacked results from this study plotted alongside measurments provided by previous investigations. The TA stations have a mean fast direction of N57.4°E and a mean splitting time of 1.39 seconds. The pattern produced by the offshore splitting measurements is more complicated. Splitting times are generally higher than for the TA stations, with a mean delay time of 1.81 seconds and a standard deviation of 0.52 seconds. Stations within 100km of the ridge generally produce fast axes that are perpendicular to this structure. The splitting patterns seen at offshore stations closer to the trench and acretionary prism are not uniformly trench perpendicular (as they are onshore). Instead, the splitting fast axes are rotated roughly trench parallel between 47°N and 49°N but rapidly switch back to trench-perpendicular below 47°N. The offshore spitting pattern west of Oregon is consistent with the onshore observations, while farther north in Washington the trench-perpendicular onshore splits are juxtaposed against the trench-parallel offshore splits. Onshore and offshore splits once again become consistent north of the Canadian border.

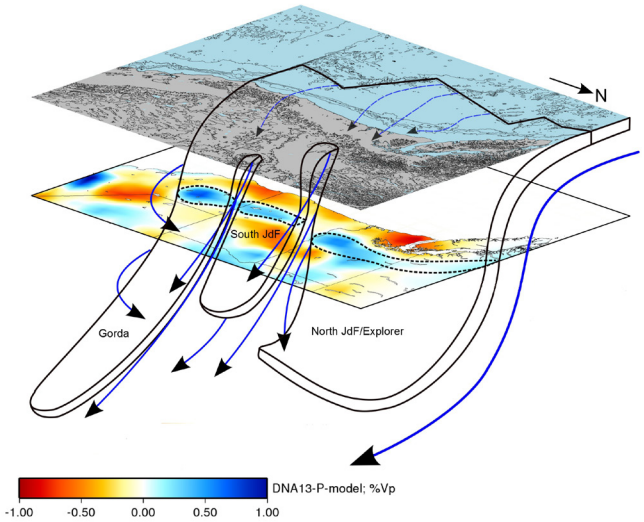

Figure 2.5.2: Cartoon summarising this study's interpretations in terms of mantle flow beneath and around the subducting Gorda, Juan de Fuca and Explorer plates. The tomography shows a depth slice though the DNA13-P wave model at 200km. The slab is segmented into at least three sections, with a third possible gap separating the Northern Juan de Fuca and Explorer sections. The tomography indicates that the slab beneath Oregon is particularly short, while the Gorda segment extends to at least 600km (*Porritt et al.*, 2013). Splitting results from this study indicate that eastwards flow west of the trench is initially ridge-parallel, but is then channelled though the Oregon slab gap. To the south, the cartoon shows toroidal flow around the edge of the Gorda slab as described by *Eakin et al.*, (2010). The slab poses an insufficient barrier to mantle flow to prevent eastwards motion beneath its base, as shown.

Discussion and interpretations

The lack of variation in the splitting parameters with event backazimuth and the uniformity of the onshore pattern suggests the presence of a single layer of anisotropy. The main source of the signal is interpreted to be the upper mantle, which is the only source thick enough to produce delay times of over 1 second. Figures 2.5.1 and 2.5.2 suggest that flow is ridge-perpendicular east of 128°W, as is consistent with the outwards movement of asthenospheric material.

The splitting pattern beyond 150km of the ridge is interpreted as being a result of asthenosphere flow responding to the presence of the subducting slab. With the exception of the trench-parallel results, splits west of the margin are seen to reduce in delay time towards the trench and rotate sub-parallel to the direction of plate motion. The reduction in delay times is interpreted as a result of the increasing misalignment of aethenospheric and lithospheric anisotropy, as predicted by *Nishimura and Forsyth* (1989).

The offshore measurements provide an indication of funnelled aethenospheric flow into the gap within the elongate high velocity anomaly shown in Figure 2.5.2. This anomaly is interpreted to be the result of the subducting slab (*Porritt*, 2013), implying that the relatively lower velocities beneath northern Oregon indicate a 'slab gap'. This may be a tear in the subducting lithosphere which allows for unimpeded eastwards flow of material.

The general pattern of trench perpendicular splitting seen in this study lends further support to the well established interpretation of a thick layer of mantle material entrained beneath the subducting slab. The slab appears provide an insufficient barrier to mantle flow to cause the trench parallel splitting pattern seen at other subduction zones (*Eakin et al.*, 2010).

Acknowledgements

This study benefited from discussions with Brent Evers, Caroline Eakin, Robert Porritt and Cheng Cheng. The figures were created using the Generic Mapping Tools.

References

Eakin, CM, Obrebski, M, Allen, RM, Boyarko, DC, Brudzinski, MR and Porritt, R, 'Seismic anisotropy beneath Cascadia and the Mendocino triple junction: Interaction of the subducting slab with mantle flow', *Earth and Planetary Science Letters*, vol 297, pp. 627-632, 2010.

Frassetto, A, Adinolfi, A and Woodward, B, 'Cascadia Amphibious Ocean Bottom Seismograph Horizontal Component Orientations', Seismic experiment report, OBSIP Management Office, Incorporated Research Institutions for Seismology (IRIS), 2013.

Maus, S, Barckhausen, U, Berkenbosch, H, Bournas, N, Brozena, J, Childers, V, Dostaler, F, Fairhead, J, Finn, C, von Frese, R and others, 'EMAG2: A 2--arc min resolution Earth Magnetic Anomaly Grid compiled from satellite, airborne, and marine magnetic measurements', *Geochemistry, Geophysics, Geosystems*, vol 10, 2009.

Nishimura, CE and Forsyth, DW, 'The anisotropic structure of the upper mantle in the Pacific', *Geophysical Journal International*, vol 96, pp. 203-229, 1989.

Porritt, RW, 'Tracing the Farallon plate though seismic imaging with USArray', PhD Thesis, University of California Berkeley, 2013.

Wustefeld, A, Bokelmann, G, Zaroli, C and Barruol, G, 'SplitLab: A shear-wave splitting environment in Matlab', *Computers & Geosciences*, vol 34, pp. 515-528, 2008.

Wustefeld, A and Bokelmann, G, 'Null detection in shear-wave splitting measurements', *Bulletin of the Seismological Society of America*, vol 97, pp. 1204-1211, 2007.

6 Seismic Constraints on a Double-Layered Asymmetric Whole-Mantle Plume Beneath Hawaii

Cheng Cheng, Richard M Allen, Rob W Porritt and Maxim Ballmer

Introduction

The Hawaii hotspot and the associated chain of islands have been long regarded as a case example of a deep-rooted mantle plume and a region thought to be an ideal place for studying intraplate hotspots located above a deep-rooted mantle plume. There is an ongoing debate, however, about the origin of the hotspot volcanism reservoir, in particular when examining the depth and direction from which any plume originates. Geochemistry observations of the region indicate the Hawaiian Plume contains 15-20% mafic lithologies such as eclogites, and they also show there is a conspicuous asymmetry in the mafic composition of different parts of the island. Based on volcano lava measurements, the island is divided into two parts: LOA and KEA, and there is more pyroxenite in the source of the LOA-volcanoes. In this work we address the question: is Pacific Plate rejuvenation occurring under the islands, and if it is, how wide and how deep is the region where the plume modifies the lithosphere? To answer these questions, we need to use geophysical, geochemical and seismological information.

Data and Method

The Hawaiian Plume-Lithosphere Undersea Melt Experiment (PLUME) included a large network of four-component broadband ocean bottom seismometers (OBSs) occupying more than 70 sites and having an overall aperture of more than 1000 kilometers. We selected ~750 S-wave relative arrival times (including direct S and SKS phases) on the SV component via multi-channel cross correlation. Of these, we selected 75 events distributed in as wide a range of back azimuth directions as possible (Figure 2.6.1), restricting the data to events with epicentral distances greater than 30 degrees and magnitudes greater than 5.5. The relative delays we obtain are inverted with a tomographic technique that uses finite-frequency sensitivity kernels that account for the frequency dependent width of the region to which body waves are sensitive and also accounts for wave front healing effects. Our tomographic method uses paraxial kernel theory to calculate the Born approximation forward-scattering sensitivity kernels for teleseismic arrival times. The surface-wave data we use here comes from two different sources. The first is ambient noise cross-correlation measurements in the period band of 10 to 25 sec. The second source is surface wave phase velocity measurements obtained using a two-plane wave tomography method in the period band of 25 to 100 sec. Following *Obrebski et al.* (2011) we create a joint matrix of body wave relative travel time anomalies and surface wave phase velocity anomalies to use in a joint inversion.

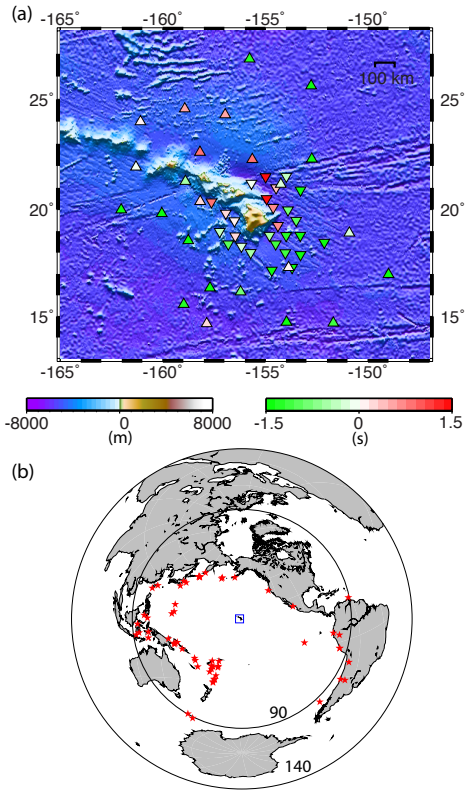

Figure 2.6.1. Map of the study area. (a) Study area showing seismometer locations (triangles) where stations deployed in the first year are indicated by inverted triangles and those deployed in the second year are marked by triangles. The station colors indicate the mean body-wave delays (measured at 0.04–0.1 Hz). Only stations that successfully recorded data are shown. These locations are juxtaposed on the topography and bathemetry of the region. (b) Map of earthquakes (red stars) used in this study and our study location (blue box). Black circles are 90° and 140° from the study region.

Imaging Results

We create two models, named as follows: HW13-SV based on inversion of SV body wave constraints only, and HW13-SVJ resulting from joint inversion of the body- and surface-waves. Figure 2.6.2 shows vertical cross-sections through the main features of the models, comparing HW13-SV and HW13-SVJ structures. The improvement our new model provides is a higher resolution within the upper mantle that results from our inclusion of surface wave data in the inversion. In addition to the shallow low-velocity layer observed immediately below the oceanic lithosphere, we also observe a second layer at the depth of about ~250-400 km (see cross-section in Figure 2.6.2b)

In the vertical cross-section perpendicular to the plate motion, the model shows an apparent asymmetry in the low velocity structure of this second layer. Larger volumes of low velocity

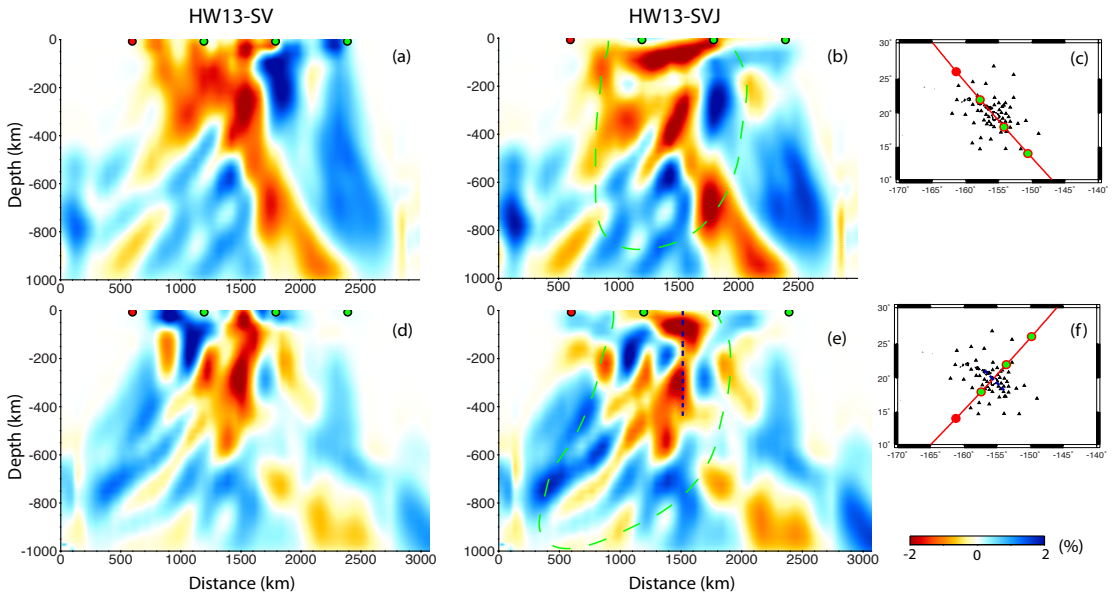

Figure 2.6.2: Vertical cross-sections through the HW13 models. Images (a-b) are cross-sections parallel to the Pacific plate motion, whereas images (d-e) are cross-sections perpendicular to the plate motion. (c, f) maps indicate the locations of the cross-sections and the distribution of stations. Results (a) and (d) are from the body-wave-only inversion (HW13-SV), (b) and (e) are from the joint ambient noise, surface wave and body wave inversion (HW13-SVJ). The dashed green contours on (b) and (e) encompass areas with good ray coverage. The dash blue line on (e) and (f) indicates the separation of the Loa (left) and Kea(right) volcano trends.

material are observed on the northwest side of the island chain (Figure 2.6.2e). Finally, good resolution is obtained through the crust and lithosphere by the joint ambient noise and earthquake surface wave data. We conduct checkerboard resolution tests using boxes with alternating high and low-velocity and of different sizes to identify what resolution our models can provide. The inclusion of the surface-wave dataset provides improved resolution in the upper ~200 km. The tests results show that the horizontal resolution is about 150 km in the upper 100 km, about 300km in the upper mantle and transition zone, and 500km in the lower mantle. The resulting structure also correlates well with previous surface-wave only tomographic models (*Laske et al.*, 2011).

Discussion

Though seismic imaging in the past has been considered inconclusive with regard to whether a lower-mantle plume source exists, our imaging results are similar to *Wolfe et al.* (2009)'s result in the lower mantle. Both results reveal low velocities within the mantle transition zone and in the topmost lower mantle, suggesting there is a deep source region for the Hawaiian plume.

Differing from the classic plume model, which has a vertical conduit feeding a thin pancake structure beneath the lithosphere, our model shows two layers of low velocity in the upper mantle. One layer is at <150 km depth, and the second is in the ~200 to 400 km depth range, thus forming a non-traditional double layered plume. Our model structure is consistent with a geodynamic model in which a plume composed of peridotite (85%) and chemically dense eclogite (15%) generates a neutrally buoyant layer at a depth of 260 to 410 km from which a fractionated upwelling rises further to feed a shallow pancake (*Ballmer et al.*, 2013). When peridotitic material from the lower mantle crosses the 410-km discontinuity, its density decreases. However, the density of eclogite does not. The combination of the negative chemical buoyancy when eclogite is present with the positive thermal buoyancy will control the ascent motion of a plume rich in eclogite. This dense material tends to accumulate at the 410km depth, forming a deep eclogitic pool (DEP), which would produce a velocity structure consistent with the second low velocity layer in our tomographic model. Another important feature of our model is the asymmetric low velocity zone that trends perpendicular to the plate motion direction in the DEP depth range (Figure 2.6.2e). The low velocity structure beneath the southwest side of the island chain (left side of the dashed blue line in Figure 2.6.2e) is larger and wider than the structure on the northeast side (right side of the dashed blue line in Figure 2.6.2e). The lateral velocity variations observed, if indicative of lateral temperature variations, may reconcile geochemical evidence in Hawaii that imply a larger influence from pyroxenite-derived lavas along the southwest Loa trend compared to the northeast Kea trend.

References

Obrebski, M., R.M. Allen, F. Pollitz, and S.-H. Hung, Lithosphere-asthenosphere interaction beneath the western United States from the joint inversion of body-wave traveltimes and surface-wave phase velocities, *Geophys. J. Int.* 185, 1003-1021, doi:10.1111/j.1365-246X.2011.04990.x, 2011.

Ballmer, M., Ito, G., Wolfe, C., Solomon, S., Double-layering of a thermochemical Hawaiian plume in the upper mantle. Submitted.

7 New Oceanic Mantle Structures Revealed by Global Full-Waveform Inversion

Scott French, Vedran Lekic, Barbara Romanowicz

Introduction

The SEMum2 model (*French et al.*, in review) was derived using full long-period (60-400s) waveform inversion based on the spectral element method (SEM: e.g. *Komatitsch and Vilotte*, 1998). Much like its predecessor SEMum (*Lekic and Romanowicz*, 2011a), SEMum2 exhibits stronger lateral heterogeneity – particularly low velocities in the upper 250km – than previous generations of global models based purely on asymptotic theories (*Lekic and Romanowicz*, 2011b), while still confirming the robust long-wavelength structure present in the latter models. In addition to recovering more realistic amplitudes of heterogeneity, the oceanic upper mantle and transition zone in SEMum2 show a more continuous fast signature of subducted slabs with depth, as well as coherent conduit-like low-velocity anomalies extending to the lower mantle, most prominent beneath the South Pacific superswell and Hawaii. Further, SEMum2 exhibits a pattern of low-velocity anomalies in the oceanic upper mantle not clearly imaged in previous generations of global models: finger-like low-velocity bands aligned with absolute plate motion (*Kreemer*, 2009) between 200 and 350km depth. Here, we first briefly introduce SEMum2, focusing on model construction, and devote the remaining sections to discussion of these low-velocity finger (LVF) structures.

SEMum2: Model construction

SEMum2 represents an update to the SEMum model of Lekic and Romanowicz (2011a), incorporating a new crustal implementation and a change in parameterization that allows for higher resolution images of mantle structure. Both models employ a "hybrid" waveform inversion technique, where wavefield forward modeling is performed "exactly" using the SEM and combined with sensitivity kernels from non-linear asymptotic coupling theory (*Li and Romanowicz*, 1995). Though approximate, NACT kernels are computationally light and easily recalculated as the mantle model evolves, and further accommodate finite-frequency effects in the great-circle plane as well as multiple forward scattering. Each iteration of the hybrid approach represents a 3x reduction in cost over adjoint techniques (e.g. *Tromp et al.*, 2005), while also allowing for a quickly converging Newton-like inversion scheme, reducing the total number of iterations required.

To further reduce cost, we use a smooth crustal model with a minimum Moho depth of 30km, otherwise approximately honoring Crust2.0 Moho topography (*Bassin et al.*, 2000). The model is calibrated to match the seismic response of Earth's crust, as seen through surface-wave dispersion, by introducing radial anisotropy – necessary to match the response of a realistically-layered model at long periods (*Backus*, 1962). By prolonging the SEM time step, the smooth crust reduces the cost of simulation an additional 3x over direct use of Crust2.0. While SEMum also employed a smooth crustal model, its uniform 60km thickness could potentially complicate interpretation of oceanic upper-most mantle structure – thus motivating the now shallower, variable Moho topography. Details of the calibration procedure have also been improved (*French et al.*, in review).

Following the introduction of the new crustal model, we performed two additional inversion iterations starting from SEMum. Next, we refined the V_S mantle-model mesh from 4° to 2° node spacing and performed one further iteration. This change in parameterization allowed for a relaxation of a priori smoothness constraints on model structure, which was further justified by resolution analysis (*French et al.*, in review). While SEMum2 model structure appears sharper than SEMum at all depths and has evolved somewhat above 60km, the two models remain strikingly similar, validating a posteriori the approach taken in developing SEMum.

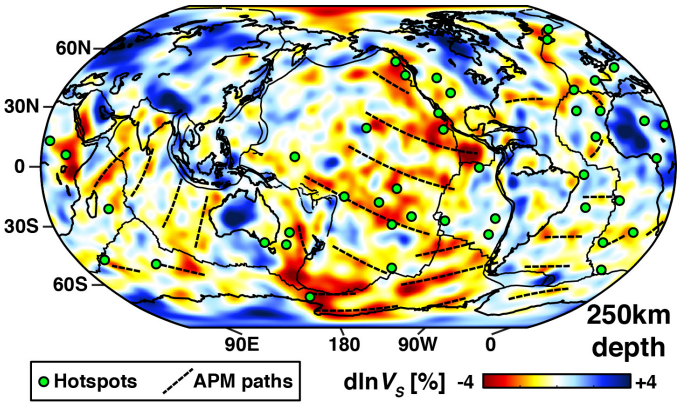

Figure 2.7.1: V_S anomaly structure at 250km depth in SEMum2, where low-velocity finger structures are immediately apparent. Dashed lines correspond to APM streamlines of Kreemer (2009).

Oceanic low-velocity structure

Clustering analysis (e.g. *Lekic and Romanowicz*, 2011b) of SEMum2 oceanic upper-mantle structure between 30 and 350km depth reveals a class of features characterized by lower-than-average V_S in the 200-350km depth range and a band like morphology in map view. These features are easily seen in SEMum2 at 250km depth (Figure 2.7.1) as elongate finger-like anomalies of significantly reduced V_S (3-4%), separated by regions of slightly elevated V_S. These features are most prominent in the central and eastern Pacific but are also present beneath other oceans (Indian, Western Antarctic, and North and South Atlantic, etc…). Intriguingly, as shown in Figure 2.7.1, these low-velocity fingers (LVFs) in the oceanic upper mantle preferentially align with the direction of present-day absolute plate motion (*Kreemer*, 2009).

In the Pacific, these APM-parallel LVFs exhibit an approx-

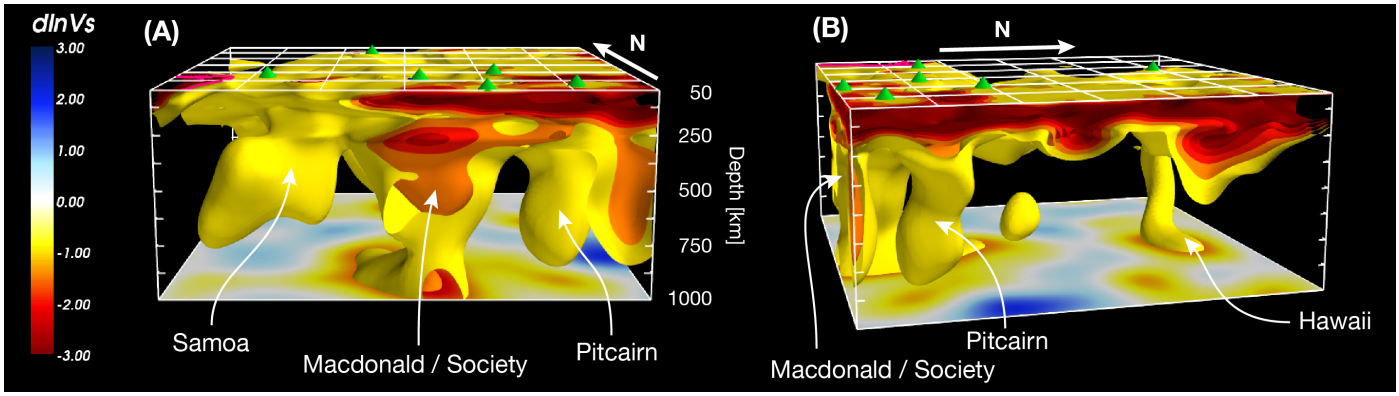

Figure 2.7.2: A 3D rendering of a 60°x60° portion of the central Pacific to 1000km depth. Min/max isocontour levels: -3 to -1%. Panel: (A) View from the South; (B) View from the East-South-East. Approximate correspondence between conduit-like anomalies and overlying hotspots (green cones; *Steinberger*, 2000) also noted.

imate 2000km periodicity, and their presence correlates with enhanced low velocity anomalies in the overlying classical oceanic low-velocity zone (LVZ). Intriguingly, in an analysis of the geoid using directional wavelets, Hayn et al. (2012) discovered a large-scale pattern of undulations matching both the ~2000km wavelength and APM alignment of the LVFs in the central and eastern Pacific – thereby providing independent geophysical evidence confirming their presence. In order to frame the LVFs in the context of surrounding mantle structure, in Figure 2.7.2 we present a 3D rendering of a 60°x60° portion of the central Pacific to 1000km depth. We see in SEMum2 a progressive transition from structure dominated by the classical oceanic LVZ at shallow depths (<200km), to that dominated by the LVFs (200-350km), to quasi-vertical conduit-like low-velocity anomalies (>300-400km) extending to the lower mantle that are spatially correlated with known hotspots or hotspot regions.

Morphology of the LVFs and their apparent interactions with the conduit-like anomalies below suggest channeling of buoyant upwellings into the asthenosphere – perhaps similar to laboratory experiments in viscous fingering (*Snyder and Tait*, 1998). Alternatively, their periodicity may be consistent with APM-aligned secondary convection similar to that suggested by Richter and Parsons (1975). Taken together, the observed interactions between the LVFs, the LVZ above, and the quasi-vertical conduit-like anomalies below evoke an interplay between a range of geodynamic phenomena that is both pervasive in the oceanic mantle and has not before been imaged at these scales.

Acknowledgements

This work was supported by the National Science Foundation (EAR-0738284). SF acknowledges support from the NSF Graduate Research Fellowship Program. SEM computations were performed at the National Energy Research Scientific Computing Center (supported by the DOE Office of Science, Contract No. DE-AC02-05CH11231).

References

Backus, G. E., Long-wave elastic anisotropy produced by horizontal layering, *J. geophys. Res.*, 67, 4427-4440, 1962.

Bassin, C. G. L., Laske, G., and Masters, G., The current limits of resolution for surface-wave tomography in North America, *EOS, Trans. Am. geophys. Un.*, 81, 2000.

Hayn, M., Panet, I., Diament, M., Holschneider, M., Mandea, M., and Davaille, A., Wavelet-based directional analysis of the gravity field: evidence for large-scale undulations, *Geophys. J. Int.*, 189, 1430-1456, 2012.

Komatitsch, D. and Vilotte, J.-P., The spectral element method: An efficient tool to simulate the seismic response of 2D and 3D geological structures, *Bull. Seism. Soc. Am.*, 88, 368-392, 1998.

Kreemer, C., Absolute plate motions constrained by shear wave splitting orientations with implication for hot spot motions and mantle flow, *J. geophys. Res.*, 116, B10405, 2009.

Lekic, V. and Romanowicz, B., Inferring upper-mantle structure by full waveform tomography with the spectral element method, *Geophys. J. Int.*, 185, 799-831, 2011a.

Lekic, V. and Romanowicz, B., Tectonic regionalization without a priori information: A cluster analysis of upper mantle tomography, *Earth Planet. Sci. Lett.*, 308, 151-160, 2011b.

Li, X. D. and Romanowicz, B., Comparison of global waveform inversions with and without considering cross-branch mode coupling, *Geophys. J. Int.*, 121, 695-709, 1995.

Richter, F. M. and Parsons, B., On the Interaction of Two Scales of Convection in the Mantle, *J. geophys. Res.*, 80, 2529-2541, 1975.

Snyder, D. and Tait, S., A flow-front instability in viscous gravity currents, *J. Fluid Mech.* 369, 1-21, 1998.

Steinberger, B., Plumes in a convecting mantle: Models and observations for individual hotspots, *J. geophys. Res.*, 105, 11,127-11,152, 2000.

Tromp, J., Tape, C., and Liu, Q., Seismic tomography, adjoint methods, time reversal, and banana-doughnut kernels, *Geophys. J. Int.*, 160, 195-216, 2005.

8 Variable Seismic Anisotropy Across the African LLSVP Southern Margin

Sanne Cottaar, Barbara Romanowicz

Introduction

Seismic anisotropy, *i.e.* the variation of seismic wave speed with propagation direction, provides information on material flow and therefore the dynamics in the earth's interior. Seismic anisotropy appears to be strong in the upper mantle and in the lowermost mantle (the D"), where strains related to horizontal flow in the large scale mantle convection system tend to be large.

Here we show evidence for strong seismic anisotropy in the D" using waveforms of shear waves diffracted along the core-mantle boundary. The seismic anisotropy appears strong to the south of the African Large Low Shear Velocity Province (LLSVP). The anisotropy rotates or weakens towards the LLSVP boundary, and there is no apparent anisotropy inside the LLSVP.

Data and Methods

In this study, we use shear diffracted phases from a deep event near the Fiji islands (~621 km, M_w 6.2, 09/04/1997, Figure 2.8.1) towards stations in southern Africa at distances of > 120°. Diffracted phases at these distances become polarized along the SH component due to the coupling of the SV component with the outer core. *To et al.* (2005) first pointed out the anomalously strong SV arrivals, which result in elliptical particle motions (Figure 2.8.2). These arrivals result from the splitting of the SH component due to the presence of anisotropy.

We measure the shear-wave splitting with the rotation-correlation method in SplitLab (*Wuestefeld et al.* 2010). The stations at smaller azimuths show a mean fast axis of -46° (defined to be positive away from the T component towards the R component) and a mean splitting time of 1.0 second.

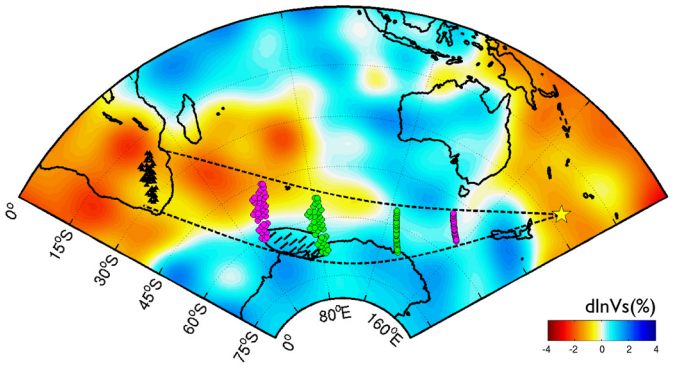

Figure 2.8.1: Coverage map of Sdiff phases from a deep Fijian earthquake (Sept. 4th 1997) observed on the Kaapvaal array in southern Africa. Magenta dots mark the entry and exit points to D" and the green dots bound the diffracted parts of the paths. We interpret the apparent anisotropy to be where the phases turn upwards in the D" indicated by the striped patch. The background model is SAW24B16 (*Megnin and Romanowicz*, 2000) at 2800 km depth.

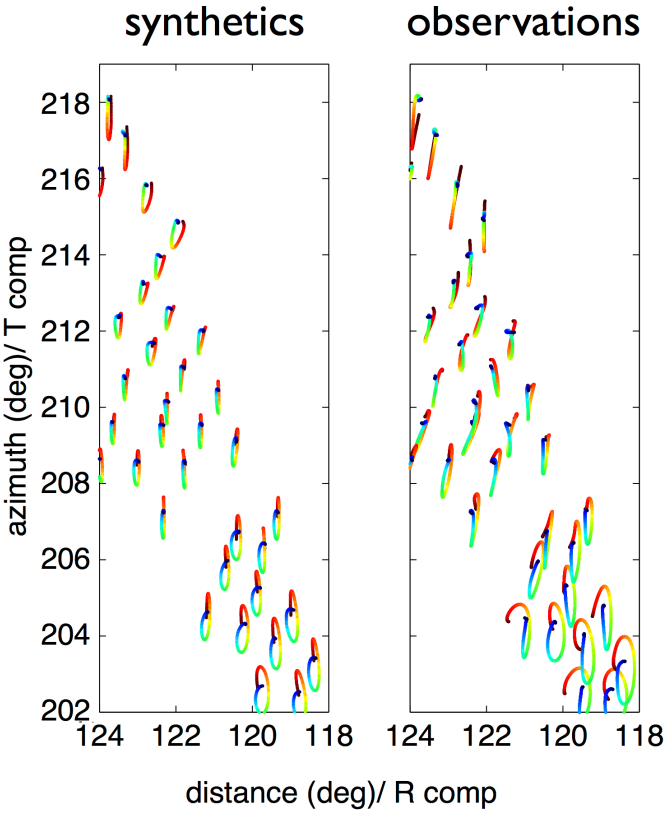

Figure 2.8.2: Particle motions for the horizontal velocity components. Waveforms are filtered between 10 and 30 seconds. Time runs from blue to red over 30 seconds. On the right are the observed particle motions at stations of the Kaapvaal array. Most striking are the elliptical particle motions at smaller azimuths. On the left are synthetic particle motions that capture most of the main features of the data (see Results subsection).

The splitting in Sdiff results from the presence of anisotropy in the upward leg of the path after the diffracted part of the path. We separately measure the splitting in the SKS and SKKS phases to exclude an origin of the splitting in the upper mantle. There is little and very scattered splitting in these phases for this event. Other studies of upper mantle anisotropy beneath the Kaapvaal array (*e.g., Adam and Lebedev*, 2012) show different trends than the shear-diffracted waveforms would suggest here.

We forward model full waveforms for anisotropic models in the D" using the 'sandwiched' Coupled Spectral Element Method ('sandwiched'-CSEM, *Capdeville et al.* 2003). This method couples the spectral element solution for an anisotropic 3D velocity model in the lowermost 370 km of the mantle to a 1D normal mode solution in the rest of the mantle and the outer core. It is computationally advantageous to apply this method for different models in the lowermost mantle for a single event, as the normal mode computation only needs to be done once. The background model is SAW24B16 (*Megnin and Romanowicz*, 2000) saturated at +1% outside and -2.75% inside the LLSVP.

The saturated model captures the delay in travel time with increasing azimuth (which is apparent in the change in color in particle motions in the second panel of Figure 2.8.2). We define the anisotropy to be in the plane orthogonal to the direction of propagation, as this relates to the apparent anisotropy seen in the waveforms, but we acknowledge that this only represents part of the actual anisotropic elastic tensor. With full waveform modeling we test the sensitivity to fast direction, strength of anisotropy and radial and lateral extent of the anisotropy (*Cottaar and Romanowicz*, 2013). Here we only present the best model.

Results

The preferred model has a fast axis direction as measured in the data, and 8% of velocity contrast between the fast and slow axis. The anisotropy is constrained to the lowermost 150 km, although there is a strong trade-off between the vertical extent and the strength of anisotropy. Laterally, the anisotropy is constrained to the fast region (with isotropic velocity perturbations over 0.5%). The synthetic waveforms for this model are shown in Figure 2.8.2.

The synthetic waveforms capture the ellipticity of the particle motions at smaller azimuths. They do not capture the increase in amplitude at these azimuths. The amplitudes of the waveforms are higher than predictions for PREM. The synthetics show a decrease in amplitude and a postcursor due to multi-pathing around the LLSVP boundary. The postcursor in the synthetics is less delayed than in the observations (*To et al.,* 2005), resulting in elliptical particle motions. The amplitudes within the LLSVP, at the higher azimuths, are larger due to the slow velocities. The SHdiff arrivals are rotated slightly out-of-plane due to refractions at the LLSVP boundary. The rotations are opposite for the synthetics and observations, though. Capturing the exact multi-pathing and refraction behavior requires corrections to the boundary shape, which is beyond the scope of this study.

Conclusion

We found evidence for the presence of strong anisotropy to the south of the African LLSVP margin by using shear diffracted phases at large distances. We can constrain the part of the elastic tensor that causes the splitting in the waveforms, *i.e.* in the plane orthogonal to the direction of propagation. Most strikingly, the anisotropy weakens towards the LLSVP boundary, and appears absent within.

This study adds an additional location where the presence of strong complex anisotropy appears to correlate with fast velocities and possibly with the presence of slab remnants. Additionally, the presence of textured postperovskite could explain strong anisotropy, as its single crystals have stronger azimuthal anisotropy than in perovskite. The LLSVP margin might be acting as a mechanical boundary that rotates the present fabric (Figure 2.8.3). Within the LLSVP, convection is either too weak or small-scaled, or the material's intrinsic anisotropy is too weak to observe using diffracted waves.

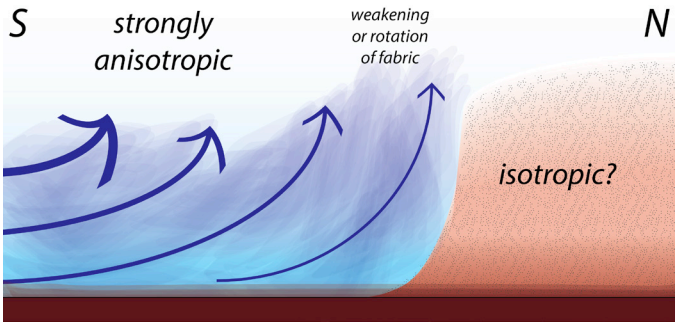

Figure 2.8.3: Cartoon cross-section from south to north through the edge of the African LLSVP with possible flow outside the LLSVP as suggested by the observed anisotropy.

Acknowledgements

The data for this project came from IRIS (www.iris.edu). We thank Yann Capdeville for providing the CSEM code which produced the synthetic data in this study. Shear wave measurements are done with help of the SplitLab Matlab package (www.gm.univ-montp2.fr/splitting/). This work was supported by NSF/CSEDI grant 1067513 and ERC grant 'WAVETOMO'.

References

Adam, J. and Lebedev, S., Azimuthal anisotropy beneath southern Africa from very broad- band surface-wave dispersion measurements, *Geophys. J. Int.,* 191(1), 155–174, 2012

Capdeville, Y., To, A., and Romanowicz, B., Coupling spectral elements and modes in a spherical Earth: an extension to the 'sandwich' case, *Geophys. J. Int.,* 154(1), 44–57, 2003.

Cottaar S. and B. Romanowicz, Observations of changing anisotropy across the southern margin of the African LLSVP, *Geophys. J. Int*, in revision, 2013.

Megnin, C. and Romanowicz, B., The three-dimensional shear velocity structure of the man-tle from the inversion of body, surface and higher-mode waveforms, *Geophys. J. Int.,* 143(3), 709–728, 2000.

To, A., Romanowicz, B., Capdeville, Y., and Takeuchi, N., 3D effects of sharp boundaries at the borders of the African and Pacific Superplumes: Observation and modeling, *Earth Plan. Sci. Lett.,* 233(1-2), 1447–1460, 2005.

Wuestefeld, A., Bokelmann, G., Zaroli, C., and Barruol, G., SplitLab: A shear-wave splitting environment in Matlab, Comput. Geosci., 34(5), 515–528, 2008.

9 The Application of the Local Slant-Stack Filters (LSSF) for High Resolution Upper Mantle Discontinuity Imaging

Zhao Zheng, Sergi Ventosa and Barbara Romanowicz

Introduction

Several discontinuities (primarily the 410-km and the 660-km) are present in the Earth's upper mantle. Their existence and characteristics provide important constraints on the temperature, composition and dynamics of the mantle. To image these discontinuities on global and regional scales, one effective tool is the SS precursors (e.g. *Shearer*, 1991). They are the underside reflections at the mantle discontinuities (Figure 2.9.1). One major advantage of the SS precursors, compared to the other data types such as receiver functions and triplications, is that they are sensitive to the structure at the midpoint of reflection, and therefore provides good coverage for the vast oceanic areas.

Despite the advantage, there are a few challenges that limit the resolution of the discontinuity images obtained from SS precursor studies. First of all, the precursors are weak in amplitude (typically 5-10% of the SS main phase), often at or below noise level. Stacking therefore is necessary. In practice, common-midpoint (CMP) stacking over rather large geographic bins (radius of 10° or 5°) has been common (for a review, see *Deuss*, 2009), which limits the resolution. Secondly, the SS precursors suffer from interference from other seismic phases, such as the postcursors of S_{diff} (or S at shorter distances) and the precursors to ScSScS. To avoid this issue, common practice has been to limit the epicentral distance of data selection to the "safe ranges," for example, 95-115° and 140-145°, although theoretically speaking the entire range of 80-160° is usable. This has reduced the amount of available data by a significant fraction and may have degraded the sampling density and led to loss of resolution.

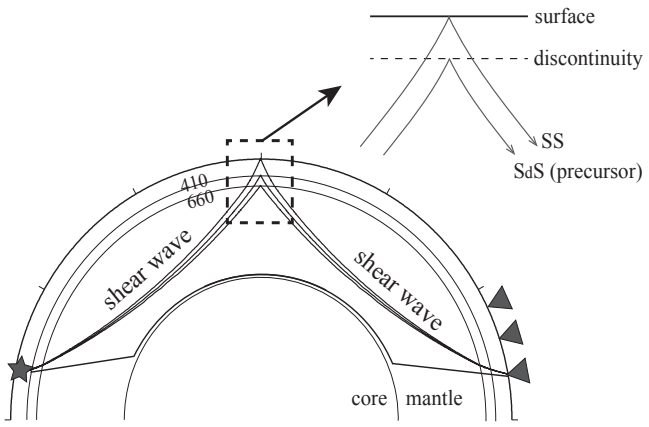

Figure 2.9.1. The ray paths of SS and its precursors. The SS precursors are reflected shear waves off the bottom side of the discontinuities in the Earth's upper mantle.

In recent years, the deployment of the much denser USArray (station spacing ~70 km) has provided unprecedented opportunities for higher resolution imaging. To overcome the above-mentioned limitations of SS precursors, here we propose the local slant-stack filter (LSSF) method. In this report, we first introduce the method, then present examples of application to USArray data.

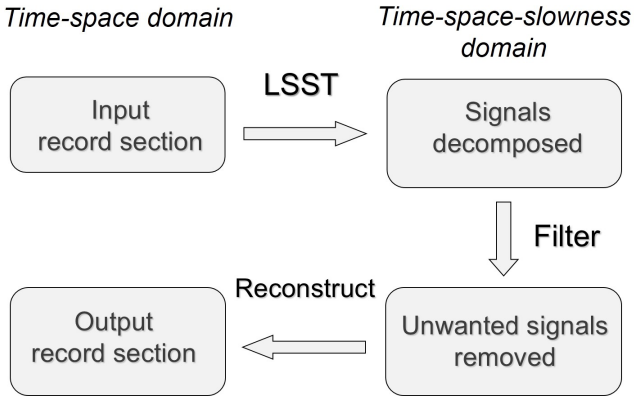

Figure 2.9.2. Workflow of the local slant-stack transform and filtering.

The Local Slant-Stack Filters

Slant stacking is commonly used in seismic signal processing. It aims to detect the slowness(es) of coherent signal(s) present in a given record section by maximizing the stacked amplitude (or other measures of energy). The stacked amplitude plot is also known as a "vespagram." The local slant-stack filters (LSSF) are based on the localized slant stack transform (LSST. *Ottolini*, 1983; *Harlan et al.*, 1984; *Bohlen et al.*, 2004; *Shlivinski et al.*, 2005). It loops over all the traces in the entire record section, and conducts one slant stacking in the vicinity of each trace. The input record section is thus transformed from the time-space domain to the time-space-slowness domain. Filters are then applied in the latter domain to extract or mask out a coherent signal(s) that has a desired slowness and appears at a specified time and spatial location. For example, in the case of this study, the SS precursors have slownesses that is very close to that of the SS (difference < ±0.5 s/deg predicted for PREM), while the interfering phases (S_{diff} postcursors and ScSScS precursors) have distinctively different slownesses (difference >2 s/deg). A filter can therefore be designed to preserve the SS slowness range and mask out the unwanted ones. Random noise has low coherence and can be easily removed. After the filtering, the record section is converted back to the time-space domain through a reconstruction process. The workflow of LSSF is summarized in Figure 2.9.2.

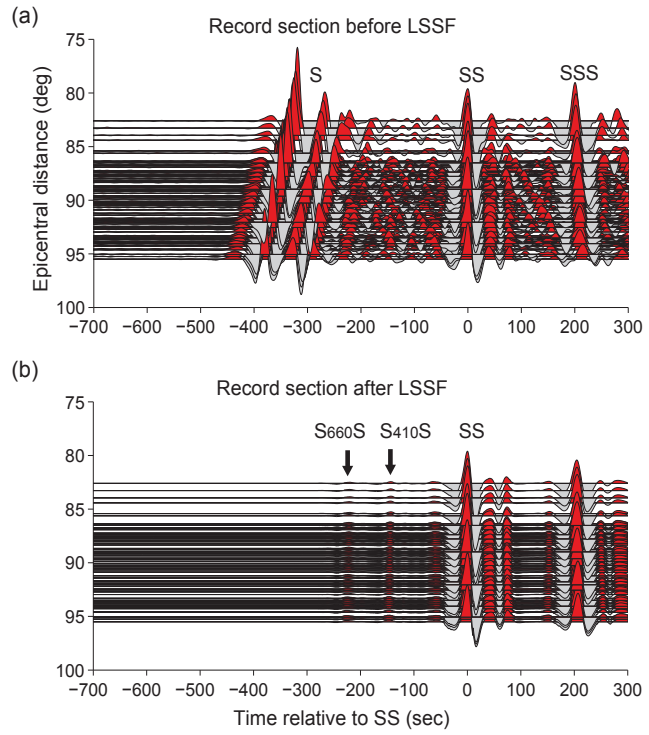

Figure 2.9.3. Record sections of an M_w 7.8 earthquake in Fiji recorded at the USArray, (a) before and (b) after the LSSF filtering.

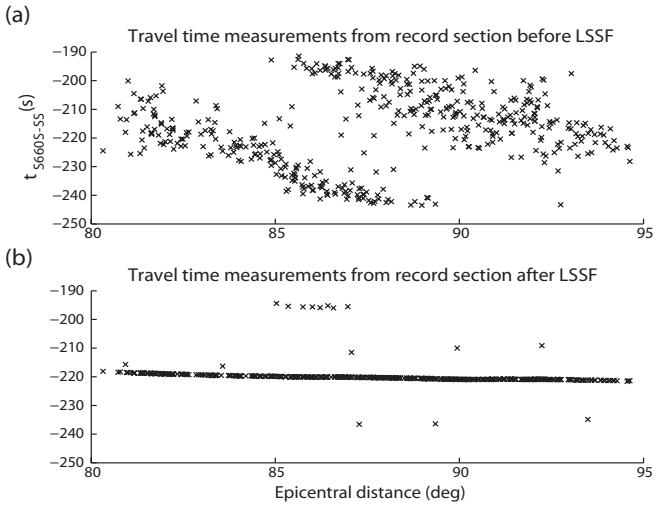

Figure 2.9.4. Differential ($S_{660}S$-SS) travel times measured by cross correlation, from (a) the record section before and (b) after the LSSF filtering. Each cross represents the measurements from one trace.

Application to the USArray Data

Figure 2.9.3(a) shows the record section from an M_w 7.8 earthquake recorded at the USArray. Considering the epicentral distance range, it would have been rejected by conventional SS precursor studies. The SS main phase is clear, however the precursors are not visible due to the strong noise following the S arrival. A vespagram analysis (not shown here due to page limit) indicates the primary content of the noise has a slowness close to that of S, likely to be postcursors of S (S*d*sS and/or Ss*d*S, i.e. the shear wave bouncing once between a discontinuity *d* and the surface, either beneath the source or beneath the receiver). LSSF filters are then applied to the record section. Only the signals that are within the slowness range of ±1 s/deg and that are spatially coherent over a radius of 1.5° are preserved. The filtered record section is shown in Figure 2.9.3(b). The noise is significantly reduced, and the $S_{410}S$ and $S_{660}S$ precursors can now be clearly identified. Their arrival times are in good agreements with the theoretical predictions, confirming the phase identification.

To quantify the improvement of the record section, Figure 2.9.4 compares the travel times of the $S_{660}S$ precursor measured from the record section before and after the LSSF. Before the filtering, the travel time measurements are much more scattered, and the slope of the trend is in agreement with the slowness of S, indicating the measurements are biased by the postcursors of S. After the filtering, the measurements are much more coherent, and have the correct travel time and slowness.

Conclusions

LSSF has proven to be a powerful tool for cleaning up SS precursor record sections and bringing out the weak yet coherent precursor signals. Measurements (for travel time as well as amplitude) can now be done on each trace in the record section, and stacking over large geographic bins is not a necessity any more. Potentially, this will greatly improve the resolution of resultant mantle discontinuity images. The cleaned record sections can be used as input for mature array imaging techniques such as migration.

Acknowledgements

Data were downloaded via IRIS DMC. This study was funded by NSF EAR #0738284. ZZ presented this work at the 2013 SSA conference and the trip was partially supported by the UC Berkeley Student Travel Grant.

References

Bohlen, T., S. Kugler, G. Klein, & F.Theilen, 1.5D inversion of lateral variation of scholte-wave dispersion, *Geophysics, 69*, 330–344, 2004.

Deuss, A., Global observations of mantle discontinuities using SS and PP precursors, *Surv. Geophys. 30*, 301-326, 2009.

Harlan, W. S., J. F. Claerbout, & F. Rocca, Signal/noise separation and velocity estimation: *Geophysics, 49*, 1869–1880, 1984.

Ottolini, R., Signal/noise separation in dip space, *Stanford Exploration Project-37*, 143–149, 1983.

Shearer, P.M., Constraints on upper mantle discontinuities from observations of long-period reflected and converted phases, *J. Geophys. Res., 96*, 18147-18182, 1991.

Shlivinski, A., E. Heyman & A. Boag, A pulsed beam summation formulation for short pulse radiation based on windowed Radon transform (WRT) frames: *IEEE Transactions on Antennas and Propagation, 53*, 3030–3048, 2005.

10 Probabilistic Downscaling of Full Waveform Smooth Tomographic Models: Separating Intrinsic and Apparent Anisotropy

Thomas Bodin, Yann Capdeville, and Barbara Romanowicz

Introduction

The global seismology group at the Berkeley Seismological Laboratory (BSL) has a long history of expertise in the development and application of global imaging using full waveform inversion, leading to several generations of global anisotropic 3D models of the Earth's mantle (*e.g., Li and Romanowicz*, 1996; 2002; *Gung et al.*, 2003; *Panning & Romanowicz*, 2004). In recent years, advances in numerical methods such as the spectral element method (SEM), and increasing computational power, have allowed us to model more accurately the entire seismic wavefield. At the BSL, *Lekic and Romanowicz* (2011) and *French et al.* (2012) recently constructed the first global upper mantle models developed using the spectral element method. However, the heavy computations involved remain a challenge, and the fitted waveforms need to be low pass filtered, which results in an inability to map features smaller than half the shortest wavelength, such as sharp discontinuities.

In this way, the tomographic images can be seen only as a smooth representation of the true Earth. However, they are not merely a simple spatial average of the true model, but rather an effective, apparent, or equivalent model that provides a similar 'long-wave' data fit. For example, it is well known that an isotropic medium with strong gradients will be seen by a long period wave as a smooth anisotropic medium.

Therefore, the observed anisotropy in tomographic models is a combination of intrinsic anisotropy produced by flow-induced lattice-preferred orientation (LPO) of minerals, and apparent anisotropy resulting from the incapacity of mapping discontinuities associated with layering. Interpretations of observed anisotropy (*e.g.*, in terms of mantle flow) therefore require the separation of its intrinsic and apparent components.

The Elastic Homogenization

The relations that link elastic properties of a rapidly varying medium to elastic properties of the effective medium as seen by long waves are the subject of current research (*Guillot et al.*, 2010; *Capdeville et al.*, 2010a,b; *Capdeville & Marigo*, 2013). These homogenization laws have been recently used by tomographers to reduce computational costs when modeling propagation of long waves in a complex medium. That is, given a complex elastic medium, and given a minimum period for the wave equation, a smooth homogeneous equivalent medium can be constructed. The computation of the forward problem (solving the elastic wave equation) can be done in this smooth model, which drastically releases the meshing constraint and reduces the computational cost.

A simple example of homogenization (upscaling) is shown in Figure 2.10.1. Here, only residuals between a reference model (light blue) and a 'real' model (black) are homogenized. This is necessary because, although tomographic models are smoothly parameterized, they are computed relative to a reference model that contains discontinuities (*e.g.*, at 410 km) (*Capdeville et al*, 2013).

The Inverse Homogenization

In the 1D case, *Capdeville et al* (GJI, 2013) recently showed that a tomographic model which results from the inversion of low pass filtered waveforms is a homogenized model, *i.e.*, the same as the model computed by upscaling the true model.

Here we propose a method for the inverse homogenization, or downscaling of smooth tomographic models. The goal is to constrain a discontinuous realistic Earth model, given its observed smooth equivalent. Of course, the solution to the problem is by essence non–unique, *i.e.*, a smooth homogenized effective model is equivalent to a large number of inhomogeneous models with discontinuities. We therefore tackle the problem probabilistically and carry out a stochastic method to sample the ensemble of layered models equivalent to a given tomographic profile. We use a transdimensional formulation where the number of layers is variable (*Bodin et al.*, 2012a,b). Furthermore, each layer may be either isotropic (1 parameter) or intrinsically anisotropic (2 parameters). The parsimonious character of the Bayesian inversion gives preference to models with the least number of parameters (*i.e.*, least number of layers, and maximum number of isotropic layers).

The homogenized model shown in Figure 2.10.1 was downscaled, and results are shown in Figure 2.10.2. This method enables us to distinguish between intrinsic and apparent anisotropy in tomographic models, as layers with intrinsic anisotropy are only present when required by the data.

Acknowledgements

The authors wish to acknowledge support from the Miller Institute for Basic Research at the University of California, Berkeley. We also acknowledge support by the France-Berkeley fund (FBF), a partnership between the government of France and the University of California, at Berkeley

References

Bodin, T., Sambridge, M., Rawlinson, N., and Arroucau, P., Transdimensional tomography with unknown data noise, *Geophysical Journal International* , 2012.

Bodin, T., Sambridge, M., Tkalcic, H., Arroucau, P., Gallagher, K., and Rawlinson, N., Transdimensional inversion of receiver functions and surface wave dispersion, *J. Geophys. Res*, 117, B02301, 2012.

Capdeville, Y. and Marigo, J., A non-periodic two scale asymptotic method to take account of rough topographies for 2-d elastic wave propagation, *Geophysical Journal International*, 192(1),163–189, 2013.

Capdeville, Y., Guillot, L., and Marigo, J., 1-d non-periodic homogenization for the seismic wave equation, *Geophysical Journal International* , 181(2), 897–910, 2010.

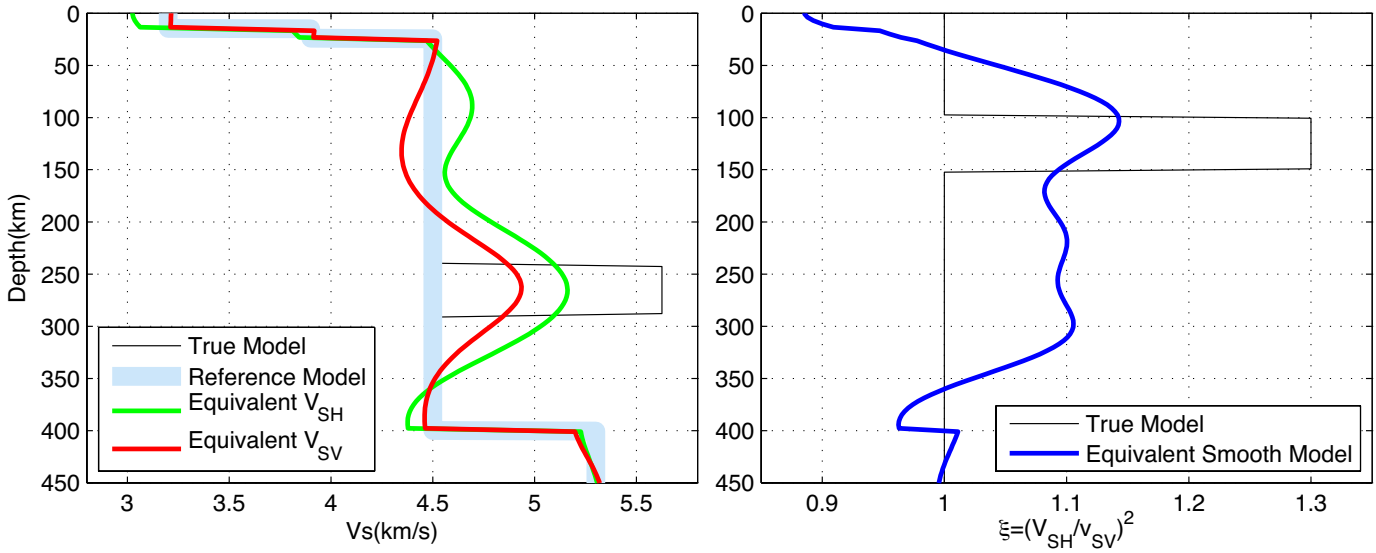

Figure 2.10.1: A true model (black) is defined as the sum of a reference model (light blue) and two anomalous layers. The first layer (100-150 km) contains intrinsic anisotropy (right panel) but does not present changes in the voigt Vs average (left panel). The second layer (250-300 km) is a simple isotropic velocity anomaly. The "residual model" is homogenized. The green (Vsh), red (Vsv), and blue (x) curves represent the smooth equivalent. Note how the two major discontinuities in Vs (250 km and 300 km) are mapped into artificial anisotropy.

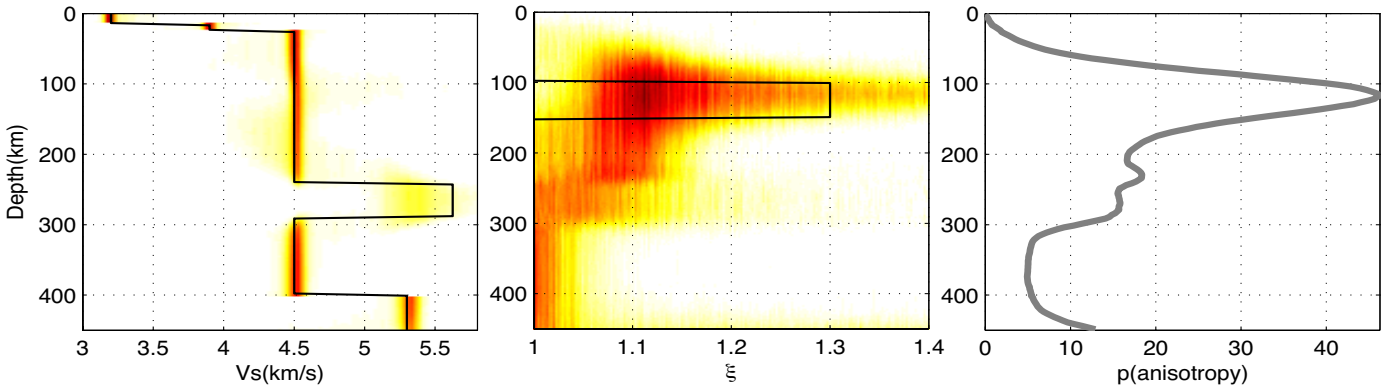

Figure 2.10.2: Probabilistic downscaling of the smooth model in Figure 2.10.1. Left: distribution showing the ensemble solution (true model is in Black). Middle: same thing for parameter x representing the intrinsic radial anisotropy. Right: probability (%) of having an anisotropic layer.

Capdeville, Y., Guillot, L., and Marigo, J., 2-d non-periodic homogenization to upscale elastic media for p–sv waves, *Geophysical Journal International* , 182(2), 903–922, 2010.

Capdeville, Y., Stutzmann, E., Wang, N., Montagner, J.P., Residual homogenization for seismic forward and inverse problems in layered media, 2013.

French, S., Lekic, V., and Romanowicz, B., Spectral-element global waveform tomography: A second-generation upper-mantle model, *AGU Fall Meeting, 2012*.

Guillot, L., Capdeville, Y., and Marigo, J., 2-d non-periodic homogenization of the elastic wave equation: Sh case, *Geophysical Journal International* , 182(3), 1438–1454., 2010.

Lekic, V. and Romanowicz, B., Inferring upper-mantle structure by full waveform tomography with the spectral element method, *Geophysical Journal International* , 185(2), 799–831, 2011.

Li, X. and Romanowicz, B., Global mantle shear velocity model developed using nonlinear asymptotic coupling theory, *Journal of geophysical research*, 101(B10), 22245–22, 1996.

Gung, Y., Panning, M., Romanowicz, B., et al., Global anisotropy and the thickness of continents, *Nature*, 422(6933), 707–711, 2003.

Panning, M. and Romanowicz, B., Inferences on flow at the base of earth's mantle based on seismic anisotropy, *Science*, 303(5656), 351–353, 2004.

11 Mapping Embedded Low-velocity Zones in Permafrost Using Full-wavefield Inversion of Multichannel Surface Waves

Shan Dou, Jonathan Ajo-Franklin (LBNL), Douglas Dreger

Introduction

Permafrost (soils and rocks that stay at or below 0 °C for at least two consecutive years) is an important and yet challenging target for seismic imaging techniques. The challenge lies in the fact that seismic velocities in permafrost are primarily controlled by ice content rather than lithology. A variety of factors, including thermal, chemical, and hydrological cryo-alteration introduce large variations in ice content, a process which yields concomitant sharp contrasts in seismic properties. Because simple layering with normal velocity gradients (increasing velocities with depth) seldom exists in permafrost, body wave refraction imaging is often unable to effectively delineate the velocity structure, particularly in the near-surface where modern thermal processes interface with permafrost structure.

In contrast, surface wave methods do not require abrupt velocity (or impedance) contrasts or normal velocity gradients and thus are amenable for mapping irregular velocity structure in permafrost. However, irregular velocity variations often lead to dominant higher and leaky modes; thus conventional surface-wave inversion methods are inapplicable despite the sensitivity of the technique.

In this study, we apply an unconventional inversion method that uses the complete signal content of the wavefield. Because of the advantages of the full-wavefield method, we are able to infer embedded low-velocity zones from inversely dispersive field data acquired from our permafrost study site at Barrow, Alaska. The low-velocity zones may correspond to embedded cryopegs (hypersaline unfrozen zones), in which ground remains unfrozen or only partially frozen under sub-zero temperatures due to the freezing-point depression effect of salt. The high salt content could have originated from repeated regression and transgression of the Arctic Ocean around 100–350 million years ago (*Thurston et al.,* 1987). Because of the available access to liquid water in cryopegs, cold-adapted microorganisms could maintain their metabolisms under permafrost conditions. The presence of extensive cryopegs at our study site, now confirmed by exploratory sampling, may indicate additional soil carbon degradation occurring in the deep permafrost.

Background

The study site is located within the Barrow Environmental Observatory (BEO) in Alaska (Figure 2.11.1b). The entire area is underlain by continuous permafrost to depths of more than 300 m (*Jorgenson et al.*, 2008).

As part of the Next-Generation Ecosystem Experiments (NGEE-Arctic) project initiated by the U.S. Department of Energy (DOE), we acquired multichannel surface-wave data at the BEO study site during the period of May 11–14, 2012. The field data acquired at the BEO site exhibit inversely dispersive trends (*i.e.* phase velocities increase with increasing frequencies) in both the space-time (x-t) and frequency-velocity (f-v) domains. This suggests that low frequency waves (which penetrate deeper into the ground because of the long wavelength) propagate with slower velocities, and hence the field site is likely to have embedded low-velocity zones/layers.

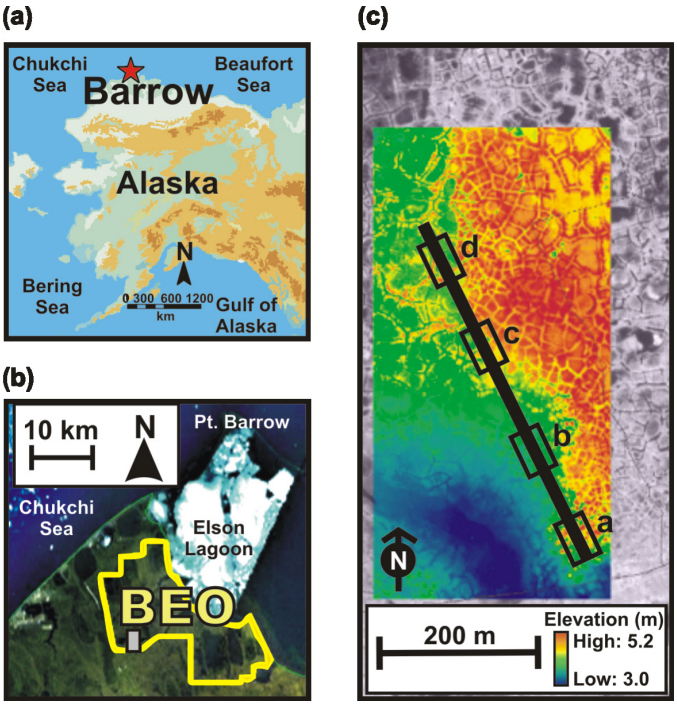

Figure 2.11.1. Site maps: (a) Location of Barrow area, Alaska (red star). (b) The location of the Barrow Environmental Observatory (BEO: yellow outline). The grey box indicates the NGEE-Arctic geophysics site. (c) The 475-meter-long seismic survey line. The black boxes (a, b, c, and d) denote the spatial locations that this study is focused on.

Methods

Conventional surface-wave inversions mostly use kinematic information (in the form of dispersion curves) carried by the wavefield. However, when applied to inversely dispersive media, the energy distribution (including the effect of higher modes, leaky modes, and the data acquisition and processing procedure), in addition to the kinematic information, becomes crucial for surface-wave inversion.

We use a non-linear full-wavefield method as an alternative to exploit the complete signal content of surface waves. Instead of fitting dispersion curves, the entire dispersion spectrum is used to construct the objective function. The nonlinear inverse problem can be framed as an optimization procedure which involves searching for optimal models that minimize the objective function. Because the objective function usually has multiple

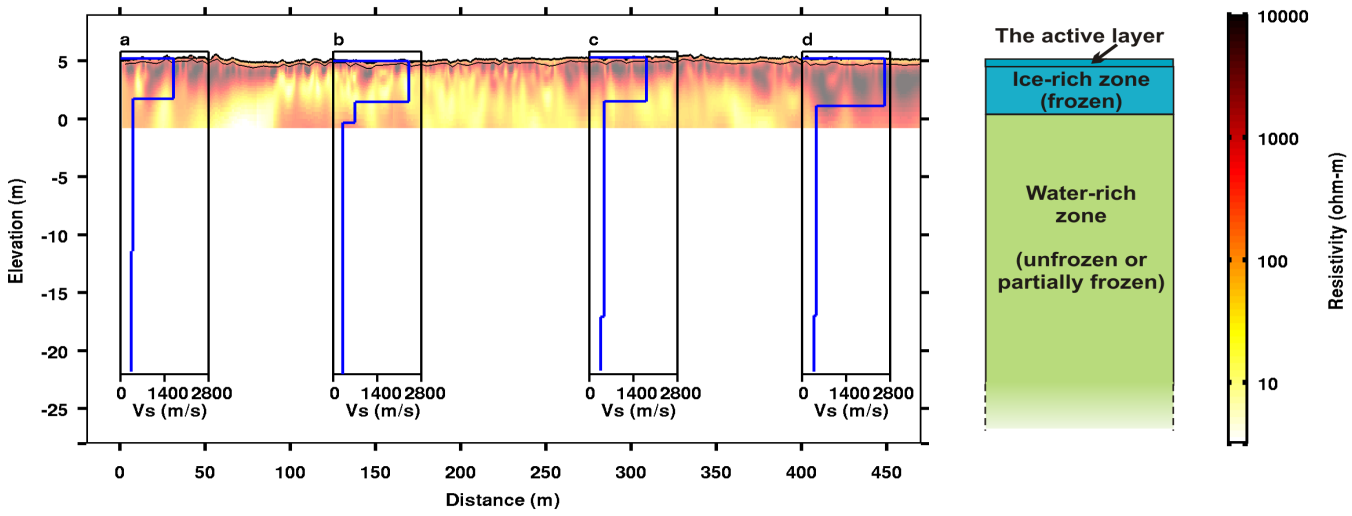

Figure 2.11.2: Comparison of shear-wave velocity profiles and the electrical resistivity tomography (ERT) results (*Hubbard et al.*, 2012). Shear-wave velocity (Vs) profiles (a), (b), (c), and (d) correspond to locations shown as section a, b, c, and d in Fugure 1c. The schematic on the right shows the conceptual model with embedded water-rich zones.

local minima and rugged topography, many commonly-used algorithms that require derivative information are unsuitable. Instead, we adopt derivative-free approaches that only require values, rather than the derivative information, of the objective function. The optimization approach is a hybrid global/local technique which uses a global direct search method to find an approximate optimum solution and a local direct search method (Nelder-Meade) to refine the result.

Results

We apply the full-wavefield inversion method to the field data. The resultant models reveal pronounced low shear-velocity zones (~300–680 m/s) underlying the thin high shear-velocity top-layer (~1700–2400 m/s with thickness ranges around 3.5–4 m). Despite the limited depth penetration of the field data, our inversion indicates these low-velocity zones should extend up to ~25 m below the surface.

We also compare the seismic velocity models with collocated electrical resistivity tomography (ERT) profiles (*Hubbard et al.*, 2012) (Figure 2.11.2). Although the boundaries between high- and low-velocity do not match the boundaries between high- and low-resistivity in an exact way, the first-order layering structures between the two are in good agreement. The consistent results from two different geophysical methods suggest the reliability of the seismic models. These low seismic-velocity (and low electrical resistivity) zones may be constituted of sediments that are unfrozen or only partially frozen.

Acknowledgements

This study was sponsored by the Office of Biological and Environmental Research within the U.S. Department of Energy's Office of Science as part of the Next Generation Ecosystem Experiment (NGEE-Arctic).

References

Hubbard, S.S., C. Gangodagemage, B. Dafflon, H. Wainwright, J. Peterson, A. Gusmeroli, C. Ulrich, Y. Wu, C. Wilson, J. Rowland, C. Tweedie, and S. D. Wullschleger, Quantifying and relating land-surface and subsurface variability in permafrost environments using LiDAR and surface geophysical datasets: *Hydrogeology Journal*, 21, 149-169, 2012.

Jorgenson, M. T., K. Yoshikawa, M. Kanveskiy, Y. L. Shur, V. Romanovsky, S. Marchenko, G. Grosse, J. Brown, and B. Jones, Permafrost characteristics of Alaska: Institute of Northern Engineering, University of Alaska, Fairbanks, 2008.

Thurston, D.K., and L.A. Theiss, Geologic report for the Chukchi Sea planning area, Alaska: U.S. Department of the Interior, Minerals Management Service, Alaska OCS Region, 1987.

12 Probing Deep Rheology Across the Eastern Margin of the Tibetan Plateau: Constraints from the 2008 M_w 7.9 Wenchuan Earthquake

Mong-Han Huang and Roland Bürgmann

Introduction

The fundamental geological structure and rheology of the Tibetan plateau have been debated for decades. Two major models have been proposed: (1) the deformation in Tibet is distributed, and associated with ductile flow in the mantle or lower crustal flow (LCF); (2) the Tibetan plateau was formed during interactions among rigid blocks with localization of deformation along major faults. On 12 May, 2008, a M_w 7.9 earthquake occurred on the Longmen Shan that separates the eastern Tibetan plateau and the Sichuan basin. The earthquake ruptured ~235 km of the Beichuan fault (BCF) and the entire Pengguan fault (PGF) (*Shen et al.*, 2009). Geodetic inversions show more than 5 slip asperities and ~16 m peak slip on SW BCF (Fig. 2.12.1). All of the slip models show oblique thrusting along the SW BCF and a right-slip component gradually increases towards the NE end of the BCF. The postseismic displacement is a response to the redistribution of stresses induced by the earthquake and can be used to probe the deep rheologic properties underneath the surface (*Wang et al.*, 2012). Here we incorporate two-year long geodetic measurements and numerical modeling to examine two end-member hypotheses to provide further evidence to the deep rheology in eastern Tibetan plateau.

The Postseismic Displacement

The GPS measurements show an overall NW-SE convergent displacement in SW BCF, and turn into right lateral strike-slip motion in the NE BCF. This pattern is similar to the coseismic displacement (Fig. 2.12.1), but the peak displacement is about 40 km away from the coseismic surface rupture where the peak coseismic displacement is located (*Shen et al.*, 2009). In the hanging wall, the amplitude of displacement increases from 0-2 cm near the surface rupture to about the location of the Wenchuan-Maowen fault (WMF), and then decays from 5-7 cm at the WMF to 3-4 cm in the far field. Comparing this with the coseismic displacement (black arrows in Fig. 2.12.1), the gradient of the displacement away from the fault is much lower and might imply either a deeper slip on the fault or viscous relaxation from the deeper part of the lithosphere. In the footwall, all of the displacement moves toward the NW and the amplitude is much smaller than in the hanging wall.

Model of the Postseismic Displacement

The afterslip is the continuous slip of the fault after the main shock and is often considered downdip of the fault rupture zone (*Wang et al.*, 2012). We use a dislocation model with layered structures to investigate the afterslip distribution by inverting the geodetic data. We modify the fault geometry proposed by *Shen et al.* (2009) and extend the fault width to 65 km depth for afterslip at the downdip extension (afterslip model in Fig. 2.12.1). The afterslip distributes on both shallow and deep parts of the BCF that represent the fit to both the near, and far field displacement.

We use a 3D finite element model to construct a regional rheologic model composed of an elastic Tibet upper crust and Sichuan crust, a viscoelastic Tibet lower crust, and a viscoelastic upper mantle. We use the bi-viscous Burger's rheology to represent the transient and steady state periods of the postseismic deformation. The Burger's rheology is composed of a Maxwell fluid connected in series with a Kelvin solid to represent the steady state and transient viscosities (η_1 and η_2, respectively). The best-fitting model is composed of the LCF located between 45 and 60 km in depth and can produce more far field postseismic displacement.

The afterslip model can explain the postseismic displacement in the near field but there is larger misfit in the far field. On the other hand, the viscoelastic relaxation model can explain the far field postseismic displacement better than the near field. It appears that a single mechanism cannot solely explain the postseismic displacement. A multiple mechanism model is needed to fit both near, and far field displacements. We consider the 15 km thick LCF to be the main mechanism of the far field displacement, so the afterslip model may explain the misfit of the LCF model. The inversion (the 2nd afterslip model in the lower right in Fig. 2.12.1) of the LCF residual displacement shows a significant reduction of the deep afterslip.

As a result, the afterslip alone model requires more than 45 cm slip in the first year below Tibet's Moho that may already undergo ductile deformation, whereas the viscoelastic relaxation in a 15 km thick LCF can explain the GPS measurements. Consequently, the result of the Wenchuan postseismic displacement supports a weak lower crustal flow underneath eastern Tibet.

Acknowledgements

We thank Prof. Z. Shen of Beijing for providing the GPS measurements. M.-H. Huang thanks Prof. Andrew Freed for instruction on ABAQUS™. This work is supported by the National Science Foundation (grant EAR 0738298).

References

Shen, Z.K., J. Sun, P. Zhang, Y. Wan, M. Wang, R. Bürgmann, Y. Zeng, W. Gan, H. Hiao, and Q. Wang, Slip maxima at fault junctions and rupturing of bariers during the 2008 Wenchuan earthquake, *Nat. Geosci.*, 2, 718-724, doi:10.1038/NGEO636, 2009.

Wang, K., Y. Hu, and J. He, Deformation cycles of subduction earthquakes in a viscoelastic Earth, *Nature*, 484, doi:10.1038/ nature11032, 2012.

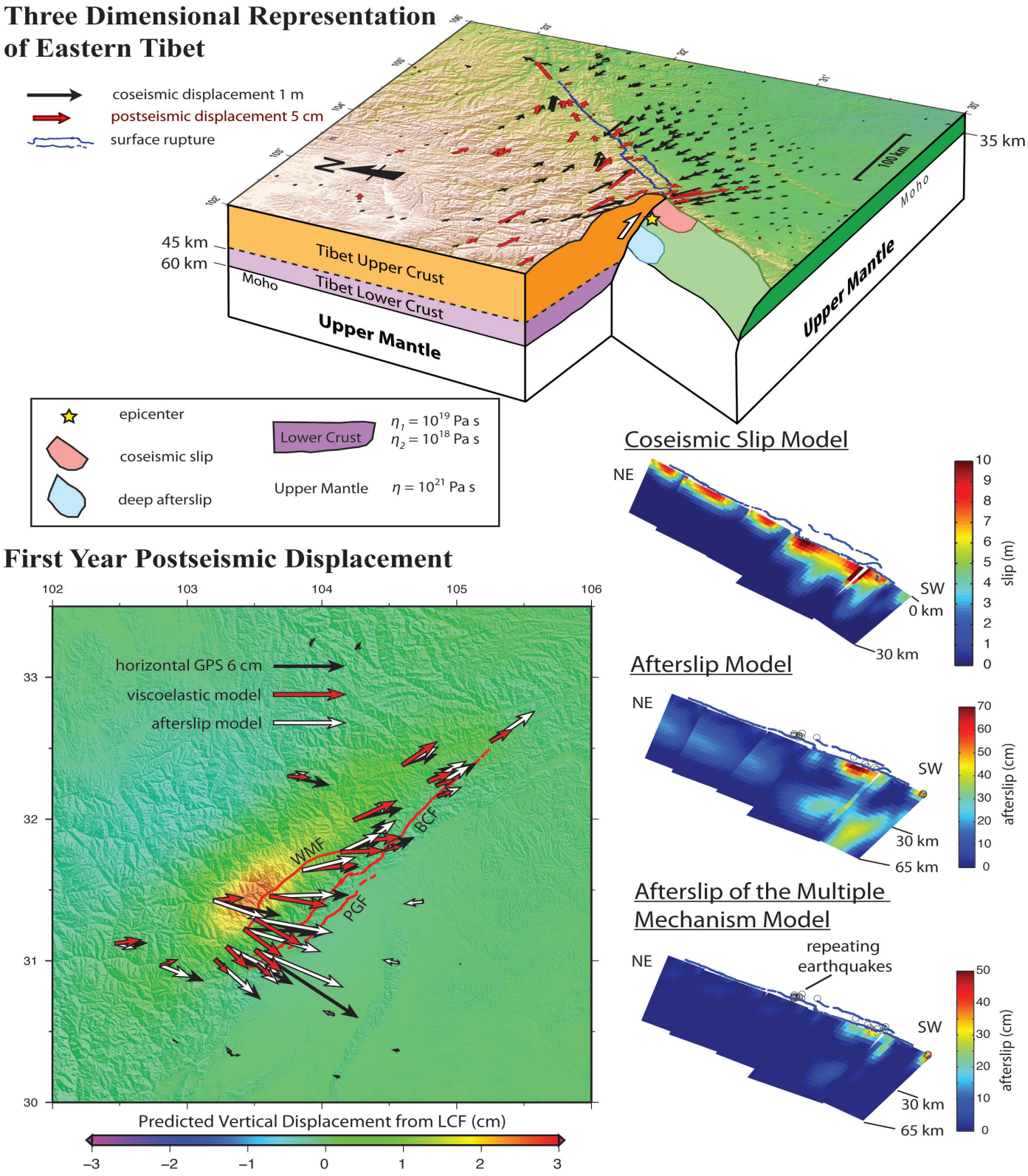

Figure 2.12.1: The 3D representation of the rheologic model in eastern Tibet and western Sichuan basin. These two geologic structures are separated by the Longmen Shan. The co- and postseismic GPS displacements are shown in the black and red arrows, respectively. The two possible mechanisms of the postseismic deformation are: (1) deep afterslip (the light blue region), and (2) lower crustal flow (the purple layer). The coseismic slip is inverted from the coseismic GPS measurements. In the lower left, the postseisic displacement during the first year is compared with the two end-member mechanisms. The two afterslip models in the lower right are inverted from the one year postseismic GPS measurements and from the LCF model residual, respectively. The deep afterslip in the multiple mechanism model is largely reduced (see text).

13 Viscoelastic Postseismic Deformation Following the 2011 M_w 9.0 Tohoku Earthquake

Yan Hu, Roland Bürgmann

Introduction

On March 11th, 2011, the surprisingly large M_w 9.0 Tohoku earthquake ruptured the interface of the subducting Pacific Plate over an area approximately 400 km long and 200 km wide and produced a devastating tsunami. As a result of the earthquake, five marine GPS-acoustic stations recorded more than 50 meters seafloor displacements near the trench (*Fujiwara et al.*, 2011). This was a first. Inversions from land and seafloor geodetic data, as well as teleseismic data, show that portions of the megathrust slipped as much as 80 meters (*e.g.*, *Ozawa et al.*, 2011; *Iinuma et al.*, 2012) (solid contours in Figure 2.13.1a). Viscoelastic relaxation in the upper mantle of the shear stresses induced by the earthquake, and aseismic afterslip of the megathrust both contribute to the very rapid crustal deformation observed since the earthquake. Land GPS stations have recorded more than one meter postseismic displacements in two years since the earthquake (red arrows in Figure 2.13.1a). The geodetic data in NE Japan, with unprecedented high spatial and temporal resolution, provide a unique opportunity to explore the rheological structure of the upper mantle and behavior of the megathrust in earthquake cycles.

In this ongoing research, we integrate the wealth of geodetic data from NE Japan and modeling experiences developed at other margins (*Hu and Wang*, 2012; *Wang et al.*, 2012) to investigate the effects of mantle rheology on postseismic deformation following the 2011 earthquake.

Finite Element Model

Newtonian-Maxwell rheology has been widely used to describe slow viscoelastic relaxation of the mantle in earthquake cycle deformation models and studies of postglacial rebound. In this work, we assume that the upper mantle is represented by the bi-viscous Burgers rheology that is able to describe slow, long-term deformation as well as very rapid, short-term transient deformation. A bi-viscous Burgers element consists of a Maxwell element (steady-state viscosity) in parallel with a Kelvin element (transient viscosity) (*Bürgmann and Dresen*, 2010).

We use a three dimensional (3D) finite element model (FEM) that is able to incorporate the complex slab geometry and tectonic structure in the real Earth. The model shown in Figure 2.13.1b consists of an elastic upper plate, an elastic subducting plate, a viscoelastic continental mantle wedge, and a viscoelastic oceanic upper mantle. Reference rock properties of each tectonic unit are also labeled in Figure 2.13.1b.

A common approach of studying afterslip is to invert the postseismic surface displacements, or the residual between observations and mantle-relaxation-model predicted motions, for distributed slip on the subduction thrust in an elastic half-space. In reality, however, afterslip is stress driven and time dependent. The conventional approach neglects the significant

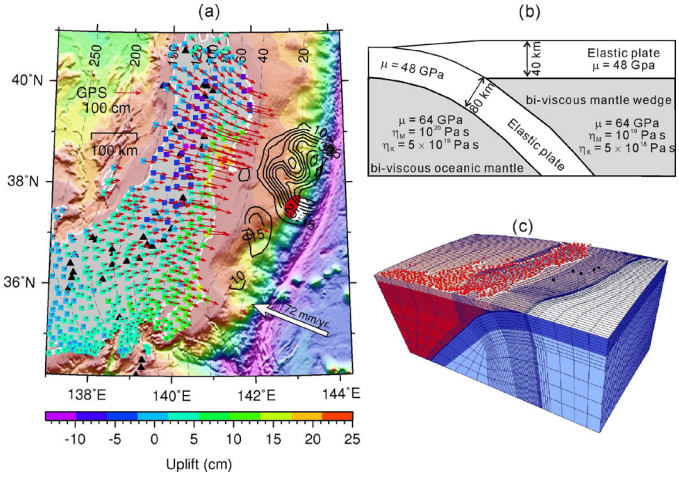

Figure 2.13.1: (a) Horizontal (red arrows) and vertical (colored contours) two-year postseismic displacements observed at land GPS stations in NE Japan. Marine GPS data (red arrows) are one year postseismic displacements. Solid contours are coseismic slip distributions at 10-meter intervals (*Iinuma et al.*, 2012). Labeled dashed lines represent the depth of the subduction interface. (b) Schematic diagram of finite element model (after *Hu and Wang*, 2012). Each tectonic unit is labeled with its rock properties. (c) Central part of the finite element mesh. Red and black dots represent locations of land and marine GPS stations, respectively. Thick white lines denote the coastline.

relaxation of the upper mantle due to the afterslip itself and the contribution of mantle relaxation to driving afterslip. In this work, we use a narrow weak shear zone with low viscosity that is attached to the subduction interface to simulate the afterslip. Because coseismic slip of the fault induces shear stress in the shear zone, subsequent viscoelastic relaxation of the shear zone gives an approximation of the stress-driven afterslip of the fault.

Following the approach of developing the FEM mesh in *Hu and Wang* (2012), we manually derived thirty-two latitude-parallel profiles based on published slab geometry data (*e.g.*, *Nakajima and Hasagawa*, 2006), relocated seismicity, and locations of the trench and the arc. These profiles were then used to construct the finite element mesh. The central part of the mesh is shown in Figure 2.13.1c.

Model Results

In our preliminary model, based on results deduced from post-2004 Sumatra earthquake deformation (*Hu and Wang*, 2012), steady-state and transient viscosities of the continental mantle wedge and the oceanic mantle are shown in Figure 2.13.1b. Steady-state and transient viscosities of the shear zone are 10^{17} and 10^{16} Pa s, respectively. The shear zone is attached to portions of the fault where the coseismic slip is less than five meters, and the afterslip zone terminates at 120 km depth.

Our model successfully reproduces the first-order pattern of

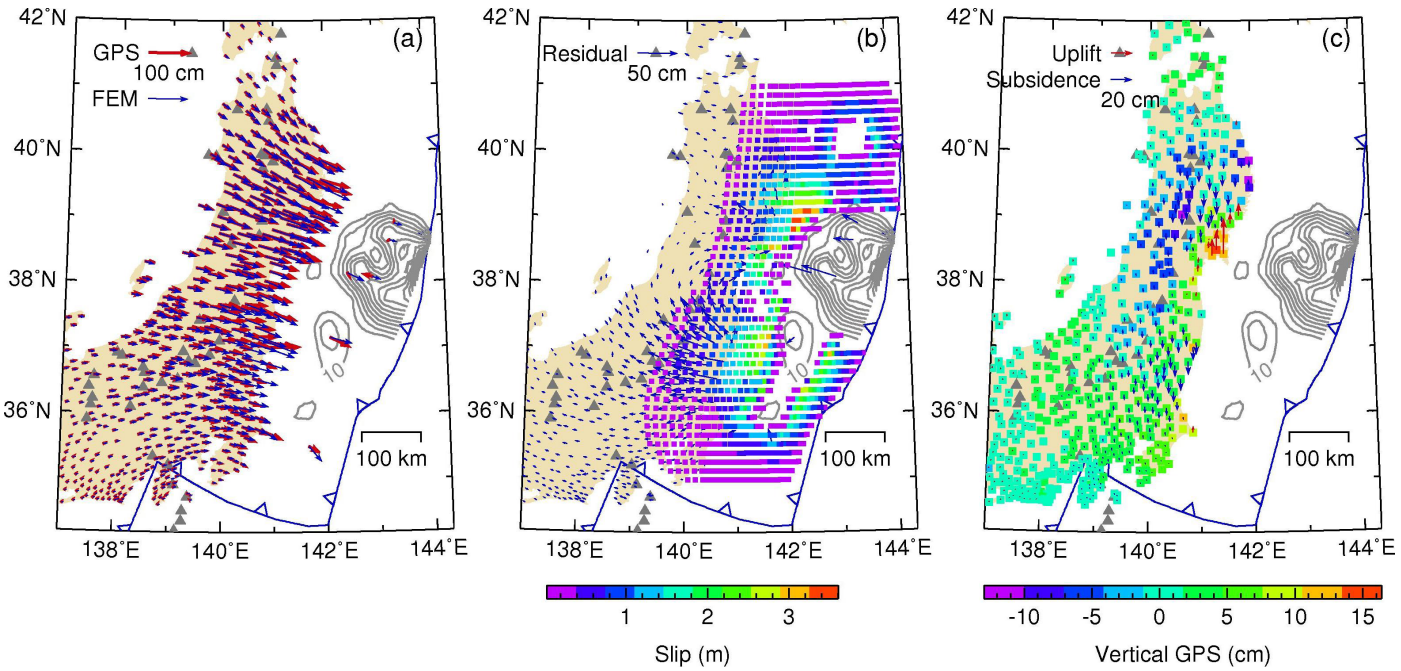

Figure 2.13.2: Comparison of postseismic GPS observations with model-predicted results one year since the earthquake. (a) Horizontal displacements. Red and blue arrows represent GPS observations and model-predicted displacements, respectively. (b) Residual between GPS observations and model-predicted results shown in (a). Colored contours represent cumulative slip of the shear zone. (c) Vertical displacements. Red and blue arrows represent model-predicted uplift and subsidence, respectively. Colored rectangles represent vertical GPS observations. Gray solid contours represent the coseismic slip of the 2011 earthquake, also shown in Figure 2.13.1a.

the observed horizontal (Figure 2.13.2a) and vertical (Figure 2.13.2c) displacements one year since the 2011 earthquake. In particular, the model predicts the order of magnitude of displacements at five marine GPS sites well (Figure 2.13.2a). The model has indicated that afterslip of the fault slows down logarithmically with time. The fault undergoes continuous afterslip of up to about three meters in the first six months since the earthquake and up to about four meters in two years (results not shown).

We have also studied the effects of two elastic subduction slabs in the south by taking into account the subducting Philippine Sea Plate and weaker lower crust below the volcanic arc. Such structure heterogeneity has minimum effects on the postseismic deformation of the 2011 Tohoku earthquake (results not shown). We are also using repeating earthquakes that periodically rupture the same segments of the megathrust (*Uchida and Matsuzawa*, 2013) to improve the constraints on the location and rheology of the shear zone.

Acknowledgements

We thank Paramesh Banerjee for providing processed daily GPS time series of land stations by the Geospatial Information Authority (GSI) of Japan and Kelin Wang's group at Pacific Geoscience Center, Geological Survey of Canada for the finite element code. This work is funded by NSF grant no. 1246850.

References

Bürgmann, R., and G. Dresen, Rheology of the lower crust and upper mantle: Evidence from rock mechanics, geodesy, and field observations, *Annu. Rev. Earth Planet. Sci.*, *36*, 531–567, doi:10.1146/annurev.earth.36.031207.124326, 2008.

Fujiwara, T., S. Kodaira, T. NO, Y. Kaiho, N. Takahashi, and Y. Kaneda, The 2011 Tohoku-Oki Earthquake: Displacement Reaching the Trench Axis, *Science*, *334*, 1240, doi:10.1126/science.1211554, 2011.

Hu, Y., and K. Wang, Spherical-Earth finite element model of short-term postseismic deformation following the 2004 Sumatra earthquake, *J. Geophys. Res.*, *117*(B5), B05404, doi:10.1029/2012JB009153, 2012.

Iinuma, T., et al., Coseismic slip distribution of the 2011 off the Pacific Coast of Tohoku Earthquake (M9.0) refined by means of seafloor geodetic data, *J. Geophys. Res.*, *117*, B07409, doi:10.1029/2012JB009186, 2012.

Nakajima, J., and A. Hasegawa, Anomalous low-velocity zone and linear alignment of seismicity along it in the subducted Pacific slab beneath Kanto, Japan: Reactivation of subducted fracture zone? *Geophys. Res. Lett.*, *33*, L16309, doi:10.1029/2006GL026773, 2006.

Ozawa, S., T. Nishimura, H. Suito, T. Kobayashi, M. Tobita, and T. Imakiire, Coseismic and postseismic slip of the 2011 magnitude-9 Tohoku-Oki earthquake, *Nature*, *475*, 373–376, doi:10.1038/nature10227, 2011.

Uchida, N., and T. Matsuzawa, Pre- and postseismic slow slip surrounding the 2011 Tohoku-oki earthquake rupture, Earth Planet. Sci. Lett., doi:10.1016/j.epsl.2013.05.021i, 2013.

Wang, K., Y. Hu, and J. He, Deformation cycles of subduction earthquakes in a viscoelastic Earth, *Nature*, *484*, 327-332, doi:10.1038/nature11032, 2012.

14 Ambient Seismic Noise Monitoring for Stress-Induced Changes in the Geysers Geothermal Field, California

Voon Hui Lai, Taka'aki Taira, Douglas Dreger

Introduction

The Geysers Geothermal Field in California is one of the most seismically active zones in North America. We investigate the temporal change of the stress field within this region, by analyzing the small perturbations of the velocity structure through the correlations of ambient seismic noise. The cross correlation of ambient noise recorded between two stations over a period of time is used to extract the impulse response or the Green's function between the stations (*Shapiro and Campillo*, 2004), which can then be used to detect temporal changes in seismic velocity. We are particularly interested in detecting temporal perturbations associated with seismic velocity structure accompanying tectonic events and fluid injections.

Methodology

For this study, we follow closely the ambient noise data processing procedure described in *Seats et al.* (2012). Our procedure consists of three phases: (1) preparation of single station seismic record, (2) cross-correlation of the data between two stations and temporal stacking, and (3) measurement of the travel time shift.

Preparation

Vertical components of the continuous record of seismic noise for over 12 months are obtained from an array of seismic stations operated by the Lawrence Berkeley National Laboratory (LBNL). This network contains 30 seismic stations distributed over the entire Geysers geothermal field with an average station distance of 2 to 3 km. This translates into 435 possible pair combinations of the stations in which some pairs have overlapping paths that allow us to verify the consistency of the Green's function along the same path.

The instrument response, mean, and trend are removed from the raw data, and a 0.1-0.9 Hz band-pass filter is applied. Finally, a whitening procedure is applied to broaden the frequency band of ambient seismic noise. For the output data, we test a few different sampling rates (20, 50 and 100 Hz) and determine that 20 Hz is the most optimum rate, with the greatest amplitude for the Green's function extracted in a frequency range of 0.1 Hz to 0.9 Hz (see Figure 2.14.2).

Cross-correlation and Stacking

We compute hourly cross-correlations of the seismic noise between two stations and stack the correlations into 1-day and subsequently 30-day stacks to obtain a reference Green's function (RGF) with high signal to noise ratio. Overlapping time windows are used to reduce any dependencies or effects of high amplitude transient signals (*Seats et al.*, 2012).

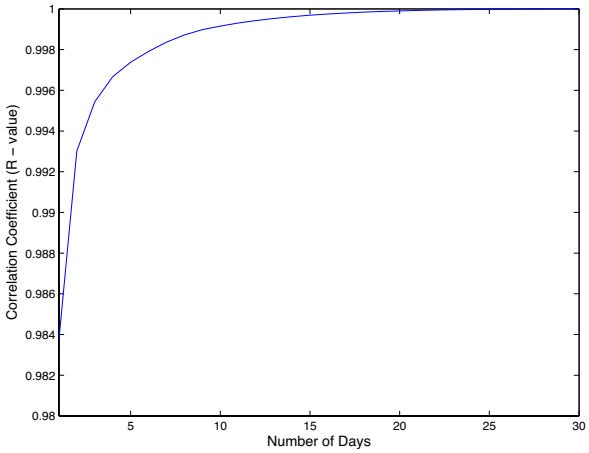

Figure 2.14.1: The mean correlation coefficient (R-value) of a month-long RGF against the stacked correlation in different numbers of consecutive days. The result shows the stacked correlation achieves a very high R-value (0.999) and begins to stabilize after a short period of 9 cumulative days.

Measurement

We estimate the relative travel time shift between the RGF and the 30-day stacked correlations in the frequency range from 0.1 to 0.9 Hz by computing a local travel time shift between the two Green's functions and measuring the slope of the travel time shifts as a function of lapse time. If the structure experiences a spatially homogeneous relative seismic velocity change due to tectonic events or fluid injections, the relative velocity change will be the opposite value of the relative travel time shift (*Brenguier et al.*, 2008). The relative velocity change is typically small (less than 1%).

Discussion

On occasion, continuous data may contain gaps due to various technical problems such as failed data loggers and telemetry dropouts. As a result, these data that contain gaps are removed from the analysis. To ensure the reliability of our correlations, we perform a synthetic noise analysis by calculating the mean correlation coefficient (R-value) of a month-long RGF against the stacked correlation in different numbers of consecutive days. We find that the resulting R-value exceeds 0.999 with a 9-day stack of Green's functions (Figure 2.14.1). This shorter time window would allow us to examine time-varying seismic structure with a high temporal resolution. We plan to follow up with a more rigorous analysis to better reflect the actual data condition that includes rejected hourly data in random days in the month.

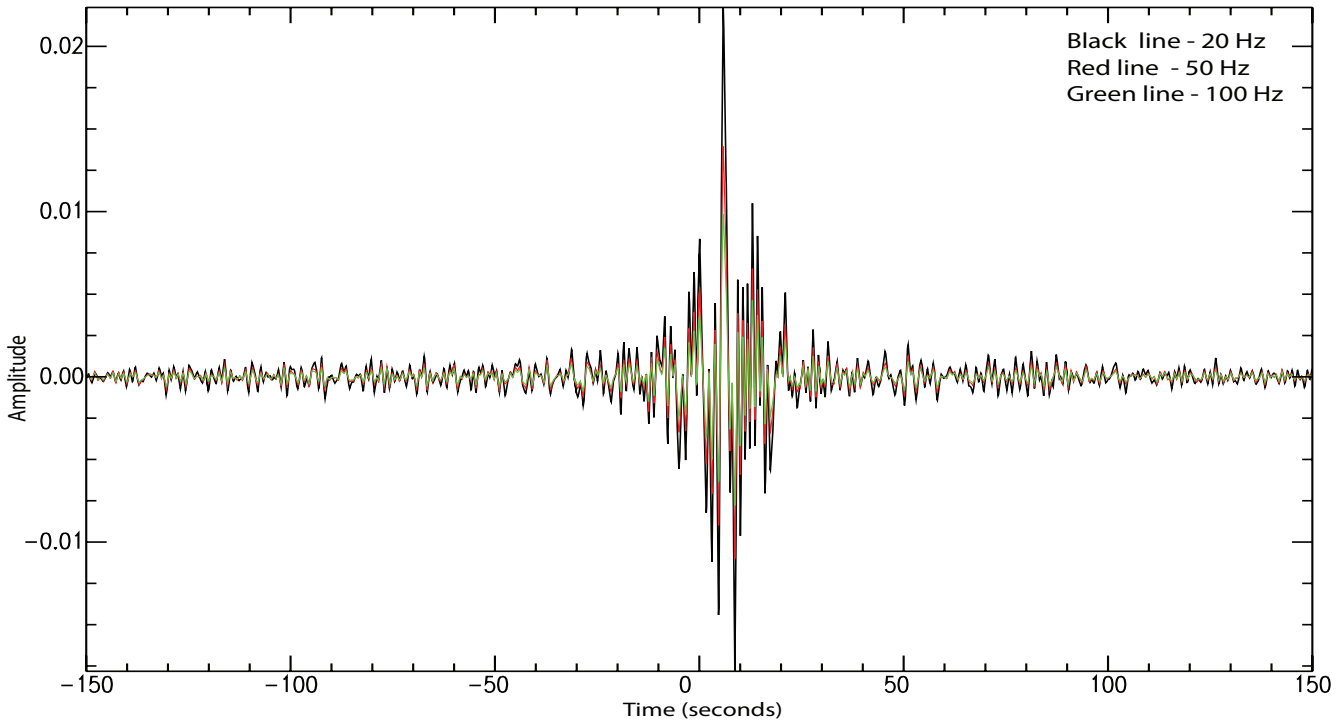

Figure 2.14.2: Stacked correlations of the same station pairs using different output sampling rates (20, 50, and 100 Hz). The resulting three outputs show great similarity in Green's function. The 20 Hz output marked with a black line shows the largest amplitude.

We also observe several gaps in the hourly data that span less than a minute. An alternative to minimize the loss of rejected data is to reduce our time window by preparing 30 minute-long data instead of hourly data. However, there will be a trade-off between retaining data and computational time.

The relative seismic velocity change within the structure after tectonic events (*e.g., Brenguier et al.*, 2008) and fluid injection can provide information about stress changes in seismogenic zones such as the Geysers. As a follow up to this study, we will revisit important assumptions, in particular the ambient seismic noise source, in order to have a greater confidence in our result.

Acknowledgements

This work is funded by the National Science Foundation under award number NSF, EAR-1053211. We would also like to thank A. Nayak and S.H. Yoo for their support.

References

Brenguier, F., N. M. Shapiro, M. Campillo, V. Ferrazzini, Z. Duputel, O. Coutant and A. Nercessian, Towards forecasting volcanic eruptions using seismic noise. *Nature Geoscience*, Vol 1, Issue: 2, p. 126-130, 2008.

Brenguier, F., M. Campillo, C. Hadziioannou, N. M. Shapiro, R. M. Nadeau, E Larose, Postseismic Relaxation Along the San Andreas Fault at Parkfield from Continuous Seismological Observations. *Science, Vol. 321*. P. 1478- 1481, 2008.

Seats, K. J., J. F. Lawrence and G. A. Prieto, Improved Ambient noise correlation functions using Welch's method. *Geophys. J. Int. 188*, 513-523. doi: 10.1111/j.1365-246X.2011.05263.x, 2012.

Shapiro, N. M. and M. Campillo, Emergence of broadband Rayleigh waves from correlations of the ambient seismic noise. *Geophys. J. Int. 31*, L07614, doi: 10.1029/2004GL019491, 2004.

15 Automated Measurement of P- and S-Wave Differential Times for Imaging Spatial Distributions of the Vp/Vs Ratio with a Moving-Window Cross-Correlation Technique

Taka'aki Taira and Aitaro Kato (Earthquake Research Institute, University of Tokyo)

Introduction

A high-resolution Vp/Vs ratio estimate is one of the key parameters needed to understand spatial variations in composition and physical states within the Earth. *Lin and Shearer* (2007) recently developed a methodology to obtain local Vp/Vs ratios in individual similar earthquake clusters, based on P- and S-wave differential times. A waveform cross-correlation approach is typically employed to measure those differential times for pairs of seismograms from similar earthquake clusters, at narrow time windows around the direct P- and S-waves. This approach effectively collects P- and S-wave differential times and requires the robust P- and S-wave time windows that are extracted to be based on manually or automatically picked P- and S-phases. We present another technique to estimate P- and S-wave differential times by exploiting temporal properties of delayed time as a function of elapsed time on the seismograms with a moving-window cross-correlation analysis (*e.g.*, *Snieder*, 2002; *Niu et al.*, 2003).

Methodology

Following *Lin and Shearer* (2007), Vp/Vs ratio within similar earthquake clusters can be expressed as

$$\left(\delta t_s^i - \delta \bar{t}_s\right) = \left(V_p/V_s\right)\left(\delta t_p^i - \delta \bar{t}_p\right) \qquad (1.1)$$

where δt_p^i and δt_s^i represent the P- and S-wave differential times for a single pair of earthquakes in a cluster obtained from the station *i*, respectively, and $\delta \bar{t}_p$ and $\delta \bar{t}_s$ are the median values of the P and S differential times from all stations.

We use a moving-window cross-correlation analysis to measure S-wave differential time. In this analysis, we evaluate time evolutions of delay times from a pair of similar earthquakes. Two seismograms aligned by the direct P-waves yield that delayed times become zero around the direct P-wave. In contrast, delayed times obtained from time windows including the direct S-wave have a non-zero value.

Our approach, in principle, is capable of measuring both P- and S-wave differential times from single-component seismograms. In an ideal case, the temporal evolution of delayed time becomes a step function with its discontinuity at the onset of the direct S-wave. The offset or constant delay time (dt) in the resulting step function would be the S-wave differential time, relative to the P-wave differential time as the two waveforms are aligned by the direct P wave.

$$dt^i = \delta t_s^i - \delta t_p^i \qquad (1.2)$$

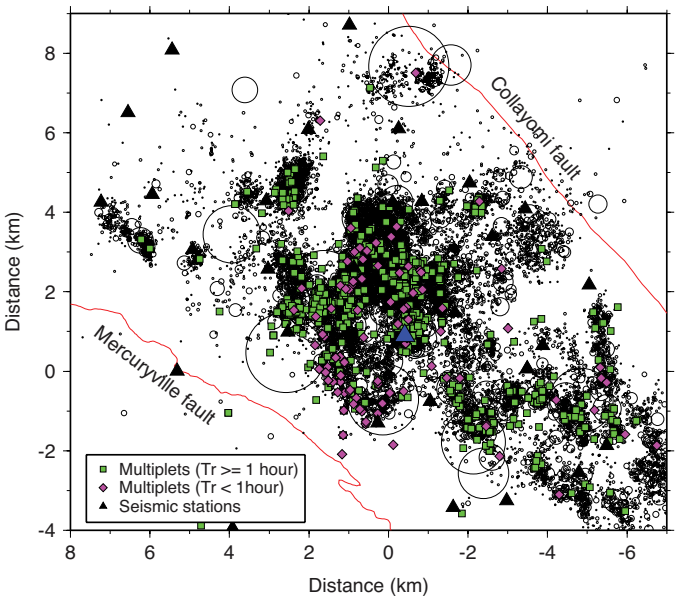

Figure 2.15.1: Map view of the Geysers similar event clusters (multiplets) identified in our analysis. Green squares and purple diamonds are the multiplets with longer (≥1 hour) and shorter (< 1 hour) recurrence intervals, respectively. The Black triangles are the LBNL and USGS seismic stations. The Blue triangle is station GDXB. Broadband data from station GDXB were used to identify the Geysers multiplets. Black circles are locations of relocated earthquakes in this area during 1984 to 2008 (*Waldhauser and Schaff*, 2008). Circle sizes are proportional to earthquake rupture sizes.

Analysis

We apply our moving-window cross-correlation technique to the two different data sets collected at: 1) the Wakayama district, Japan and 2) the Geysers geothermal field, California (Figure 2.15.1). Both of the target areas are characterized by earthquake swarms that provide a number of similar event clusters.

We use the following automated procedure to systematically analyze the two data sets: 1) identifying the direct P arrivals on the vertical component data by using an Akaike Information Criterion based on a phase picking algorithm introduced by *Zhang et al.* (2003), 2) performing the waveform alignment by the P-wave with a waveform cross-correlation to obtain the P-wave differential time, δt_p^i, 3) the moving-time window analysis to estimate the S-wave differential time, $\delta \bar{t}_s$(Figure 2.15.2).

Kato et al. (2010) have estimated the Vp/Vs ratios for a few similar earthquake clusters from the Wakayama data set, by a conventional approach to obtain differential times. As shown in Figure 2.15.3, we find that the resulting Vp/Vs ratios from

our approach for the same earthquake clusters are comparable

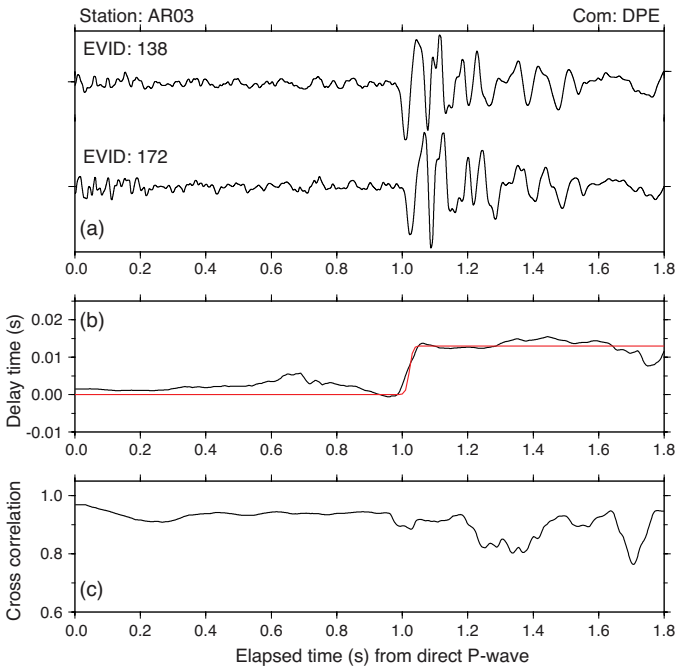

Figure 2.15.2: S-wave differential times measurement with a moving-window cross-correlation analysis. (a) Observed seismograms recorded at station AR03 in the east-west component for two Wakayama local earthquakes (evnet-ids 138 and 172). Waveforms are aligned by the direct P-wave. The resultant P-wave differential time is -0.0239 s. Amplitudes are normalized by their maximum amplitudes. (b) Delay time and (c) cross-correlation value from a moving-window cross-correlation analysis. Red line shown in (b) is the best fit step function with the offset of 0.0123 s. Using equation (15.2), the resulting S-wave differential time is -0.0116 s.

with those obtained from *Kato et al.* (2010). We also find that the moving-window cross-correlation technique effectively measures both P- and S-wave differential times for the seismograms in which the clear P- and S-phases are not observed.

Acknowledgements

We thank the Northern California Earthquake Data Center and the Lawrence National Berkeley Laboratory for data collection and distribution for the Geysers seismic data. This work is supported by the National Science Foundation grant EAR-1053211.

References

Kato, A., S. Sakai, T. Iidaka, T. Iwasaki, and N. Hirata, Non-volcanic seismic swarms triggered by circulating fluids and pressure fluctuations above a solidified diorite intrusion, *Geophys. Res. Lett., 37*, L15302, doi:10.1029/2010GL043887, 2010.

Lin, G., and P.M. Shearer, Estimating local Vp/Vs ratios within similar earthquake clusters, *Bull. Seismol. Soc. Am., 97*, 379–388, 2007.

Niu, F., P.G. Silver, R.M. Nadeau, and T.V. McEvilly, Stress-Induced Migration of Seismic Scatterers Associated with the 1993 Parkfield Aseismic Transient Event, *Nature, 426*, 544-548, 2003.

Snieder, R, Coda wave interferometry and the equilibration of energy in elastic media. *Phys. Rev. E., 66*, 046615, 2002.

Waldhauser, F. and D.P. Schaff, Large-scale relocation of two decades of Northern California seismicity using cross-correlation and

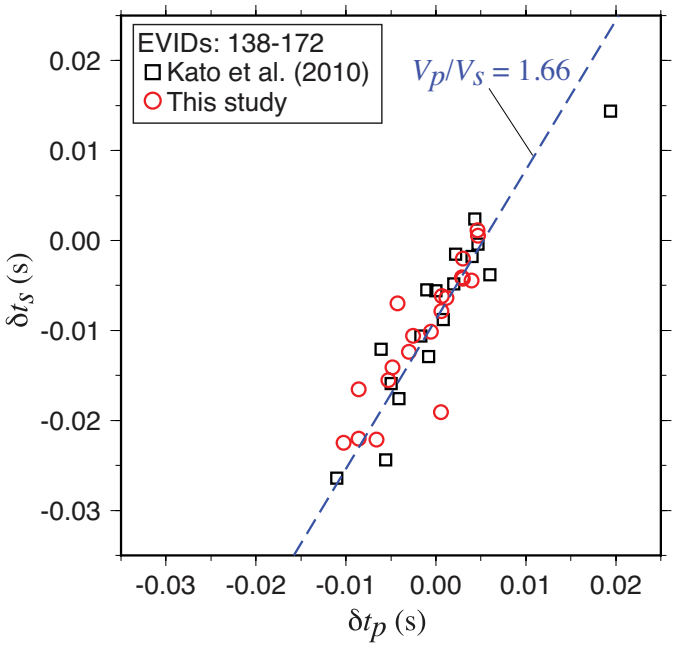

Figure 2.15.3: P differential arrival times versus S differential arrival times for a single pair of events investigated by *Kato et al.* (2010). Black squares and red circles are the P and S differential time measurements by *Kato et al.* (2010) and our study, respectively. The blue dashed line passing through the points is the best fitting line from a least-squares method. The slope of the line is 1.66, which is the resulting Vp/Vs ratio.

double-difference methods, *J. Geophys. Res., 113*, B08311, doi:10.1029/2007JB005479, 2008.

Zhang, H.J., C. Thurber, and C. Rowe, Automatic P-wave arrival detection and picking with multiscale wavelet analysis for single-component recordings, *Bull. Seismol. Soc. Am., 93(5)*, 1904–1912, 2003.

16 Infering a Maximum *A Posteriori* Probability Model from Geodetic Data

Jianbao Sun

Introduction

Space geodetic techniques, particularly GPS and Interferometric Synthetic Aperture Radar (InSAR), have become vital tools for earthquake and crustal deformation studies, in recent years. Data measured using these techniques have been widely used for inversion of coseismic, postseismic and interseismic slip, as well as for inferring best-fit source parameters of geophysical phenomena. A number of optimization methods exist for modeling and interpretation of geodetic data (*e.g. Menke*, 2012; *Tarantola*, 2005). Each approach has pros and cons for solving the geodetic inversion problems, but we mostly rely on the different forms of least squares methods for both linear and nonlinear problems. This is vital for geodetic data interpretation because InSAR provides extremely high horizontal resolution, with a few to tens-of-meter pixel size for most of the satellites, such as the Envisat satellite from the European Space Agency (ESA) or the TerraSAR-X satellite from German Aerospace Center (DLR). The high resolution, with unprecedented deformation measurement precision, requires that InSAR data be inverted with efficient algorithms. This is a challenge for geophysical studies and emergency responses, because the problems are strongly nonlinear when geodetic data are linked with geophysical models.

A class of inversion approaches for geodetic data relies on probabilistic inversion methods, which describe the inversion problem as an *a posterior* probability density function (PDF) sampling process. The *a posterior* PDF is composed of a prior PDF of unknown parameters and a likelihood function connecting data with theoretical models. The prior PDF is updated using the likelihood function according to Bayes' theorem. The *a posterior* PDF is sampled with a Markov Chain Monte Carlo (MCMC) method. This is the Bayesian inversion method for geodetic inverse problems. *Fukuda and Johnson* (2008) developed the Fully Bayesian inversion method, which treats every unknown parameter as a nonlinear parameter and inverts in a MCMC process, without using the least squares inversion. This method is theoretically advantageous for solving the problem for all of the unknown parameters in a unified framework and one process. However, it also complicates the parameter search in a high-dimension nonlinear space with large amounts of observations, such as InSAR data. *Fukuda and Johnson* (2010) developed another *a posterior* PDF for geodetic inversion problems, which uses linear least squares inversion with a MCMC sampling process for nonlinear parameters, called Mixed linear-nonlinear Bayesian inversion method. This is a reasonable treatment to geodetic problems because they have both linear and nonlinear properties. The least squares solution for linear parameters greatly reduces the computation cost compared to the solution of treating all parameters as non-linear.

A Maximum *A Posteriori* Probability Model

The Bayesian methods are still far less efficient than the popular global optimization methods, such as simulated annealing, genetic, or neighborhood algorithms. However these methods are not optimized for uncertainty estimates. In addition, the two Bayesian inversion methods risk to be trapped in low-probability regions, or might never sample disconnected regions of the parameter space, leading to divergence of the inversion. This can occur because the structure of parameter space is unknown, and we cannot guarantee that a random walk is able to explore the global parameter space. It is quite possible that the collected models close to the mathematical maximum of the *a posterior* PDF are not geophysically reasonable.

Our solution to these problems is to use the fast global optimization algorithm—Adaptive Simulated Annealing (ASA) (*Ingber*, 1993)—to search the parameter space, while using constraints for both linear and nonlinear parameters to guarantee that physically reasonable models are collected (*Sun et al.*, 2013). This falls in the well known class of Maximum-*A-Posteriori* (MAP) methods. The 'mode' of the *a posterior* PDF will be searched through the global optimization inversion. The parameter uncertainties are not obtained as conveniently as in the Bayesian methods. However, by analyzing the models collected at the later stage of the inversion, or starting an independent Bayesian inversion after the MAP inversion, it would be easy to estimate the parameter uncertainties, because the efficiency of the MCMC method depends on how far the initial solution is from the 'mode' of the posterior PDF.

We use the *a posterior* PDF from *Fukuda and Johnson* (2010) as the optimization objective. By using this *a posterior* PDF, some of the important advantages of the Bayesian method are inherited, *e.g.,* objective smoothing of slip solutions, a unified solution for all of the parameters in one process (regularization factor, data weights, unknown fault geometry parameters and fault slips). This is in contrast to using a uniform slip assumption in a prior step. Currently, we mainly use the MAP method for coseismic slip inversions, including both highly nonlinear parameters and a large number of fault-slip parameters, with high-resolution geodetic observations, such as GPS and InSAR data. However, the method is not limited to coseismic slip inversions, and other geophysical problems with both linear and nonlinear properties can be addressed with this method in a more efficient manner if the nonlinear properties are weak. The MAP method we developed here gains high efficiency due to using the very fast global optimization method ASA. It normally takes only a few minutes to obtain a solution for one-segment slip models of a blind fault, even with a large number (> 1000) of data points. For multiple fault-segment models, the computation cost depends on the number of nonlinear parameters and the matrix size of the least squares inversion. However, the MAP inversion can quickly converge to the vicinity of the *a posterior* PDF mode in the initial stage, with the following iterations refining the solution step by step. This is particularly useful in rapid-response applications, where a first-order model is needed; *e.g.*, for stress transfer assessment after an earthquake.

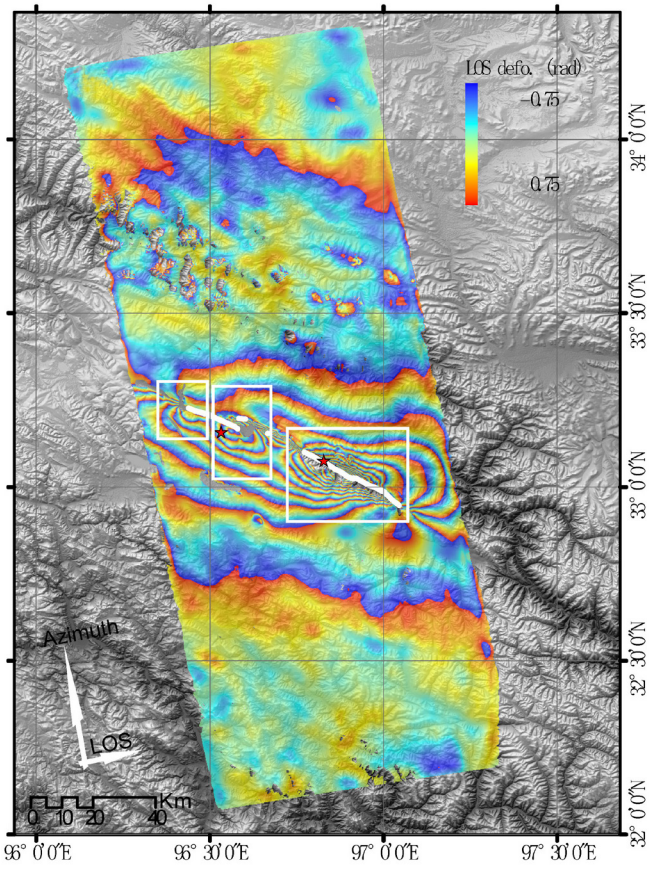

Figure 2.16.1: One of the L-band InSAR interferograms of the 2010 Yushu, China earthquake produced from ALOS PALSAR data. The white lines show the surface rupture from field investigations and the white rectangles highlight areas of high displacement gradients. The right star is the location of the maximum surface slip, and the left one is the epicenter from USGS solution. Note that the fringe between 33.5°N and 34.0°N, is likely due to atmospheric delay, rather than earthquake deformation.

Moreover, it is promising to use this method to construct a database of geophysical models from geodetic data in a unified form, so that the underlying deformation mechanisms of the lithosphere can be inferred.

A MAP Model Case of a Large earthquake

The slip model of the April 14, 2010 Mw 6.9 Yushu, China earthquake is a modestly difficulty case, composed of three segments with a sinistral strike-slip dominated mechanism. There are 3537 subsampled InSAR data points on three tracks used in the inversion (Figure 2.16.1). We failed to get the inversion to converge using Bayesian inversions of the three tracks of InSAR data; however, the inversion stably converged to the model shown in Figure 2.16.2 using the MAP method.

References

Fukuda J., and Johnson, K., A Fully Bayesian Inversion for Spatial Distribution of Fault Slip with Objective Smoothing, *Bulletin of The Seismological Society of America*, *98(3)*, 1128-1146, doi:10.1785/0120070194, 2008.

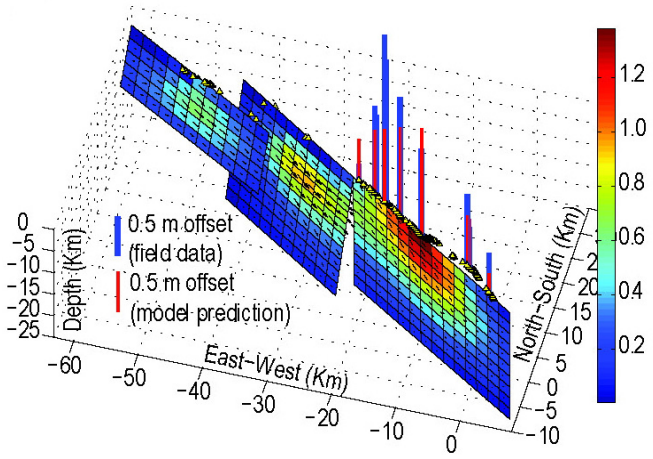

Figure 2.16.2: The MAP model of the 2010 Yushu, China earthquake. Also shown are the model offset predictions at the surface with field data for comparison.

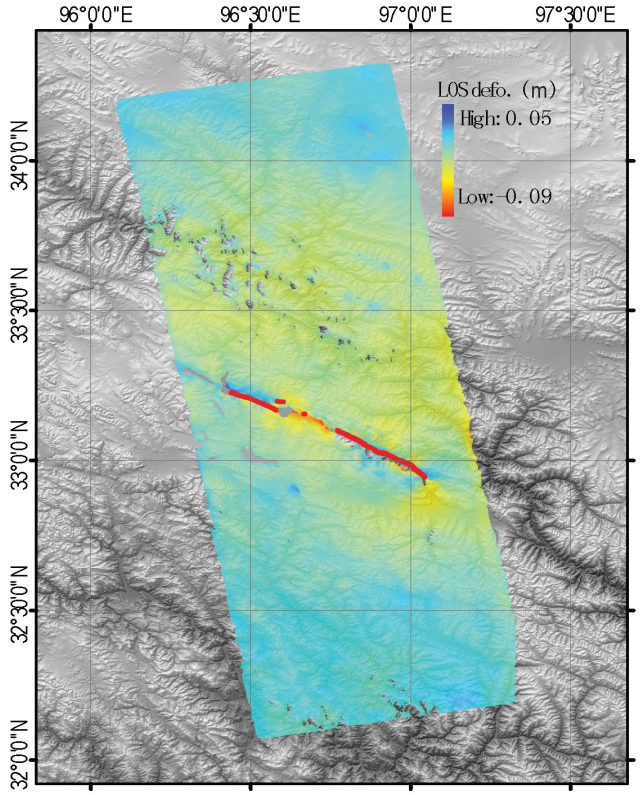

Figure 2.16.3: The residuals of the interferogram in Figure 2.16.1 after removal of the forward modeled InSAR deformation using the MAP model in Figure 2.16.2. Note that the unwrapped fringe between 33.5°N and 34.0°N still exists.

Fukuda J., and Johnson, K.M., Mixed linear–non-linear inversion of crustal deformation data: Bayesian inference of model, weighting and regularization parameters, *Geophysical Journal International*, *181(3)*, 1441-1458, doi:10.1111/j.1365-246X.2010.04564.x., 2010.

Sun J., Shen, Z.-K., Bürgmann, R., Wang, M., Chen, L., and Xu, X., A three-step Maximum-A-Posteriori probability method for InSAR data inversion of coseismic rupture with application to the April 14, 2010 Mw 6.9 Yushu, China earthquake, *J. Geophys. Res*, *in press*, doi:10.1002/jgrb.50244, 2013.

17 Exploring Landslide and Granular Mechanics from Geodetically Derived Surface Flow Kinematics

Brent Delbridge, Roland Bürgmann, Eric Fielding, Scott Hensley, Bill Schulz

Introduction

This project focuses on improving the understanding of the physical mechanisms controlling landslide motion by studying the landslide-wide kinematics of the Slumgullion landslide in southwestern Colorado using interferometric synthetic aperture radar (InSAR) and GPS. Factors which may control the landslide motion include pore-water pressure, inertia, the geometry of the landslide boundaries, and material properties such as strength, viscosity, hydraulic conductivity, diffusivity, and density (*Schulz et al.*, 2009b, *Schulz et al.*, 2009a). Our task is to examine the relative importance of each of these factors by understanding how they manifest themselves as observable modulations of the slide deformation under different external forcing such as rainfall, snowmelt and atmospheric pressure variations.

The deformation field derived from InSAR will provide the necessary observations to interpret and identify the spatial scale-dependent processes by providing the important length scale observations necessary to go beyond kinematic slide models and use this slide as a large granular shear experiment to push our current understanding of granular media.

By utilizing the temporal resolution of real-time GPS acquired during a temporary deployment from July 22nd through August 2nd with the landslide-wide coverage of the InSAR-derived deformation, we hope to elucidate the landslide response to environmental changes such as rainfall, snowmelt, and atmospheric pressure, and consequently, the mechanisms controlling the dynamics of the system.

The results of this study will also allow us to test the agreement and commensurability with Uninhabited Aerial Vehicle Synthetic Aperture Radar (UAVSAR) derived deformation with real-time GPS observations and traditional satellite-based SAR interferometry from the COSMOSkyMed system. We will not only help mitigate the hazards associated with large landslides, but also provide information on the limitations of current geodetic imaging techniques. This unique opportunity to compare several concurrent geodetic observations of the same deformation will provide constraints and recommendations for the design and implementation of future geodetic systems for the monitoring of earth surface processes.

The Slumgullion Natural Laboratory

The Slumgullion landslide provides an ideal setting in which to study landslide mechanics because of its rapid deformation rates of up to 2 cm/day and large spatial extent in which to examine the complex interaction of different kinematic elements within the slide (3.9 km long with an estimated volume of 20×10^6 m^3, *Parise and Guzzi*, 1992). The slide has also shown sensitivity to rainfall, snowmelt, and atmospheric pressure variations from passing storm fronts and the solid earth and ocean tides (*Schulz*, 2009). The clearly measurable response of the slide motion to environmental forcing makes Slumgullion a perfect natural laboratory.

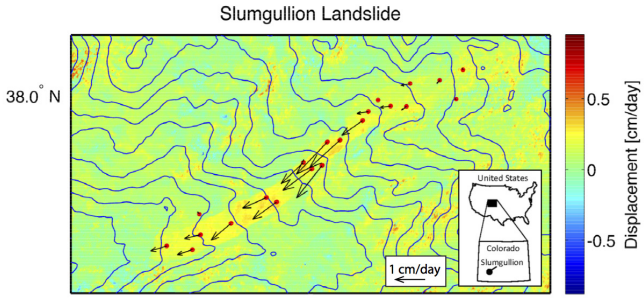

Figure 2.17.1: The colors above show the line-of-sight (LOS) displacement inferred from a pair of UAVSAR images collected one week apart on April 16th and 23rd 2012. The red circles and corresponding black vectors show GPS derived horizontal motion. The Slumgullion landslide is located in the San Juan Mountains of southwestern Colorado (inset) and has been moving for approximately the last 300 years (*Crandell and Varnes,* 1961) with total displacement on the order of hundreds of meters (*Coe et al.*, 2003).

Fleming et al. (1999) performed detailed mapping of the landslide and showed that the landslide has about a dozen kinematic units. These units are generally separated by narrow zones across which most differential displacement occurs. *Fleming et al.* (1999) measured average annual velocities of (0.5-2.0 cm/day) with lowest velocity at the landslide head (0.3 cm/day), low velocity at the toe (0.5 cm/day), and greatest velocity (2 cm/day) where the landslide is narrowest and steepest. They found that velocity varies seasonally, presumably due to changes in pore-water pressures. *Coe et al.* (2003) performed periodic surveying of surface monuments distributed across the landslide and hourly monitoring at two locations of landslide displacement, air and soil temperature, snow depth, rainfall, soil-water content, and groundwater pressures within an apparently perched aquifer. They found that the landslide moved fastest during spring and summer and slowest during winter. The time between rainfall and the landslide velocity response was less than several weeks.

Schulz and others (2009a,b) performed further sampling, field testing and monitoring at one location on the side of the landslide for three years. They found the landslide motion accelerated when pore-water pressure increased within the landslide body, but the pore-water decreased along the landslide margin. The decrease in pore pressure at the slide margins probably occurred in response to shear-induced soil dilation. Consequently, the decreased pore-water pressures increased effective stress and caused the landslide to decelerate. This hypothesis is supported by large-scale ring-shear tests on shear zone soils, precise leveling across part of the bounding shear zone, *in situ* hydrologic testing, and laboratory measurements of soil porosity (*Schulz et al.*, 2008).

Current Research

The NASA/JPL UAVSAR airborne repeat-pass SAR interferometry system imaged the Slumgullion landslide from four look directions on eight flights in 2011 and 2012. Combining the four look directions allows us to extract the full 3-D velocity field of the surface. COSMO-SkyMed(CSK) high-resolution Spotlight data was also acquired during time intervals overlapping with the UAVSAR one-week pairs, with intervals as short as one day. Interferograms made from pairs of CSK images acquired in 2010, 2011 and 2012 reveal the slide deformation on a longer timescale by allowing us to measure motion on a scale of meters and see the average rates over year-long intervals using pixel offset tracking of the high-resolution SAR amplitude images. The spatially complex deformation field derived from InSAR will provide the necessary observations to interpret and identify the spatial scale-dependent processes present by providing the important length scale observations necessary to go beyond kinematic slide models.

Additionally, TerraSAR-X repeat-pass interferometry data was acquired in 2011–2012 and TanDEM-X bistatic (single-pass interferometry) data was acquired in 2011. The TanDEM-X bistatic data will enable construction of a high-resolution InSAR digital elevation model. These observations were taken to complement and overcome the spatial limitations of ongoing yearly GPS observations from 18 monitoring points and *in situ* observations of pore-pressure and atmospheric parameters acquired by collaborator Bill Schulz from the USGS. The high resolution topography derived from our Tandem-X BiStatic data will be used to correlate the slide topology with its complex spatial deformation, which will allow me to extract the roles played by composition and geometry. We continued to build upon this work by beginning an independent field investigation consisting of the deployment of seven continuous GPS stations along the length of the slide from July 22nd to August 2nd, 2012. This time period was concurrent with the acquisition of several SAR images including a pair of four-pass UAVSAR flights July 24th–August 1st 2012. COSMO-SkyMed high-resolution Spotlight data was also acquired over the landslide during time intervals overlapping with the UAVSAR one-week pairs and GPS deployment, with time intervals as short as one day. (five CSK acquisitions total, three descending track and two ascending track). Additionally, the topographic data will also act as a unique and independent dataset allowing for quantitative geomorphometric analysis.

We believe that the synthesis of these observations will result in a more robust estimate of the total slide displacement, and yield a robust estimate of the systematic and random errors present in these observations. The temporal resolution of the real-time GPS will compliment the landslide-wide spatial coverage of the InSAR-derived deformation to provide full coverage of the surface displacement. The spatiotemporal overlap of the various geodetic datasets in this study provide a unique opportunity to quantify information on the limitations of current geodetic imaging techniques, and their application to studying earth surface processes.

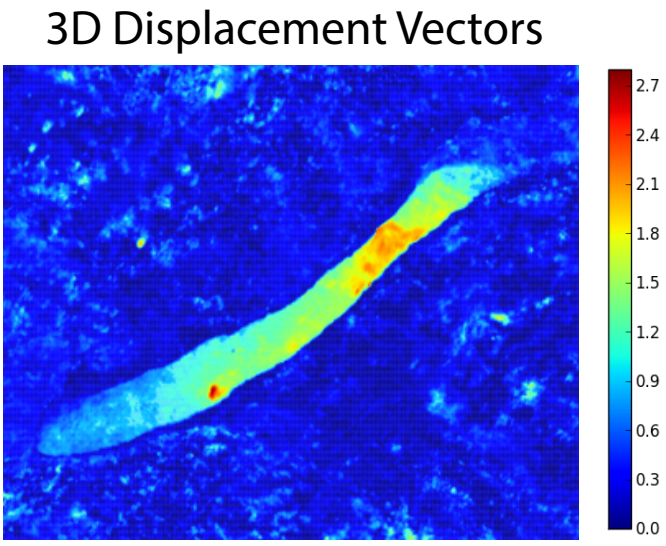

Figure 2.17.2: The image above shows the magnitude of the 3D displacement vectors which were estimated from four UAVSAR one-week interferogram pairs spanning April 16th–April 23rd 2012 (one of these images used is shown in Figure 2.17.1). The slide velocity increases with warmer colors. The narrow, rapid portion of the slide reaches the 2 cm/day previously measured by *Coe et al.*, 2003 and others. Note that the largest velocity magnitudes of 2.7 cm/day are restricted to a small isolated region near the toe of the slide, and appear to be a smaller slide piggybacking on the larger flow. The coincident acquisition of these images along four independent flight paths allowed us to extract the true physical displacement of the image ground surface. This procedure overcomes the ambiguity in determining the slide motion present in a single interferogram, which only yields deformation information in the 'look direction'.

Acknowledgements

This has been supported by an NSF Graduate Research Fellowship and is a collaboration of The University of California Berkeley with the USGS in Colorado, and Jet Propulsion Laboratory in Pasadena, California.

References

Coe, J. A., Ellis, W. L., Godt, J. W., Savage, W. Z., Savage, J. E., Michael, J. A., & Debray, S., Seasonal movement of the Slumgullion landslide determined from Global Positioning System surveys and field instrumentation, July 1998–March 2002, *Engineering Geology*, 68(1), 67-101, 2003.

Fleming, R. W., Baum, R. L., & Giardino, M., Map and description of the active part of the Slumgullion landslide, Hinsdale County, Colorado, US Department of the Interior, US Geological Survey, 1999.

Schulz, W. H., Kean, J. W., & Wang, G., Landslide movement in southwest Colorado triggered by atmospheric tides, *Nature Geoscience*, 2(12), 863-866, 2009.

Schulz, W. H., McKenna, J. P., Kibler, J. D., & Biavati, G., Relations between hydrology and velocity of a continuously moving landslide evidence of pore-pressure feedback regulating landslide motion?, *Landslides*, 6(3), 181-190, 2009.

18 Geodetic Tracking and Characterization of Precipitation Triggered Slow Moving Landslide Displacements in the Eastern San Francisco Bay Hills, California, USA

Julien Cohen-Waeber, Roland Bürgmann, Nicholas Sitar, Alessandro Ferretti, Chiara Giannico, Marco Bianchi

Introduction

Technologies such as continuous Global Positioning Systems (GPS) and Interferometric Synthetic Aperture Radar (InSAR) are now capable of measuring active surface displacement with as much as sub-centimeter precision and accuracy. While GPS has become such a fundamental tool that tracking discrete points in real time is common and reliable, its finite spatial extent is a shortcoming. Alternatively, the introduction of InSAR has allowed widespread surface deformation tracking, though it is still far from being real time. Evidently, these technologies are complementary and lend themselves to numerous geological engineering applications including the characterization and tracking of subsidence, seismically induced crustal deformation, or in our case, landslides. Thus, the objective of this work is to characterize, by a careful observational program, active slope deformation resulting from various static and dynamic conditions across the Lawrence Berkeley National Laboratory (LBNL) site and the San Francisco East Bay hills (Berkeley Hills). Through the instrumentation of individual landslides with a comprehensive network of continuous GPS stations, and regional monitoring of slope surface deformation by InSAR time series analysis, this study focuses on the effects and characterization of precipitation triggered slow moving landslide displacements.

InSAR Time Series Analyses

A review of three independent InSAR time series analyses of the Berkeley Hills, from separate satellite acquisitions over different time intervals from 1992-2011, shows remarkable consistency (*Hilley et al. 2004, Quigley et al.* 2010*, Giannico et al.* 2011). In each case, a clear precipitation dependent behavior of landslide displacement has been observed, with similar mean downslope velocities of approximately 30 mm/year and periods of higher velocities during each wet season. Furthermore, these studies suggest that internal deformation of each slide mass is noticeable when divided into groups of coherently moving masses (*Quigley et al.* 2010*, Cohen-Waeber et al.* 2013). In fact, improved InSAR methods which allow higher spatial resolution have allowed preliminary conclusions on the mechanics of displacement within these landslides as different sections of the deformable slide mass mobilize separately.

The InSAR time series analysis of permanent scatterers performed by *Hilley et al.* (2004) first showed the use of InSAR for seasonal landslide displacement tracking using European Space Agency satellites ERS-1 and ERS-2 data acquisitions from 1992 to 2001. The study observed that periods of landslide acceleration were closely related to seasonal precipitation, though non-linear in that precipitation related displacement did not occur immediately, with lag times of up to 3 months, and did not predictably increase with larger events.

Similarly, *Quigley et al.* (2010) examined seasonal precipitation-related displacement, supplementing the same ERS data set with the Canadian Space Agency's RADARSAT-1 acquisitions from 2001 to 2006. Landslide displacement was shown not only to be of the same magnitude as for the ERS data, but was also clearly seasonal and sensitive to variations in rainfall patterns as well. Detrended and stacked (by month) observations plotted against average monthly precipitation exhibited a clear 1 to 3 month displacement response lag time and a positive correlation to the intensity of precipitation.

An important limitation of the Permanent Scatterer InSAR method used in these examples is the presence of stable coherent targets. To improve spatial resolution, a new algorithm (SqueeSAR™) developed by Tele-Rilevamento Europa (TRE) utilizes both the Permanent and Distributed Scatterer methods (*Ferreti et al.* 2011). Thus, a third InSAR time series analysis was performed over the Berkeley Hills by *Giannico et al.* (2011) applying the SqueeSAR™ method to the German Space Agency's TerraSAR-X data acquisitions from 2009-2011. Once again, landslide related displacements were clearly identifiable with similar velocities and with periods of precipitation-related acceleration, though with better spatial coverage (Figure 2.18.1, top).

The higher spatial resolution afforded by the SqueeSAR™ method allows closer observation of the landslide mechanisms as expressed at the ground surface, much like in *Quigley et al.* (2010). In this case, the downslope displacements of different areas within the Berkeley Hills landslides reveal that they are in fact moving as bodies of smaller coherent masses, much like a flow slide, with what could be called an "accordion effect" (*Cohen-Waeber et al.* 2013). Differencing the average downslope displacements of the top, middle and bottom of the landslides reveals a pattern of apparent landslide extension, followed by a landslide shortening as the precipitation progresses. During wet seasons, the lower portions of the landslides accelerate earlier than the upper portions while toward the end of wet seasons and into dry periods, the lower portions of the landslides slow and the upper portions catch up (Figure 2.18.1, Bottom).

Continuous GPS Tracking

With the installation of seven continuous GPS stations on several LBNL and Berkeley Hills landslides, ground surface displacements are being tracked at a data collection rate of 1 Hz, since January 2012. While historical ground surface displacements related to these landslides have yet to be fully characterized and quantified, a clear signal from daily solutions at several of these stations is already apparent. Through two mildly wet

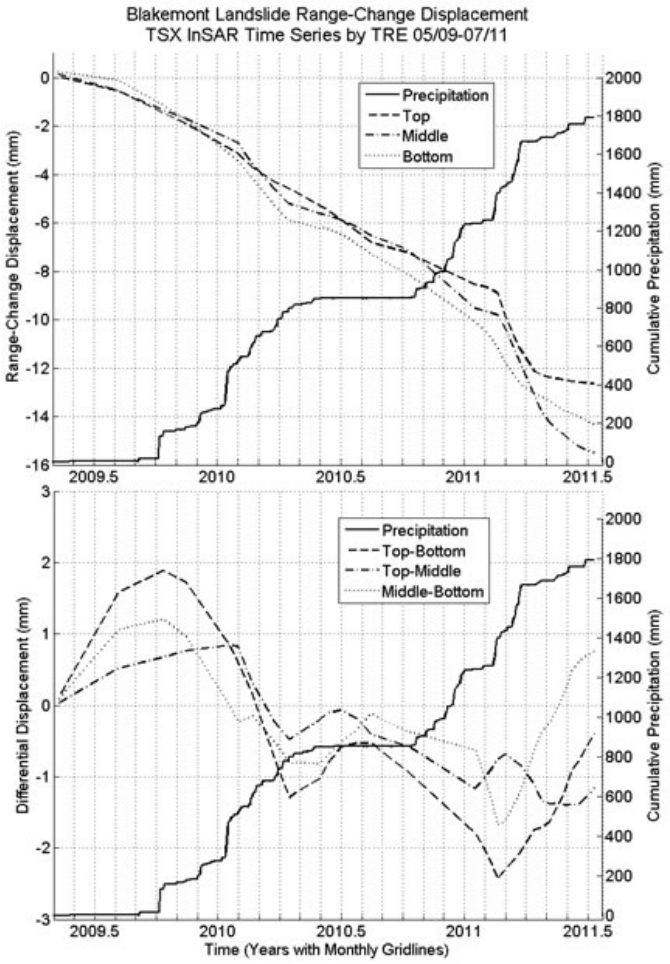

Figure 2.18.1: Average downslope range-change displacement (top) and differential of average downslope displacements from TRE SqueeSAR™ analysis of TerraSAR-X data acquisitions (2009-2011, bottom) in areas of Blakemont Landslide, versus cumulative precipitation (right axes).

seasons, GPS measurements have confirmed InSAR observations with well-defined precipitation triggered slope movement at similar average velocities and the same "accordion effect".

Preliminary Conclusions

Overall, InSAR has demonstrated its capability to record and characterize landslide motions that otherwise would not have been observed with such level of detail. Records of landslide related surface displacement from several independent studies have similar precipitation triggered down-slope velocities, and comparable internal mechanisms exhibiting progressive accordion-like downslope failure typical to slow moving flow slides. While both methods of observation have not yet been compared on one landslide over the same period, they are complimentary and these observations have been verified by continuous GPS data. Improved InSAR spatial coverage and observations over longer periods will provide important insight on the triggering mechanisms and internal landslide behaviors described. Notably, further work is planned to explore the possibility of seismically induced landslide motions. Despite recent moderate earthquakes in the region, these have not yet been documented, (*Hilley et al.* 2004, *Cohen-Waeber et al.* 2013) primarily due to the lack of temporal resolution with InSAR.

Acknowledgements

We gratefully acknowledge our financial support from the Lawrence Berkeley National Laboratory, Earth Science Division Director's fund.

References

Cohen-Waeber J. et al., GPS Instrumentation and Remote Sensing Study of Slow Moving Landslides in the E. San Francisco Bay Hills, CA., Proceedings of the 18th Int. Conf. on Soil Mech. and Geotech. Eng., Paris, France, 2013.

Ferretti A. et al., A New Algorithm for Processing Interferometric Data-Stacks: SqueeSAR, *IEEE Geoscience and Remote Sensing* 49(9), 3460-3470, 2011.

Giannico C. and Ferretti A, SqueeSAR™ Analysis Area: Berkeley, *Processing Report*, Tele-Rilevamento Europa, Milano, IT, 2011.

Hilley G.E. et al., Dynamics of Slow Moving Landslides From Permanent Scatterer Analysis, *Science* 304, 1952-1955, 2004.

Quigley K. C. et al., Seasonal Acceleration and Structure of Slow Moving Landslides in the Berkeley Hills, Proc. of the 3rd Conf. on Earthquake Hazards in the E. San Francisco Bay Area; edited by Keith Knudsen, *CA Geol. Surv. Special Report 219*, 169-178, 2010.

19 Repeating Earthquake Slip Evolution Along 200 km of the Central San Andreas Fault

Robert M. Nadeau, Ryan C. Turner, and Roland Burgmann

Introduction

An historic catalog of micro-earthquakes and digital seismograms from the Northern California Seismic System (NCSS) extending back through 1984 enable a spatially and temporally extensive view of active faulting processes at depth using repeating earthquakes along a ~ 200km long section of the central San Andreas Fault (SAF) zone. We analyzed seismic data along this section to identify new repeating earthquake (REQ) sites and to update known REQ sites (*Nadeau and McEvilly*, 2004; T*urner et al.*, 2013) through April of 2011. This information was then used to infer the evolution of aseismic fault slip at seismogenic depth along the fault section in order to investigate the general underlying architecture and mechanics of the faulting process at the location and to assess the relationship of the REQ behavior with respect to the occurrence of larger (> M4) earthquakes in the region. This provides insights into the evolution and role of transient aseismic fault slip in earthquake occurrence that should ultimately lead to improved models of the earthquake cycle and aid in the development of more accurate earthquake forecasts.

Results

We searched for and updated REQs in the study zone using a waveform cross-correlation/cross-coherencey method (*Nadeau and McEvily*, 2004). The resulting REQ catalog consisted of 870 REQ sites comprised of 6011 repeated events (Figure 2.19.1). The REQ search region also included several 10s of km both northwest and southeast of the 200km section, but yielded little evidence of REQ activity in these presumably locked fault regions.

Deep fault creep inferred from the REQs (*Nadeau and McEvilly*, 2004) occurring on the SAF-proper show a clear decrease in rates (below the Pacific-North American relative plate motion rate of 3.3 cm/yr) to the northwest of the juncture of the San Andreas and Calaveras faults at about 90 km NW (Figure 2.19.1). Deep creep occurring off the SAF (i.e., to the northeast) is also observed along the sargent fault (~140 to 160 km NW) (*Turner et al.*, 2013) and on the Paicenes-San Benito faults (~80 to 87 km NW). With the exception of the region from ~ 65 to 80 km NW, more complex spatial and temporal deep-creep behavior is also observed in regions of moderate to large earthquake activity (>M4.0).

In the Parkfield area, for example, a significant increase in the rate of creeping is observed following the M6.0 earthquake. Before the M6.0 event, cumulative creep was well behind that expected for freely creeping fault keeping pace with the relative plate motion rate of 3.3 cm/yr. However, by the end of the study period in April of 2011, the accelerated accumulation of creep resulting from the post-seismic creep released from the M6.0 appears to have resulted in a cumulative creep over the study period that is consistent with the expected long-term accumulation of creep from tectonic plate motion, at least between +5 km and -15 km northwest.

Though a post-seismic increase in creep accumulation following the M6.0 is observed southeast of -15 km, it continues to lag behind the plate rate, indicating an increase in slip deficit of ~ 50-60 cm since the end of 1984 at the southeastward end of the study segment. This and the absence of identifiable REQs farther to the southeast is consistent with classification of the Cholame segment of the SAF as a type-A locked fault segment capable of rupturing in an ~ M7.0 or larger earthquake (UCERF 2, 2007).

Two prominent along-strike dips in the cumulative deep creep contours are also observed centered at about 73 and 85 km NW. The 85 km dip appears to correspond well with the location of the off-SAF sequences, suggesting relative plate motion that is to be accommodated by deformation on at least two sub-parallel fault zones. The dip at 73 km has no corresponding off-fault REQ activity, but the spatial distribution of low-rate REQs appears to outline a low-repeat-rate seismicity hole, possibly indicating a zone of slip-deficit accumulation above ~ 6km that has dimensions of about 15 km along-strike and 5 km in depth. The slip deficit in this area is on the order of 40 cm, since 1984 and if an earthquake were to rupture over this area and release this accumulated deficit it could generate an M5 or larger earthquake.

Acknowledgements

Supported by the U.S. Geological Survey through award G10AC00093 and by the National Science Foundation through award EAR-0951430. Waveform data were provided by the Northern California Seismic System, USGS, Menlo Park by way of the Northern California Earthquake Data Center at the Berkeley Seismological Laboratory (BSL).

References

Nadeau, R. M. and T. V. McEvilly, Periodic Pulsing of Characteristic Microearthquakes on the San Andreas Fault, *Science*, 303, 220-222, 2004.

Turner, R.C., R.M. Nadeau and R. Burgmann, Aseismic Slip and Fault Interaction from Repeating Earthquakes in the Loma Prieta Aftershock Zone, *Geophys. Res. Lett.*, 40, 1079–1083, doi:10.1002/grl.50212, 2013.

Waldhauser, F., and D. P. Schaff (2008), Large-scale relocation of two decades of Northern California seismicity using cross-correlation and double-difference methods, *J. Geophys. Res.*, 113, B08311, doi:10.1029/2007JB005479.

Waldhauser, F. (2009), Near-real-time double-difference event location using long-term seismic archives, with application to Northern California, *Bull. Seism. Soc. Am.*, 99, 2736-2848, doi:10.1785/0120080294.

Working Group on California Earthquake Probabilities (WGCEP)

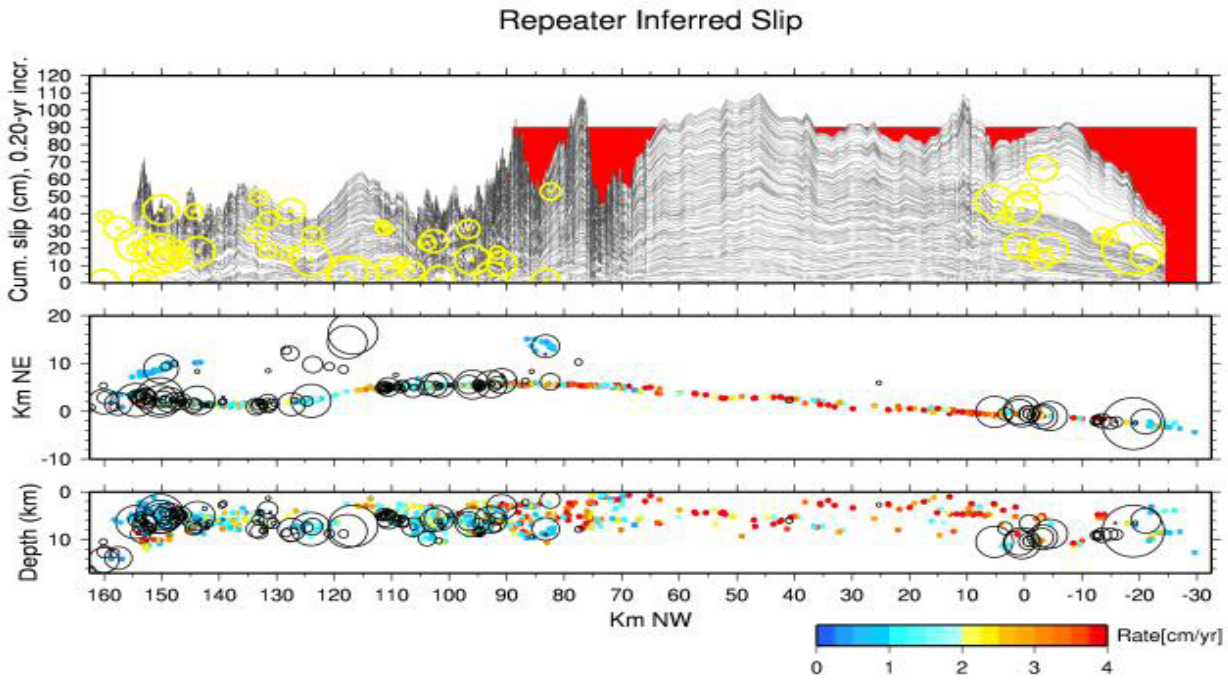

Figure 2.19.**1:** REQ inferred cumulative deep-creep through time (top) and Double-difference relocations (DDRT, *Waldhauser and Schaff*, 2008; *Waldhauser*, 2009) of 870 REQ sites along the ~ 200 km long study region (middle, bottom). Cities of Parkfield and San Juan Bautista are located at -9 and +135 km, respectively. The REQ events range in magnitude from ~ M1.4 to 3.5. Top: Contours of cumulative deep-creep from REQs from 1984 through April, 2011 at 0.2 yr intervals with along-strike smoothing of 15 REQ sequences. Yellow symbols are >M4 events occurring during this period and centered on the nearest 0.2yr contour. Red region is expected cumulative creep since 1984 assuming a tectonic rate of 3.3 cm/yr. Middle: Along-fault map view of SAF REQs color-coded to their average inferred slip rates over the entire 1984 - April 2011 study period. M4+ seismicity is shown as black circles. Bottom: Along-fault depth section of the same sequences. Off-SAF repeaters on the sargent fault (~140 to 160 km NW) and on the Paicenes-San Benito faults (~80 to 87 km NW) were not used in the slip contour calculations.

(2007), The Uniform California Earthquake Rupture Forecast, Version
2 (UCERF 2), *U.S. Geol. Surv. Open File Rep.*, 2007-1473, 1–104.

20 Variability of Fault Slip Behaviors along the San Andreas Fault in the San Juan Bautista Region, Inferred from Characteristically Repeating Earthquake

Taka'aki Taira, Roland Bürgmann, Robert M. Nadeau, Douglas S. Dreger

Introduction

An improved understanding of time history of fault slip at depth is an essential step toward understanding the underlying mechanics of the faulting process. We investigate spatially- and temporally-varying fault slip along the northernmost creeping section of the San Andreas fault near San Juan Bautista (SJB), California, by systematically examining spatiotemporal behaviors of characteristically repeating earthquakes (CRE).

Characteristically Repeating Earthquake Catalog

We have constructed the CRE catalog through a waveform cross-correlation analysis. We analyzed about 12,000 local events that occurred within a 15 km radius of the 1998 M_w 5.1 SJB earthquake. We evaluate the waveform similarity for a pair of seismograms in the vertical component with an 8-24 Hz bandpass filter based on the waveform cross-correlation coefficient and the phase coherency. To minimize the false detection of repeating earthquakes, we identify a pair of earthquakes as CREs if both the cross-correlation coefficient and the coherency are greater than 0.95 obtained from at least two stations. Our cross-correlation and coherency thresholds are comparable to those used in previous studies (e.g., *Zhao and Peng*, 2009). Our analysis identifies about 600 sequences with magnitudes ranging from -0.1 to 3.5 that are distributed in a depth range of 3 km to 10 km (Figure 2.20.1).

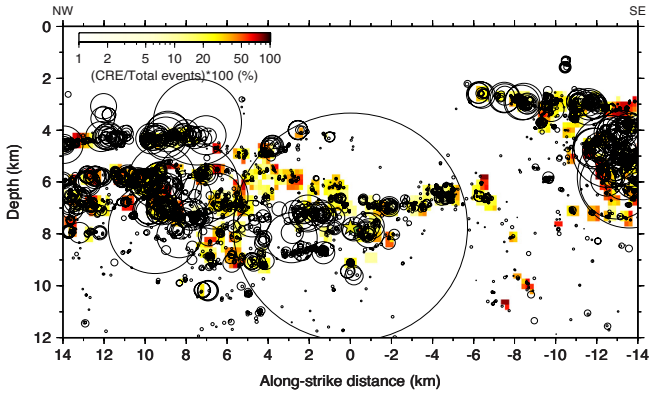

Figure 2.20.1: Spatial distribution of CREs near the 1998 M_w 5.1 SJB earthquake. Color scale indicates the CRE proportion of total seismicity. Circles are local earthquakes (1984-2012) analyzed to identify CREs, and their sizes are proportional to the rupture size. The yellow star is the 1998 SJB M_w 5.1 earthquake.

Following *Nadeau and Johnson* (1998) and *Chen et al.* (2007), we first explore a relation between the recurrence interval (*Tr*) and seismic moment (M_0) for the CREs identified in the SJB region. As the *Tr* of CREs were significantly perturbed following the 1998 M_w 5.1 SJB earthquake, we estimated the median *Tr* and M_0 in individual sequences from the CRE activity in 1990-1997. As shown in Figure 2, the *Tr*-M_0 relation from our study is in good agreement with those from *Nadeau and Johnson* (1998) and *Chen et al.* (2007). This would indicate that the SJB CRE can be used to infer temporal evolutions of the fault slip (*d*) near the CRE rupture area, with the empirical relation between *d*-M_0 introduced in *Nadeau and Johnson* (1998):

$$\log(d) = -2.36 + 0.17\log(M_0) \qquad (1.1)$$

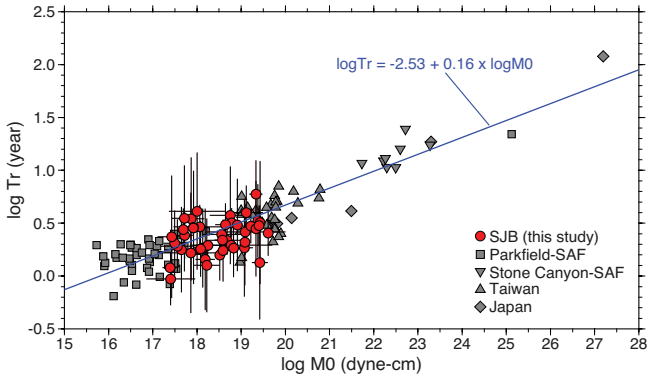

Figure 2.20.2: Recurrence interval (*Tr*) as a function of seismic moment (M_0) from *Chen et al.* (2007) and this study. Red circles are the SJB CRE sequences.

Temporal behaviors of fault slip are determined from CREs with equation (20.1) on the characteristic fault path where CREs occurred. We discretize a 28 km long, 12 km deep plane with 1 km x 1 km segments in the strike and dip directions, respectively. In each segment, we used CRE sequences that occurred within a 3 km radius from the center of the segment, and computed average fault slips when at least 3 sequences are available (Figure 2.20.3).

Spatial Variation in Interseismic Slip Rate

We evaluated the spatial distribution of the interseismic slip rate from CREs that occurred before the 1998 M_w 5.1 SJB earthquake at individual segments. Our analysis identifies a low-creep (0.1-0.2 cm/year) or locked asperity near the 1998 M_w 5.1 SJB earthquake (Figure 2.20.4). The geodetic slip rate in this area is about 2.3 cm/year (e.g., *Johanson and Bürgmann*, 2005). This suggests a considerable slip deficit was accumulated in the low-creep rate zone.

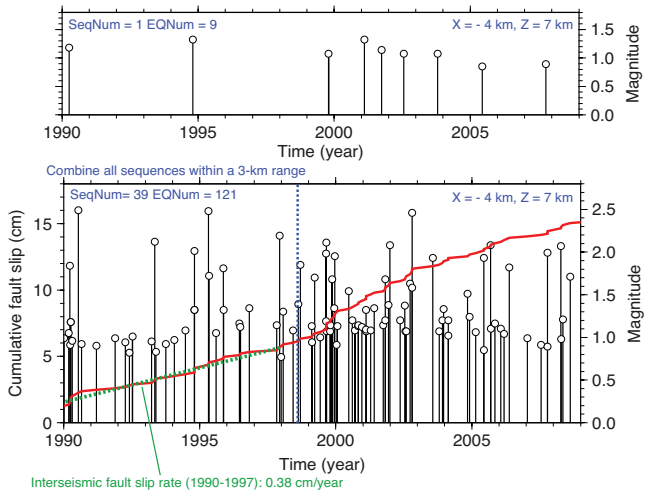

Figure 2.20.3: Fault slip estimate from CRE activity. Top panel shows the time history of a single sequence at the X=-4 and Z=7 grid point. The bottom panel shows the CRE activities from all sequences that occurred within a 3 km radius from this grid point. Red line is the time history of the average fault slip with equation (20.1.), and dashed blue line is the origin time of the 1998 SJB M_w 5.1 earthquake. Also shown is the interseismic slip rate estimate (dashed green line) with the CRE activity in 1990–1997.

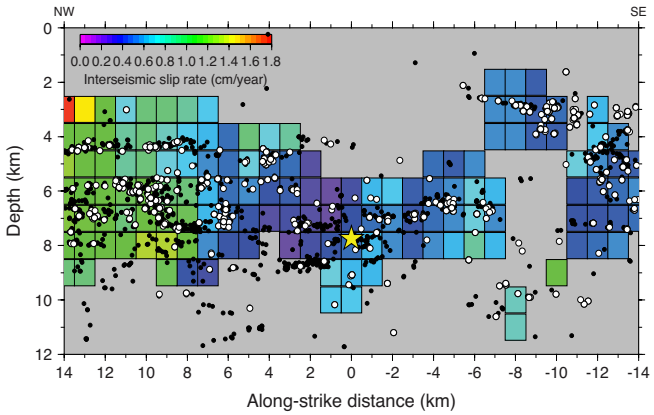

Figure 2.20.4: Spatial variation in interseismic slip rate (1990–1997) inferred from the characteristically repeating earthquakes. White and black circles indicate repeating and non-repeating earthquakes, respectively. The yellow star is the 1998 SJB Mw 5.1 earthquake.

Spatiotemporal Evolution of Postseismic Slip following the 1998 SJB M_w 5.1 Earthquake

In the postseismic period following the 1998 M_w 5.1 mainshock, the CRE activity was significantly increased in a zone at a depth of 5-10 km about 2-7 km northwest of the 1998 SJB mainshock (Figure 2.20.5), which indicates a triggering of substantial aseismic slip induced by the 1998 SJB mainshock. The largest accumulated postseismic slip is about 6 cm at this zone in the first 1000-day postseismic period. It appears that a considerable aseismic slip release occurred in the low-creep rate zone shown in Figure 2.20.4.

The spatial migration of the postseismic slip was inferred from CREs activities (Figure 2.20.6). Initial postseismic migration within the first 100 days was dominantly along the

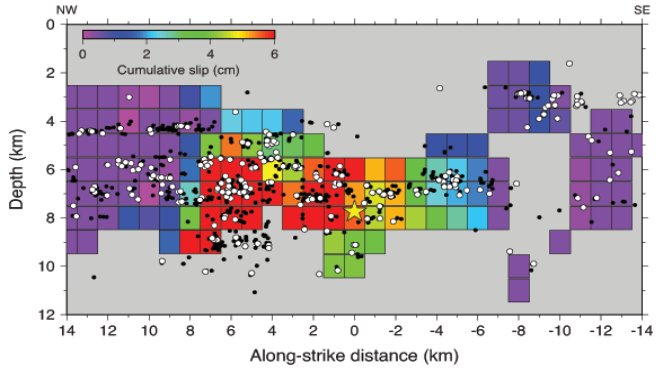

Figure 2.20.5: Spatial variation in posts sic slip in the first-1000 day postseismic period.

strike of the San Andreas fault, toward the northwest fault segment. After this postseismic period, another migration of postseismic slip was initiated, which was propagated into the southeast fault segment from the hypocenter of the 1998 M_w 5.1 SJB earthquake.

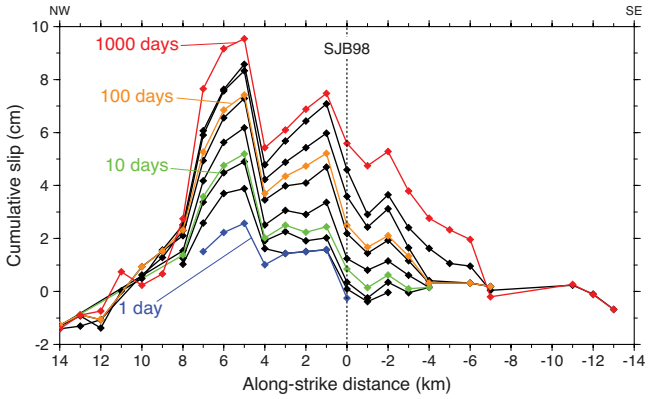

Figure 2.20.6: Cumulative postseismic slip inferred from CRE sequences.

Acknowledgements

We thank K.H. Chen for providing us with the CRE data, and the Northern California Earthquake Data Center for data collection and distribution for the seismic data in the northern California. This work is supported by the National Science Foundation grant EAR-0951430.

References

Chen, K.H., R.M., Nadeau, and R.J. Rau, Towards a universal rule on the recurrence interval scaling of repeating earthquakes?, *Geophys. Res. Lett., 34*, L16308, 2007.

Johanson, I. A., and R. Bürgmann, Creep and quakes on the northern transition zone of the San Andreas fault from GPS and InSAR data, *Geophys. Res. Lett., 32*, L14306., 2005.

Nadeau, R.M., and L.R. Johnson, Seismological studies at Parkfield VI: Moment release rates and estimates of source parameters for small repeating earthquakes, *Bull. Seismol. Soc. Am., 88*, 790–814, 1998.

Zhao, P., and Z. Peng, Depth extent of damage zones around the central Calaveras fault from waveform analysis of repeating earthquakes, *Geophys. J. Int., 179*, 1817-1930, 10.1111/j.1365-246X.2009.04385.x, 2009.

21 Seismic Quiescence Following Large Magnitude Earthquakes

Christopher Johnson and Roland Bürgmann

Introduction

Stress perturbations produced by large-magnitude earthquakes impact seismicity at regional and global distances by altering the stress on a fault plane and advancing or delaying earthquake nucleation. Regional changes in seismicity are observed in aftershock locations with areas of increased or decreased activity correlating to areas of positive or negative Coulomb stress changes, respectively (*Stein*, 1999). At distances beyond two fault lengths, *i.e.* the region experiencing significant static Coulomb stress change, seismic waves from large magnitude earthquakes have been shown to trigger small earthquakes (*Gomberg et al.*, 2001). This dynamic transfer of stress from seismic waves is also observed to trigger microseismicity and tremor in regions of geothermal activity as well as non-volcanic tremor in deep fault zones immediately during the passage of the waves and in the hours to days following (*Brodsky*, 2006; *Peng et al.*, 2010). Less frequently, immediate triggering of small earthquakes ranging from $3 > M < 5$ are detected during the surface wave train (*Husker and Brodsky*, 2004; *Tape et al.*, 2013). Above M>5, dynamic triggering is not observed at distances beyond the 2-3 fault lengths of a large-magnitude event (*Parsons and Velasco*, 2011). An exception to this finding is the M_W 8.6 2012 east Indian Ocean event that resulted in above-average global seismicity for events > M5.5 in the six days following the mainshock and is an example of delayed dynamic triggering which suggests that the stress perturbations experience during the teleseismic surface waves were large enough to advanced the earthquake cycle of multiple >M5 events (*Pollitz et al.*, 2012). As a result, questions remain regarding the dynamic triggering of large earthquakes at global distances and the influence of earthquake nucleation times following dynamic stress perturbations on active faults.

Subsequent to the global increase of seismicity as a result of the 2012 east Indian Ocean event is a 95 day period of quiescence for M≥6.5 events (*Pollitz et al.*, *Submitted*). The observable rate decrease following the 2012 Indian Ocean event prompted this study to examine if a magnitude threshold exists for seismic quiescence following a period of dynamically triggered earthquakes. Here we investigate the idea of global "dynamic shadowing" in order to determine if a spatial and temporal relationship to large magnitude events exists for periods of reduced global seismicity. This study builds on the previous work by *Parsons and Velasco* (2011) who concluded that an increase in M>5 seismicity is confined to the region within 2-3 fault lengths of the rupture and activity returned to background rates within 36 hours following a M>7 event. Using a similar methodology we explore the suppression of global activity with respect to background earthquake activity following large magnitude events. The goal of this study is to determine if a dynamic shadow results in a reduction of seismicity at a distinguishable level below the background seismicity over various temporal and spatial ranges.

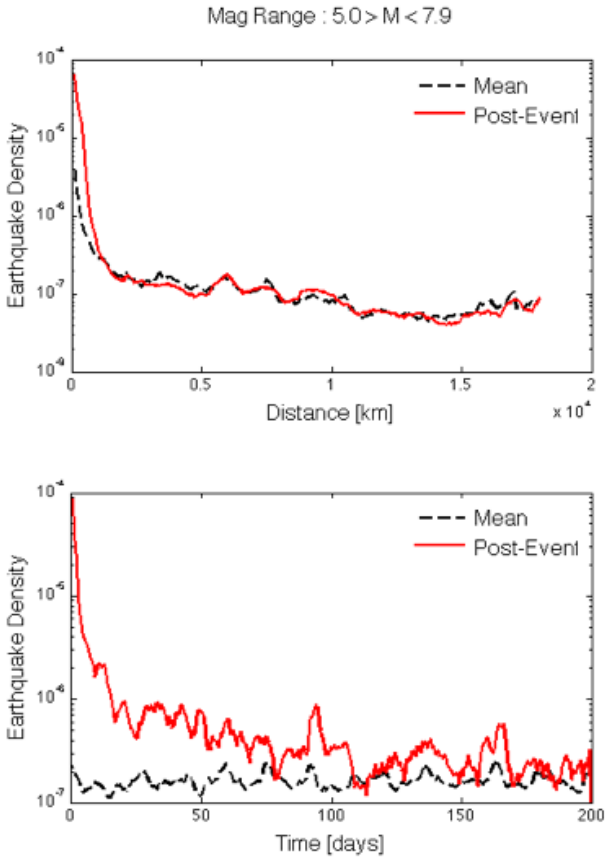

Figure 2.21.1: All events from 1977–2013 are considered between $5 > M < 7.9$ for the analysis. The top panel indicates a return to mean rates at a distance of ~1000 km. The bottom panel indicates increased activity for >100 days following a M≥7.9 event. Significant activity below the mean rate is not observed.

Methods

Establishing a change in earthquake rates requires a robust background rate for subsequent comparisons. Utilizing 35 years of earthquake catalog data obtained from the Advanced National Seismic System (ANSS), we analyze seismic rate changes following large magnitude earthquakes. Similar to *Parsons and Velasco* (2011) we compile earthquake catalogs within select magnitude ranges, one containing the range of magnitudes that possibly experience a rate change and the second catalog containing all remaining larger events. For each magnitude range considered, a spatial and temporal stacking of the events is used to calculate an earthquake density. The background rate is determined by randomly combining the event times using different locations within the compiled catalog of smaller events in order to scatter the foreshock and aftershock activity. By varying the magnitude range and time intervals around the large earthquakes, we will establish if a relationship exists between suppressed seismicity and very large magnitude events.

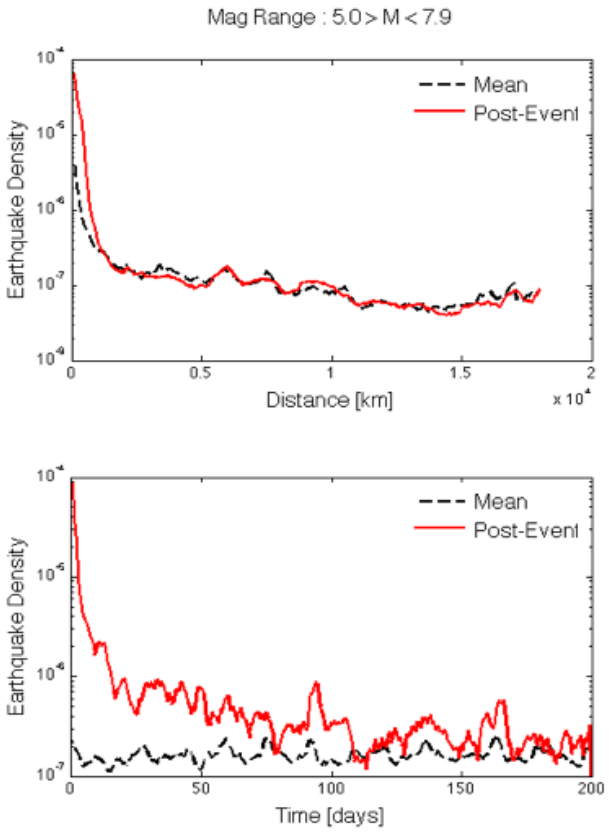

Figure 2.21.2: All events from 1977–2013 are considered between 6.0 > M < 7.9. Similar to the lower magnitude range, no increased activity is detected beyond ~1000 km. The bottom panel indicates a return to background rates within 25 days. Brief periods of activity below the mean are observed but the significance is not supported when considering the third catalog.

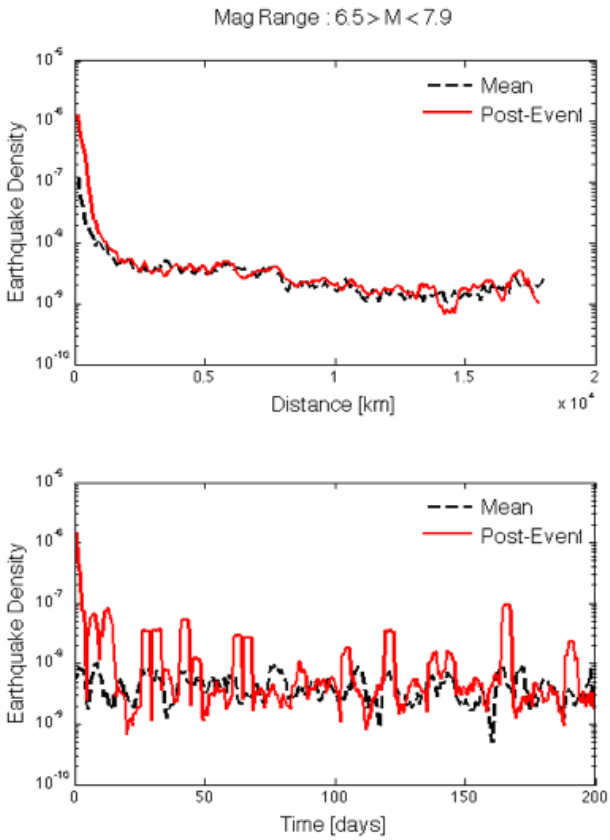

Figure 2.21.3: No significant suppression of activity is observed for events 6.5 > M < 7.9. Activity returns to mean rates within 1000 km and three days without a period of reduced activity.

Initial Results

Catalog data from 1977–2012 includes 36 $M \geq 7.9$ events and three catalogs are compiled containing all other events within 5.0 > M < 7.9, 6.0 > M < 7.9, and 6.5 > M < 7.9. Using a time window of 200 days and distances extending to 18,000 km, an earthquake density is computed by stacking all events relative to the large events in 12 hr bins at 100 km interval. T he mean density is calculated using the preceding 200 days of events in each catalog. Each magnitude range indicates a return to background rate within ~1000 km of the mainshock. This is consistent with a 2-3 fault length aftershock zone. The temporal increase in activity resembles an Omori decay with 6.5 > M < 7.9 activity returning to background rates with in three days and activity for M > 5 is increased for ~100 days. No magnitude range demonstrates an extended decrease in activity below the mean rate. Continued examination of different magnitude, spatial, and temporal ranges is to be completed.

Acknowledgements

This work is based upon work supported by the National Science Foundation Graduate Research Fellowship for C.W. Johnson

References

Brodsky, E. E., Long-range triggered earthquakes that continue after the wave train passes, *Geophys. Res. Lett.*, *33*, L15313, doi:10.1029/2006GL026605, 2006.

Gomberg, J., Reasenberg, P.A., Bodin, P., and Harris, R.A., Earthquake triggering by seismic waves following the Landers and Hector Mine earthquakes, *Nature*, *411*, 462-466, 2001.

Husker, A.L. and Brodsky, E.E., Seismicity in Idaho and Montana triggered by the Denali Fault earthquake: A window into the geologic context for seismic triggering, *Bull. Seis. Soc. Am.*, *94*, S310-S316, 2004.

Parsons, T. and Velasco, A.A., Absence of remotely triggered large earthquakes beyond the mainshock region, *Nature Geosci.*, *4*, 312-316, 2011.

Peng, Z., D. P. Hill, D. R. Shelly, and C. Aiken, Remotely triggered microearthquakes and tremor in central California following the 2010 Mw 8.8 Chile earthquake, *Geophys. Res. Lett.*, *37*, L24312, doi:10.1029/2010GL045462, 2010.

Pollitz, F.F., Stein, R.S., Sevilgen, V, and Bürgmann, R., The 11 April 2012 east Indian Ocean earthquake triggered large aftershocks worldwide, *Nature*, *490*, 250-253, 2012.

Stein, R.S., The role of stress transfer in earthquake occurrence, *Nature*, *402*, 605-609, 1999.

Tape, C., West, M., Silwal, V., and Rupppet, N., Earthquake nucleation and triggering on an optimally oriented fault, *Earth and Plan. Sci. Lett.*, doi:/10.1016/j.epsl.2012.11.060, 2013.

22 Laboratory Investigations into Micromechanical Mechanisms Controlling the Onset of Stick-slip Instabilities

Paul A. Selvadurai, Steven D. Glaser and Rani H. Kiwan

Introduction

Improving our understanding of the factors controlling spontaneous shear rupture nucleation on a frictional fault would help better define the important physical processes contributing to earthquake rupture and faulting. Our current laboratory investigations (*Selvadurai and Glaser,* 2013) quantify the local stress states on a laboratory fault, which control the transition from stable (quasi-static) to unstable (dynamic) sliding. We propose that the initiation of the unstable phase occurs at the displacement incongruities where compliant, 'creeping' segments of the fault transition into stiff, 'locked' sections. These transition regions can exhibit swarms of smaller earthquakes, localized in time and space, prior to the larger subsequent earthquake. Similarities between our laboratory results (specifically the acoustic emission measurements), and those observed in geological settings are briefly described here.

Laboratory Facilities

The laboratory model consisted of two sandblasted Poly(methyl methacrylate) (PMMA) surfaces pressed together by a normal stress (σ_f) and then sheared at a constant velocity (v_p) in a direct shear configuration. Figure 2.22.1 provides a general view of the direct shear apparatus where the PMMA base plate and slider block measured 950 x 950 x 60 mm and 400 x 80 x 10 mm, respectively. A non-contact eddy current sensor array, mounted near the interface, measured the slow, quasi-static motions near the fault and, in nature, are evident in GPS and InSAR data. To measure the relatively quick dynamic stress changes, an array of 16 piezoelectric acoustic emission (AE) sensors were placed along the underside of the base plate; drawing parallels to seismometers deployed in the field. The AE sensors have been accurately calibrated using known source-time functions induced by glass capillary fractures. During the application of the normal pressure, contacting asperities are formed due to the interaction between the two randomly rough surfaces. These interactions are believed to be consistent with processes occurring on natural geological faults. A pressure sensitive film (FUJI™ prescale 12-50 MPa) was used to initially localize, quantify, and measure the heterogeneous normal stresses resulting from the population of asperity contacts.

Laboratory Procedure

Details of the experimental facilities, procedure and material properties of the PMMA are given by Selvadurai and Glaser (2013). Briefly, the fault was firstly characterized using the pressure sensitive film by compressing it throughout the interface using a known nominal stress (σ_f) for a controlled amount of time (t_{hold}) at a known reference location. Using the electro-mechanical shear actuator, the rigid loading platen was driven at a set-point velocity (v_p) to simulate far-field tectonic actions.

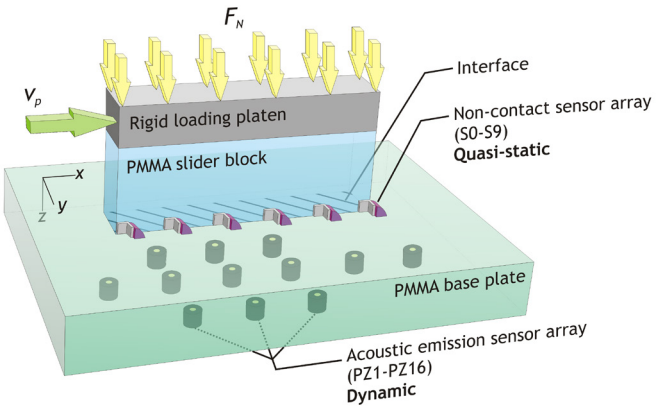

Figure 2.22.1. General schematic view of the overall direct shear apparatus including general locations of the sensors arrays.

Current experimental suites employed constant velocities ranging from 0.010 to 0.030 mm/s but only the results from the faster loading rate, v_p = 0.030 mm/s, will be presented here. Shear stress (τ_f), normalized over the nominal interface area, measured between the loading platen and shear actuator, increased gradually and slow, aseismic 'creeping' displacements were observed using the non-contact sensors until a 'mainshock' occurred. The mainshock was characterized by a sizable decrease in the bulk shear force (~50-70% drop from maximum) coupled with rapid, coseismic displacements in the direction of applied shear.

Experimental Observations: Foreshocks Preceding the Mainshock

Detectable physical changes, such as ground deformations associated with the premonitory movements are difficult (if not impossible) to detect using current geodetic and seismic sensing tools. On some natural faults, smaller earthquakes have occurred within a region tens of kilometers of the eventual hypocenter of the larger earthquake, weeks to seconds beforehand. The physics and mechanics of these 'foreshocks' are not well understood with respect to their influence on the larger mainshock.

In Figure 2.22.2, while loading the fault slowly (v_p = 0.030 mm/s) prior to the mainshock, we observe small dynamic emissions detected using the AE array.

During these 'foreshock' emissions, there was no discernible drop in the bulk shear force (τ_f) sustained by the fault, but they must represent changes in local stress states due to some physical phenomena which we are currently investigating.

Spatio-temporal distributions can also be analyzed. Location and timing of the foreshocks were determined from first arrival P-waves using multiple AE sensors and are shown in Figure 2.22.3. The size of the circular region represents the spatial error associated with the p-wave location algorithm. Locations

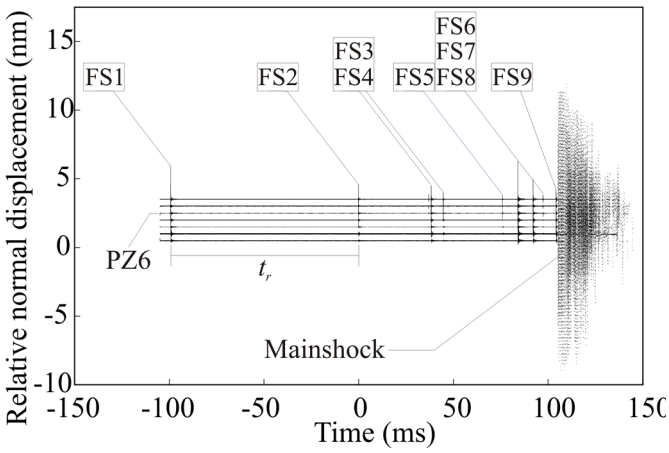

Figure 2.22.2. Acoustic emission measurements for nine foreshocks (FS1-FS9) creating a sequence that preceded a larger mainshock event (v_p = 0.030 mm/s). The recurrence time, t_r, between FS1 and FS2 is shown as an example.

of the foreshocks have been superimposed over the initial contact measurements provided from the pressure sensitive where the hotter (red) colors indicate contact and the cooler (blue) represents zero stress or no initial contact.

Preliminary Discussion

Observational seismology has, in some cases, observed foreshock sequences preceding larger mainshock events (e.g., *Dodge et al.,* 1995) not dissimilar to our preliminary laboratory results. While the scale of the two results are distinctly different (in both space and time) we have currently begun an investigation that employs similar techniques and models to characterize our experimental findings. These techniques may help develop scaling relations from the laboratory to the field that have been difficult to characterize in the past. These foreshock bursts may be useful contributors to short-term earthquake probability estimates (*Chen and Shearer,* 2013).

Acknowledgements

Funding for this work is provided by NSF Grant # 1131582.

References

Chen, X. and Shearer, P. M., California foreshock sequences suggest aseismic triggering process: *Geoph. Res. Lett.*, *v. 40*, p. 1-6, doi:10.1002/grl.50444, 2013.

Dodge, D. A., Beroza, G. C. and Ellsworth, W. L., Foreshock sequence of the 1992 Landers, California, earthquake and its implications for earthquake nucleation: *J Geophys. Res.*, *v. 100*, no. B7, p. 9865-9880, 1995.

Selvadurai, P. A. and Glaser, S. D., Experimental evidence of micromechanical processes that control localization of shear rupture nucleation: Presented at the *47th US Rock Mechanics / Geomechanics Symposium* in San Francisco, CA, USA, 2013.

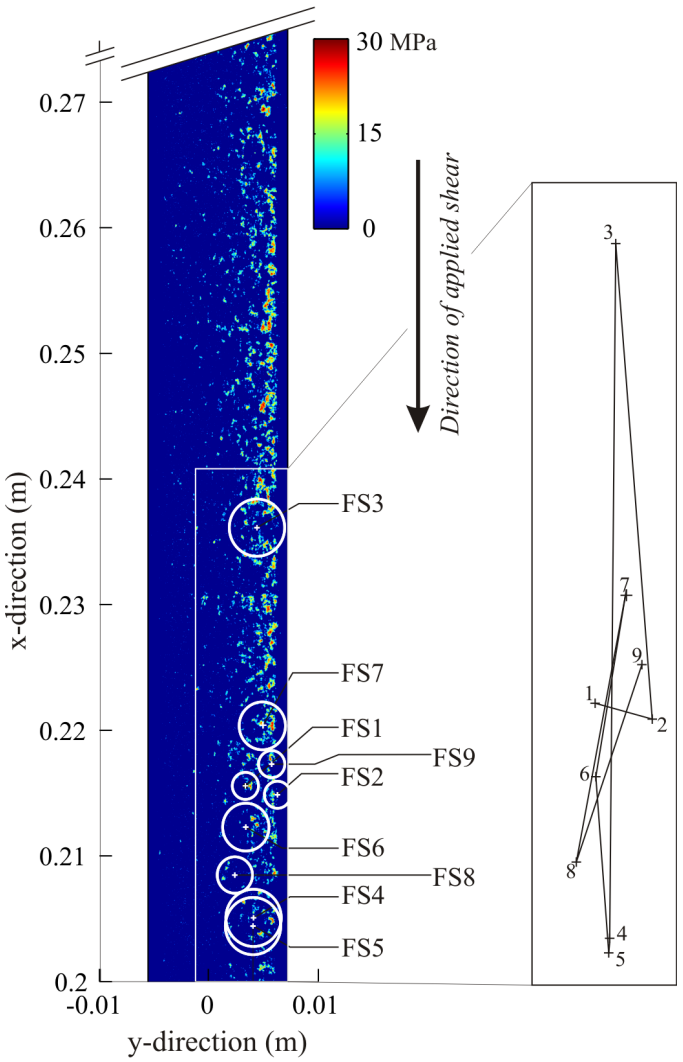

Figure 2.22.3. Locations of the foreshocks shown in Figure 2.22.2 determined using P-wave travel times from multiple sensors. The locations were superimposed on the pressure measurements obtained from the pressure sensitive film. Locations exhibiting higher normal stress appear red while the blue background assumes no normal stress was transferred (i.e., no contact occurred). The inlay shows an enlarged view of the movement of the foreshock sequence where the distribution appears to be random in space.

23 Source Characterization of Underground Explosions from Combined Moment Tensor and First Motion Analysis

Andrea Chiang and Douglas S. Dreger

Introduction

The use of regional distance long-period, complete waveform data to determine the seismic moment tensor and discriminate the source-type of earthquakes, underground cavity collapses and nuclear explosions has been demonstrated for events in the western United States (*Dreger et al.*, 2008; *Ford et al.*, 2008; *Ford et al.*, 2009a), and for the recent 2006 and 2009 North Korean nuclear tests (*Ford et al.*, 2009b; *Ford et al.*, 2010). In these studies populations of earthquakes, underground cavity collapses and nuclear explosions are found to separate when considered on a *Hudson et al.* (1989) source-type diagram. *Ford et al.* (2010) utilized the *Hudson et al.* (1989) source-type representation to develop a network sensitivity solution (NSS) to determine the best fitting solution, the uncertainty in the solution, and the capabilities of the method given the station topology. The regional distance moment tensor inversion, coupled with NSS analysis and first motion constraints, enables the discrimination of source-type in conditions of relatively sparse regional distance monitoring.

Data and Methods

In this study we investigate the September 14, 1988 US-Soviet Joint Verification Experiment (JVE) nuclear test at the Semipalatinsk test site in Eastern Kazakhstan, and two nuclear explosions conducted at the Chinese Lop Nor test site. These events were very sparsely recorded by stations located within 1600 km, and in each case only 3 or 4 stations were available in the far-regional distance range (Figure 2.23.1) for moment tensor analysis. Following the results of *Ford et al.* (2009b) we incorporated first-motion data from regional stations, as well as teleseismic stations to provide additional constraint in the NSS analysis. The results show that unique discrimination of these events is possible under these extremely sparse monitoring conditions when long-period regional waveforms and P-wave first-motion polarities are combined.

To assess the confidence of the moment tensor solution, we implemented the Network Sensitivity Solution (NSS) technique developed by *Ford et al.* (2010). The technique presents the level of fit between data and the different theoretical solutions described by the source-type diagram for a given station configuration, Earth model, and frequency band. From the NSS of a given event we can determine whether or not the best fitting full moment tensor solution from the inversion is well resolved to make useful interpretations about the source. We included regional and/or teleseismic P-wave first motions in addition to waveform data in the NSS analysis (*Ford et al.*, 2012) to better constrain the moment tensor solution by comparing observed P-wave polarities to predicted P-wave polarities.

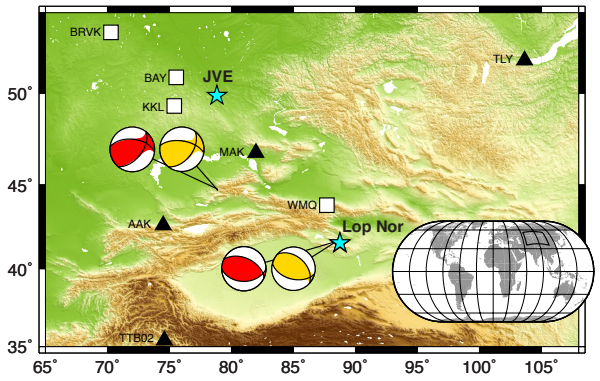

Figure 2.23.1. Event locations (star) and seismic stations (triangle and square) used in the moment tensor analysis. The two Lop Nor events are located very closely hence the overlapping stars. Black triangles represent the stations used in the analysis of the May 15th, 1995 Lop Nor explosion and the June 8th, 1996 Lop Nor explosions, and white squares are the stations used in the September 14th, 1998 Soviet JVE. Focal mechanisms of local earthquakes used in the velocity model calibration are also plotted. Gold is the solution from this study and red is the Harvard GCMT solution.

Network Sensitivity Solutions (NSS)

Here we present the combined waveform and first motion analysis for the three explosions (Figure 2.23.2). For the 1988 JVE, the regional waveforms only the NSS solution shows a similar trend compared to other nuclear explosions (*Ford et al.*, 2010), with the best-fitting full moment tensor solution plotting near the theoretical opening crack. The colors of the shaded contour regions correspond to different scaled variance reduction (sVR), in which the sVR is scaled to the moment tensor solution in the NSS that has the maximum VR. In the case of using just the waveform data, source mechanisms without a significant explosive component can fit the observed data just as well as a dominantly explosive mechanism. However, when regional and teleseismic P-wave first motions are included in the computation of the NSS a solution that is predominately explosive is obtained. The NSS results show significant improvement in discrimination capabilities when we include additional constraints from P-wave first motions, especially for moment tensor solutions fitting better than sVR of 90%.

The two Lop Nor explosions illustrate that when good teleseismic data is not available, using only regional P-wave polarities also improves monitoring capabilities. Waveform-only NSS for the 1995 Lop Nor event show a wide range of possible sources fitting ≥ 90% of the best fitting moment tensor solution, which is largely the result of the large Love wave amplitudes and the sparse station coverage. However, if we use both waveform data and P wave polarities observed at regional distances we see the combined analysis significantly reduces the distribution of

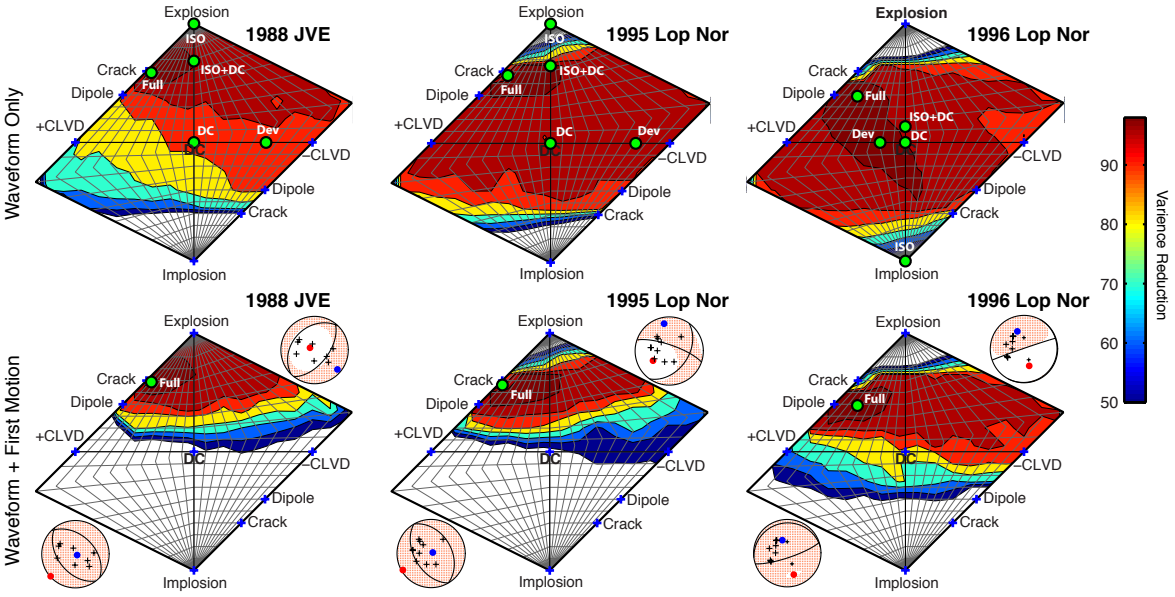

Figure 2.23.2: Network Sensitivity Solutions (NSS) for the 1988 JVE, 1995 and 1996 Lop Nor Shaft Explosions. Green circles are best fitting full, deviatoric, pure double couple (DC), ISO+DC and pure isotropic (ISO) source mechanisms; blue crosses are the theoretical mechanisms; shaded regions are color-coded by their scaled variance reduction (sVR); black crosses, blue dots and red dots plotted on the best fitting full and deviatoric mechanisms are P-wave up first motions, T- and P-axes. Here we compare NSS using regional waveform and combined waveform and P-wave first motion. For the JVE we used both regional and teleseismic first motions, and for the two Lop Nor explosions we used only regional first motions.

solutions with high sVR (≥ 90%) and uniquely discriminates the event as consistent with other nuclear explosions and inconsistent with earthquakes and collapses (Figure 2.23.2).

Similarly, waveform-only NSS for the 1996 Lop Nor event cannot uniquely discriminate the event as a explosive source due to strong Love waves, sparse station coverage, and possible Rayleigh wave reversal. However, after incorporating regional P-wave first motions, the NSS results now show similar trends as observed in the 1995 Lop Nor test and the 1988 Soviet JVE, though contours showing solutions with sVR ≥ 90% are more extensive and cross slightly over to the horizontal deviatoric line (Figure 2.23.2). Although the combined waveform and first motion NSS does not give a unique discrimination, it identifies the source as non-DC. Unlike earthquakes, the distribution of moment tensor solutions is not situated around the pure DC mechanism but shifted along the vertical volumetric axis and towards an opening linear vector dipole.

Conclusions

We have performed seismic moment tensor inversions for the 1988 Soviet JVE test and two Lop Nor nuclear tests. These cases represent sparse monitoring conditions. In each case we have shown that the use of long-period waveform data comprised mostly of regional surface waves results in solutions with large isotropic components that are consistent with solutions for other studied nuclear tests (*Ford et al.*, 2009a; *Ford et al.*, 2009b; *Ford et al.*, 2010). Using only regional waveforms, the distribution of solutions on the source type diagram of *Hudson et al.* (1989) do not cleanly discriminate the event either because of the known explosion negative compensated linear vector dipole (CLVD) tradeoff (case of the JVE event) or due to large observed Love waves (cases of the two Lop Nor tests). In each case, however, the inclusion of regional P-wave polarities, and ideally observations from teleseismic arrays when available, reduces area of solutions that provide a good level of fit to the data, providing good separation from double-couple solutions and solutions on the deviatoric line.

Acknowledgements

We acknowledge funding from the Air Force Research Laboratory, contract FA9453-10-C-0263 that is supporting this research.

References

Dreger, D. S., Ford, S. R., and Walter, W. R., Source Analysis of the Crandall Canyon, Utah, Mine Collapse, *Science*, *321*, 217, 2008.

Ford, S. R., Dreger, D. S. and Walter, W. R., Source Characterization of the 6 August 2007 Crandall Canyon Mine Seismic Event in Central Utah, Seismol. Res. Lett., 79, 637-644, 2008.

Ford, S. R., Dreger, D. S. and Walter, W. R., Source Analysis of the Memorial Day Explosion, Kimchaek, North Korea, Geophys. Res. Lett., 36, 2009

Ford, S. R., Dreger, D. S. and Walter, W. R., Identifying Isotropic Events Using a Regional Moment Tensor Inversion, *J. Geophys. Res., 114*, 2009.

Ford, S. R., Dreger, D. S. and Walter, W. R., Network Sensitivity Solutions for Regional Moment-Tensor Inversions, *Bull. Seismol. Soc. Am., 100*, 1962-1970, 2010

Ford, S. R., Walter, W. R. and Dreger, D. S., Event Discrimination Using Regional Moment Tensors, *Bull. Seismol. Soc. Am., 102*, 867-872, 2012

Hudson, J. A., Pearce, R. G., and Rogers, R. M., Source type plot for inversion of the moment tensor, J. Geophys. Res., 94, 765-774. 1989.

24 Moment Tensor Inversion of Seismic Events Associated with the Sinkhole at Napoleonville Salt Dome, Louisiana

Avinash Nayak and Douglas S. Dreger

Introduction

Napoleonville Salt Dome is located near Bayou Corne, Assumption Parish, southeast Louisiana. Caverns in salt domes such as this one are used for brine mining and storage of hydrocarbons and industrial waste. Beginning in June 2012, residents of Bayou Corne reported unusual gas bubbling in surface waters and frequent tremors. The parish requested the assistance of the United States Geological Survey (USGS) to monitor the continuous seismic activity. A temporary network of broadband seismic stations was established which revealed a complex and rich sequence of numerous seismic events. On August 3, 2012, a large sinkhole (Figure 2.24.1) was reported close to the western edge of the salt dome leading to an emergency declaration and evacuation of nearby residents. The sinkhole, filled with a slurry of water, crude oil and debris, has since swallowed Cypress trees and has been growing in surface area ever since (presently > 20,000 m^2). Subsidence, bubbling of natural gas and intermittent seismicity have been observed in the region. Preliminary investigation suggests that sidewall collapse of a cavern, OXY GEISMAR #3, might be a possible cause of the sinkhole. Readers are referred to public briefings reports on the Department of Natural Resources, Louisiana website for further details (http://dnr.louisiana.gov/index.cfm?md=pagebuilder&tmp=home&pid=1051).

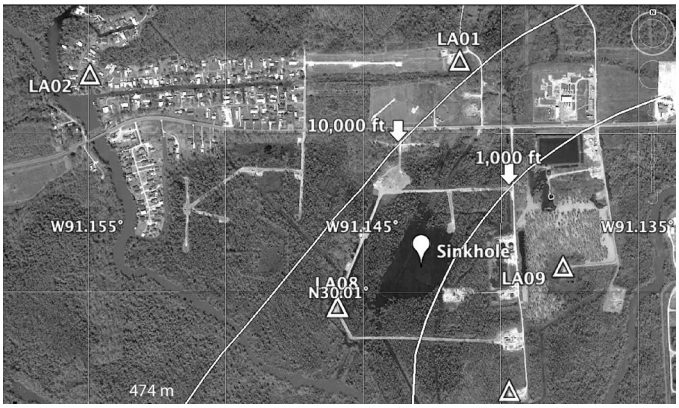

Figure 2.24.1: Google Earth image (dated – March 12, 2013) of the study region showing locations of USGS stations (triangles), sinkhole (balloon) and approximate contours (solid lines) of the edge of Napoleonville salt dome at 1,000 feet and 10,000 feet depth.

This region (-91.16°E to -91.13°E, 30°N to 30.025°N,) has been previously aseismic, with no events reported in the *National Earthquake Information Center* catalog between January 1973 and April 2012. Therefore, the sudden intense seismicity occurring simultaneously with development of the sinkhole indicates that the two phenomena are probably related. In this study, we implement an approach for automatic detection, location and moment tensor inversion of seismic events at the sinkhole.

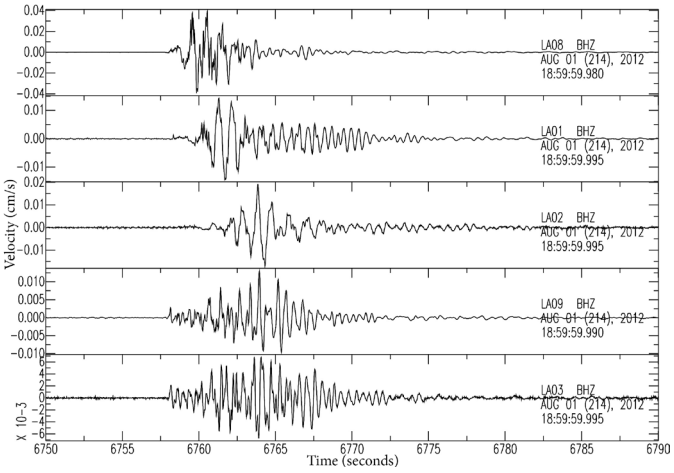

Figure 2.24.2: Velocity waveforms of a representative event.

Data and Methodology

Figure 2.24.2 shows velocity waveforms of a seismic event on August 1, 2012 as recorded at five USGS stations. The records primarily show that strong surface waves and waveforms of multiple events are quite similar to each other, indicating closely spaced hypocenters and a repetitive source process. Three of these stations, *LA01*, *LA02* and *LA08*, are on the sedimentary strata surrounding the sinkhole and show similar waveforms, but are quite different from waveforms at stations *LA03* and *LA09*, which are on sedimentary deposits over the salt dome. The difference in waveforms is reflected in the available seismic velocity models (*William Ellsworth, personal comm.*), which show the salt dome to be a fast half-space, overlain and surrounded by slow layers of sediments with velocities smoothly increasing with depth. To study source mechanisms of these events, we perform six-component point source seismic moment tensor inversion allowing for both deviatoric mechanisms and volume changes (*Minson and Dreger*, 2008). Due to the uncertainties in travel-time locations and depths owing to lack of clear seismic phases in waveforms and presence of numerous seismic events, we employ the grid search approach of *Kawakatsu* (1998) which continuously scans the seismic wavefield and performs moment tensor inversion of low frequency waveforms assuming virtual sources distributed over a 3D grid. For a given window of data, the source location and moment tensor solution which give the best Variance Reduction (VR), a measure of normalized fit between observed and synthetic waveforms, is assumed to be the true seismic source. We assume that seismic paths to stations *LA01*, *LA02* and *LA08* conform to sediment velocity model and seismic paths to stations *LA03* and *LA09* conform to salt dome velocity model. Fundamental Green's functions for the 1D velocity models are computed using *FKRPROG* (*Saikia*, 1994). Displacement records are bandpass filtered between 0.1 to 0.2

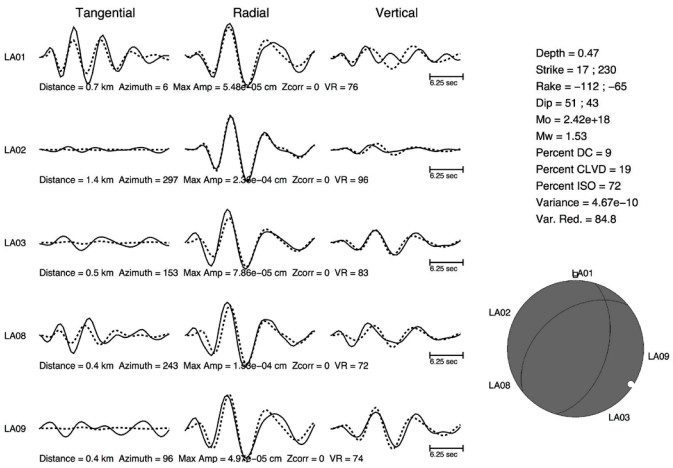

Figure 2.24.3: Observed (solid lines) and synthetic (dashed lines) waveforms and the moment tensor solution for one event.

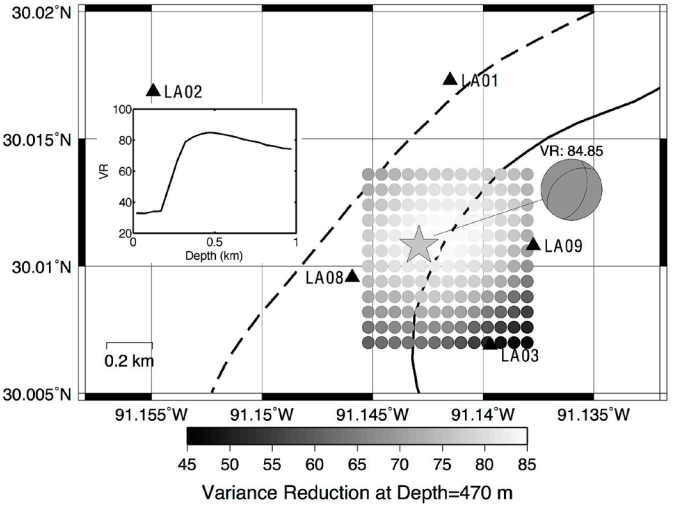

Figure 2.24.4. Figure showing distribution of *VR* in horizontal directions at best depth and distribution of best *VR* with depth (inset).

Hz, which simplifies the waveforms while maintaining the signal to noise contrast for larger events. The same causal filter is used for Green's functions. Then, the moment tensor inversion is performed for each grid point using 25-seconds data windows with time steps of 0.25 seconds. Here we discuss results for 5 hours of data from 17:00 hours to 24:00 hours on August 01, 2012. We were able to detect 23 events using a threshold of 70% VR during this time period. The details of the moment tensor solution and corresponding waveform fits for one of the events are shown in Figures 2.24.3. This event was located at -91.1422°E, 30.0112°N, depth 0.47 km and centroid time 20:52:39.00 hours. The solution fits the data very well at 84% VR and can explain most of the strong radial and vertical components. We find a dominant volume increase component in the solution (Isotropic > 70%). The distribution of VR in space (Figure 2.24.4) shows that our location is well constrained. All solutions are quite similar showing a dominant volume increase component (Isotropic 64-74%) and are concentrated at a depth of ~ 470 m at the western edge of the salt dome, very close to the present location of the sinkhole. Magnitudes range from M_w 1.3 to 1.7.

Discussions

The moment tensor solutions are opposite to what one would expect in a collapse environment, if the energy release were purely due to gravity-driven tectonic collapse alone. However, the presence of large volume increase components as well as occurrence of harmonic tremors and long period events in the region indicates the role of fluids in controlling the seismic source processes, which can be inferred to be due to tensile failure of a near-vertical crack, or a crack-double-couple on a normal fault in the salt. Future work will include studying sensitivity of moment tensor solutions to velocity models, modeling waveforms at higher frequencies and possible explanations of the source mechanisms in terms of physical processes and their relationships with the sinkhole.

Acknowledgements

We thank William Ellsworth (USGS) for preliminary velocity models, data, mapping resources and helpful discussions. We also thank Aurelie Guilhem (ETH Zurich) and Seung Hoon Yoo (BSL) for helpful discussions. A. Nayak wishes to acknowledge the BSL Byerly/Tocher grant in supporting this work.

References

Kawakatsu, H., On the realtime monitoring of the long-period seismic wavefield: *Bull. Earthq. Res. Inst.*, 73, 267-274, 1998.

Minson, S.E., and D.S. Dreger, Stable Inversion for complete moment tensor: *Geophys. J. Int.*, 174, 585-592, 2007.

Saikia, C.K., Modified frequency-wavenumber algorithm for regional seismograms using Filon's quadrature: modeling Lg waves in eastern North America: *Geophys. J. Int.*, 118, 142–158, 1994.

25 Full Moment Tensor Solutions Constrained using First Motion Polarities for Seismicity at the Geysers Geothermal Field, California

Voon Hui Lai, Sierra Boyd, Douglas Dreger

Introduction

The Geysers Geothermal Field is one of the most seismically active regions in North America. There have been previous efforts to study the source parameters of these earthquakes with magnitude greater than M_w 3.0 in this region by computing the deviatoric and full moment tensor solutions for these events (*Boyd*, 2013). However, for earthquakes that have a small volumetric term, statistical analysis such as the F-test is insufficient to provide good measure of significance to the full moment tensor (FMT) solutions. Hence, we incorporate first motion polarities to provide the additional constraint to the FMT solutions.

Methodology

Five earthquakes are chosen for further investigation. The first motion polarity data takes into account four parameters: station azimuth from the epicenter, takeoff angle, polarity (up or down) of first P arrivals, and a weighing factor. An average of 150 seismic stations from Northern California (NCSN), Berkeley Digital (BDSN), and Lawrence Berkeley National Lab (LBNL) Seismic Networks are used to ensure good azimuthal coverage. Both azimuth and takeoff angle for each station are obtained from the Northern California Earthquake Data Center (NCEDC) catalog and the polarities of the vertical component of each station are visually reviewed using Seismic Analysis Code (SAC) and Jiggle, developed by U.S. Geological Survey (USGS). A weighting is introduced to account for the uncertainties in determining the first motion polarities, which primarily stem from: (1) emergent signals which are common for head waves (or Pn phase), (2) low signal to noise ratio and (3) acausal ringing for stations that use an acausal filter and are situated close to the epicenter. Impulsive signals are assigned higher weight to reflect higher confidence in picking; lower weights are assigned to emerging polarities. Ambiguous polarities are removed from the analysis.

The first motion polarities are then incorporated into the Network Sensitivity Solutions (NSS) developed by *Ford et al.* (2010). NSS calculates the variance reduction (VR) for each synthetic source and plots it as a function of source-type parameter on a source-type plot. Using NSS, we first compute 200 million possible moment tensor solutions using the waveform data. Solutions with positive values of VR are then tested against the first motion data, and a combined VR is computed. The maximum VR fit surface is plotted on the *Hudson et al.* (1989) source-type diagram.

Results and Discussion

For events occurring on March 1, 2011 and February 24, 2008, we observe that using the combined dataset, the region representing the best-fit source model with VR greater than 95% in the source-type diagram (see Figure 2.25.1b) is significantly reduced in area. For the March 1, 2011 event, the best-fit source model is composed of 79% double couple (DC), 3% +compensated linear vector dipole (+CLVD) and 18% isotropic (ISO) components. For the February 24, 2008 event, the best-fit source model is composed of 22% DC, 30% +CLVD, and 48% ISO components. For both events, the constrained FMT solution shows consistency on the ISO component compared to the unconstrained FMT solution.

For both events, the first motion constrained FMT solution provides superior fit to the first motion polarities, closely followed by the unconstrained FMT solution (see Figure 2.25.1). In contrast, the deviatoric solution does not fit well the polarity data as demonstrated by the negative fit value. In conclusion, there is a higher confidence in the FMT solution as it fits better with the first motion polarities. The polarity data is also useful in determining the source parameters for an earthquake by providing a good constraint to the FMT solution. The preferred source mechanism for the earthquake is the best-fit source model obtained from NSS using both waveform data and first motion polarities.

Acknowledgements

This work is supported by the Department of Energy Geothermal Technologies Program under Award Number DD-EE0002756-002. We would like to thank A. Chiang, A. Guilhem, P. Hellweg, P. Lombard, and S.H. Yoo for their support.

References

Boyd, O. S., D. S. Dreger, V. H. Lai, and R. Gritto, Full Moment Tensor Analysis Using First Motion Data at the Geysers Geothermal Field. PROCEEDINGS, 38th Geothermal Reservoir Engineering Workshop, SGP-TR-98, 2013.

Ford, S. R., D. S. Dreger and W. R. Walter, Network sensitivity solutions for regional moment tensor inversions, *Bull. Seism. Soc. Am., 100*, 1962-1970, 2010.

Hudson, J. A., Pearce, R. G., and Rogers, R. M., Source type plot for inversion of the moment tensor, *J. Geophys. Res., 94*, 765-774, 1989.

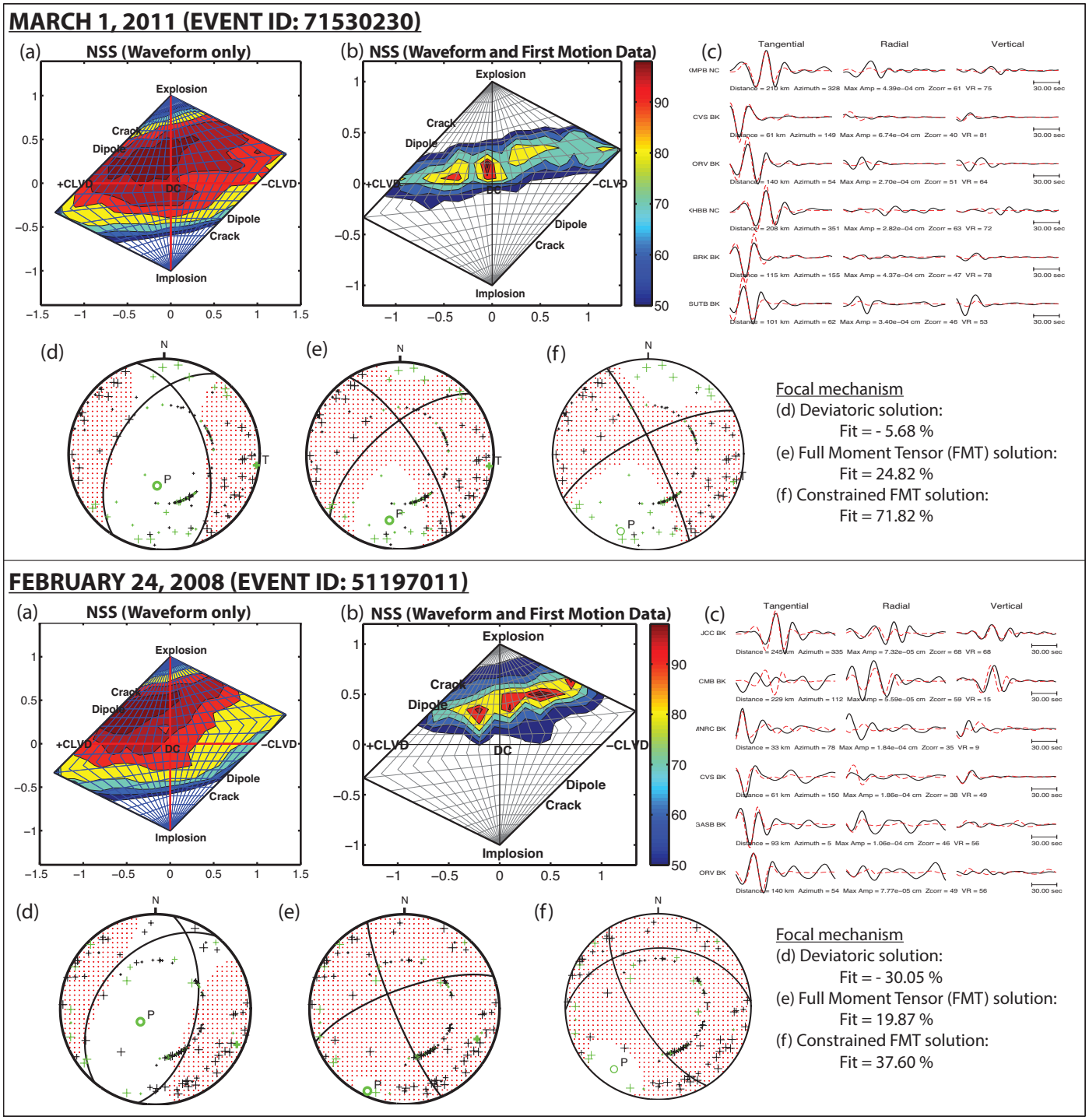

Figure 2.25.1: Source type plots for the NSS result using (a) waveform data and (b) the waveform constrained with first motion polarities. Warmer colors represent higher VR for the best-fit source model for each event. The plots show the VR scaled to the maximum fit value for each case. We also compare (c) the synthetic waveform computed using the constrained full moment tensor (FMT) soltuion (indicated by red dash line) with the observed waveform data (indicated by the black solid line) and show that they compare reasonably well with high variance reduction, particularly for March 1, 2011 event which its VR equals to 74.1%. Focal mechanisms of (d) deviatoric solution, (e) unconstrained FMT solution and (f) constrained FMT solution overlaid with the polarity information are also shown here. Red shaded region represents compressional which is dominated by "up" first motions (shown by black "+" signs) while the white region represents represent dilatation, dominated by "down" first motions (green "+" signs). The weighting corresponds to the size of the "+" sign where the bigger "+" sign means higher confidence in picking. The "+" signs in the inner circle typically represent head-wave arrivals at stations with small takeoff angle and are useful to constrain the nodal planes

26 TremorScope: Imaging the Deep Workings of the San Andreas Fault

Roland Bürgmann, Richard Allen, Douglas Dreger, Robert Nadeau, Barbara Romanowicz, Taka'aki Taira, Margaret Hellweg

Introduction

Until recently, active fault zones were thought to deform via seismic slip during earthquakes in the upper, brittle portion of the crust, and by steady, aseismic shear below. However, in the past decade, this view has been shaken by seismological observations of seismic tremor deep in the roots of active fault zones. First recognized on subduction zones in Japan and the Pacific Northwest, tremor has also been found to be very active on a short section of the San Andreas Fault to the southeast of one of the most densely monitored fault segments in the world, near Parkfield, CA (*Nadeau and Dolenc*, 2005). This deep (~20-30 km) zone of activity is located right below the nucleation zone of the great 1857 Fort Tejon earthquake, estimated to be an *M*7.9 event. Thus, learning more about the temporally and spatially complex faulting processes in this zone may help us better understand the conditions that lead to such large ruptures.

Figure 2.26.1. Installation of the seismic vault at TremorScope station TRAM.

The Project Plan and Implementation

The tremor source region is southeast of existing seismic networks around Parkfield, along the San Andreas Fault. We are adding eight seismic stations—the TremorScope (TS) network—in this area to complement existing instrumentation.

Now, all sites for the TS network have been permitted and all four surface stations have been installed, two in this past year. Figure 2.26.1 shows the installation of the seismometer vault at station TRAM, just above the centroid of the tremor sources. Surface installations have a broadband seismometer, an accelerometer and a digitizer. Station TRAM will also host one of the four boreholes. The borehole sites, with a hole about 300 m deep, will have an accelerometer at the surface. Seismometers, accelerometers and geophones will be installed at the bottom of these boreholes, where the levels of environmental and human-induced noise are much lower than at the surface, so the weak tremor signals will be more easily detected and analyzed. We defined the specifications for the boreholes, including target depth and casing options. In late-June, we hosted a pre-bid walk-through for prospective drilling companies to introduce them to the drilling sites in preparation for their bids. Downhole will be a three-component set of gimballed, 2 Hz geophones. Three boreholes will also be equipped with a Guralp downhole sensor package, consisting of a three-component broadband seismometer, a three-component accelerometer and a digitizer. At all locations, data will be logged onsite and forwarded to Berkeley for real-time processing. The data will be used in real-time earthquake monitoring (see Operational Section 3.1) as well as for tremor studies. Data are now being archived and analyzed from the four surface stations.

Figure 2.26.2 shows non-volcanic tremor in the Parkfield region on May 8th, 2013. This type of tremor is hard to detect at just one station because it has a low diffuse signal that lasts for minutes. The TS network is located very near the source of these tremors and we can clearly pick up the signal on multiple

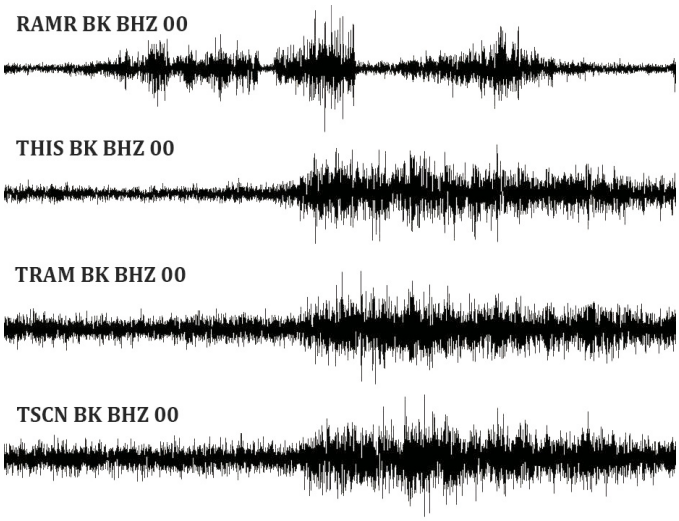

Figure 2.26.2: Non-volcanic tremor as seen on the TS network in the Parkfield, CA region on May 8th, 2013. The concurrence of the signal on the lower three seismograms shows that this is not locally generated noise. Station RAMR, however, is farther away and does not pick up the tremor.

stations (THIS, TRAM, TSCN) and confirm that this is indeed tremor. In contrast, station RAMR is located about 50 km away from the source region and no identifiable tremor signal is visible.

Results

Figure 2.26.3 depicts a map of the Parkfield, California area. The stars are locations of tremor bursts occurring 90 days prior to June 9th, 2013. Red stars are the five most recent tremor bursts. The solid and dotted lines in both panels represent the locked and creeping portions of the San Andreas Fault, respect-

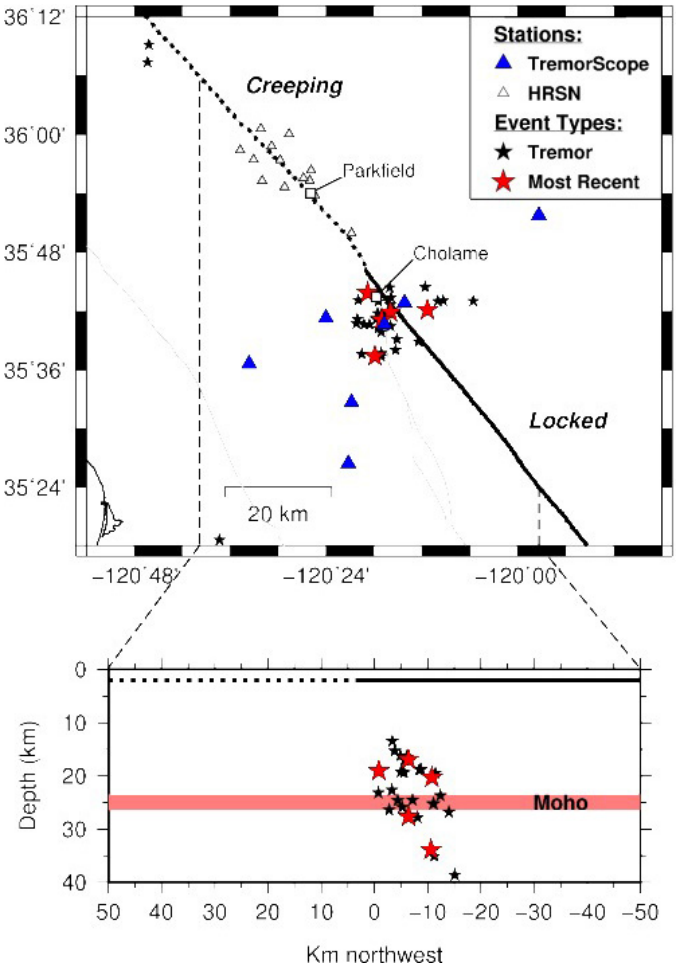

Figure 2.26.3: Map showing the 90 days of tremor prior to June 9th, 2013.

ively. The white triangles are sensitive borehole stations of the High Resolution Seismic Network (HRSN) used in the detections, and the Tremorscope stations are shown as blue triangles. The towns of Parkfield and Cholame are the labeled squares. The bottom panel shows the locations of the tremor episodes in depth section along the fault. The pink horizontal line represents the Moho in the area. To look at the most recent tremor, go to http://seismo.berkeley.edu/research/recent_tremor.html

Perspectives

Data from the TremorScope project will improve earthquake tremor monitoring in the region south of Parkfield. Insights from the project will also contribute to an understanding of tremor and slip in other regions of the world where such phenomena have been observed, but are not nearly as accessible. Should a great San Andreas earthquake occur during this experiment, the network would also provide unprecedented and exciting insights into the seismic rupture process. In addition, the BSL received the go-ahead from the university to submit a "major research initiative", or MRI, proposal to the National Science Foundation for tracking fault processes on the deep San Andreas with a high-sensitivity seismic array of borehole stations. This project would use the TremorScope instrumentation as leverage to increase and improve seismic monitoring throughout the area and improve our understanding of the transition in fault behavior between the locked San Andreas Fault in the Fort Tejon/Carizo Plains segment and the creeping section to the northwest of Parkfield.

Acknowledgements

This work is funded by grant 2754 from the Gordon and Betty Moore Foundation.

References

Nadeau, R., and Dolenc, D., Nonvolcanic tremors deep beneath the San Andreas fault, *Science*, *307*, 389, doi:10.1126/science.1107142, 2005.

27 Near Real-Time Infragravity Noise Removal for the Monterey Ocean Bottom Broadband (MOBB) Station

Zhao Zheng, Taka'aki Taira, Barbara Romanowicz

Introduction

The Monterey Ocean Bottom Broadband (MOBB) seismic station is located 40 km offshore in the Monterey Bay, CA, at a water depth of ~1,000 m (*Romanowicz et al.*, 2003; 2006). Since 2009, data have been available in real time via cable connection to the nearby MARS (Monterey Accelerated Research System) node (http://www.mbari.org/mars) (*Romanowicz et al.*, 2009). So far, MOBB is the only offshore permanent broadband station in central California besides the island-based Farallon Islands station (FARB). It therefore provides important complementary azimuthal coverage for seismicity on the San Andreas Fault system.

However, the usage of MOBB seismic data for purposes such as regional moment tensor (MT) determination has been greatly restricted due to severe noise from seafloor deformation forced by ocean infragravity (IG) waves. Given the water depth at MOBB, the IG-induced noise on the vertical component seismogram peaks in 20-200s (*Dolenc et al.*, 2005), which overlaps with the band (10-100 s) for regional MT analysis.

Fortunately, MOBB contains a Differential Pressure Gauge (DPG) which provides continuous water pressure recordings at a sufficiently high sampling rate (1 sps). It has been noticed that a strong correlation exists between seafloor vertical ground motion and pressure in the IG band (*Dolenc et al.*, 2005). A transfer function (TF) between the two components can therefore be defined and utilized to remove the IG noise from vertical component seismogram (*Webb and Crawford*, 1999; *Crawford and Webb*, 2000; *Crawford et al.*, 2006; *Dolenc et al.*, 2007). If the TF is time invariant, then it can be pre-computed and used in a real-time fashion for noise removal.

Method

Following *Webb and Crawford* (1999), the transfer function T(ω) can be expressed as

$$T(\omega) = \gamma(\omega)\sqrt{G_{SS}(\omega)/G_{PP}(\omega)} \qquad (27.1)$$

where GSS(ω) and GPP(ω) are the one-sided auto-spectral density functions for the vertical component seismic and the pressure records, respectively, and γ(ω) is the coherence between the two components defined as (*Bendat and Piersol*, 1986):

$$\gamma(\omega) = G_{SP}(\omega)/\sqrt{G_{SS}(\omega)G_{PP}(\omega)} \qquad (27.2)$$

with $G_{SP}(\omega)$ being the one-sided cross-spectral density function between seismic and pressure records. Following *Crawford and Webb* (2000), we estimate $G_{SS}(\omega)$, $G_{PP}(\omega)$, and $G_{SP}(\omega)$ from $S(\omega)$ and $P(\omega)$, the spectrum of the seismic and the pressure record:

$$G_{SS}(\omega) = \left(\frac{2}{NL}\right)\sum_{i=1}^{N}|S_i(\omega)|^2 \qquad (27.3)$$

$$G_{PP}(\omega) = \left(\frac{2}{NL}\right)\sum_{i=1}^{N}|P_i(\omega)|^2 \qquad (27.4)$$

$$G_{SP}(\omega) = \left(\frac{2}{NL}\right)\sum_{i=1}^{N}S_i^{*}(\omega)P_i(\omega) \qquad (27.5)$$

where *i* is the index of the data segment that enters the average, *N* the number of data segments, and *L* the length of each segment. In this study, we calculate the *G* terms for each day by breaking 1 day's data into 8 non-overlapping 3-hour segments and taking the average. We have tried other values of *N* and *L* and determine that this set is optimal.

The part of energy that is coherent with the pressure record is then subtracted from the seismogram:

$$S'(\omega) = S(\omega) - T_i^{*}(\omega)P(\omega) \qquad (27.6)$$

Then an inverse Fourier transform of $S'(\omega)$ is taken to obtain the corrected seismogram in the time domain.

The success of the method relies upon the high coherence between the seismogram and the DPG in the IG band. In a related study (*Taira et al.*, 2013), the authors have confirmed that the coherence is indeed high ($\gamma^2(\omega)$ median > 0.995 in the period range of 30-200s) for MOBB.

Results

We systematically calculate the TFs from each day from Apr 2009–Feb 2010 and July 2011–June 2012 when data are available (the gap in between was due to a cable trawl incident). We have also examined the time before 2009, however these data have many issues. These 1-day TFs are then compared to examine their temporal variability (Fig. 2.27.1). We discover that the TF is generally stable over time, except for an abrupt change from 2010 to 2011, which was due to a DPG replacement in July 2011. One reference TF is obtained for 2009-2010 and 2011-2012, respectively. As a side note, despite nominally being identical, different DPGs have notably different calibrations, which may be a relevant concern for other OBS deployments and related studies. The reference TF needs to be recalibrated every time the instrument is replaced.

We then utilize the reference TF for noise removal. Fig. 2.27.2 shows an example of an M_w 4.3 local earthquake. The method proves successful. We then include the cleaned MOBB data for MT inversion. As shown in Fig. 2.27.3 for several local earthquakes, significant improvements in variance reduction are achieved. This noise removal method has been incorporated in the MT determination code of the Northern California Seismic System.

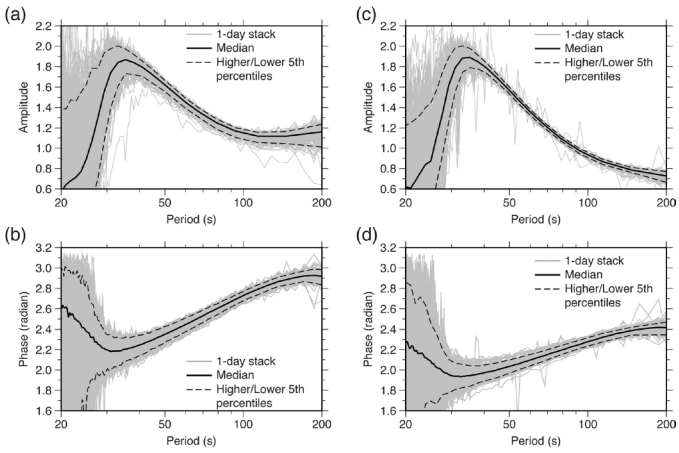

Figure 2.27.1: Amplitude (a,c) and phase (b,d) responses of the 1-day transfer functions (TFs) in the time intervals 2009-2010 (left) and 2011-2012 (right). In each plot, the individual TFs are the cluster of gray curves; the solid curve shows the median, and the two dashed curves show the higher and lower 5th percentiles of the ensemble.

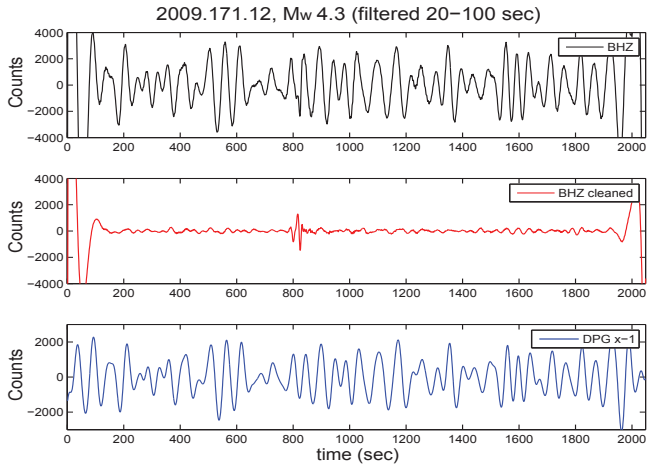

Figure 2.27.2: MOBB waveforms for an M_w 4.3 local earthquake. From top to bottom: the vertical component seismogram before the noise removal using the reference TF for the time interval of 2009–2010; the vertical component seismogram after the noise removal; the DPG record (sign flipped). All traces are filtered in 20-100 seconds.

Acknowledgements

MOBB data are downloaded from the NCEDC. D. Dolenc kindly provided us with the codes for computing power spectral density and transfer functions. This study was supported by the NSF Grant OCE-9911392 and OCE-0648302.

References

Bendat, J. S., and A. G. Piersol, Random Data: Analysis and Measurement Procedures, John Wiley and Sons, New York, 1986, 566 pp.

Crawford, W. C., and S. C. Webb, Identifying and removing tilt noise from low-frequency (<0.1 Hz) seafloor vertical seismic data, *Bull. Seismol. Soc. Am. 90*(4), 952–963, 2000.

Crawford, W. C., Stephen, R. A., and Bolmer, S. T., A second look at low-frequency marine vertical seismometer data quality at the OSN-1 site off Hawaii for seafloor, buried, and borehole emplacements, *Bull. Seismol. Soc. Am. 96*(5), 1952-1960, 2006.

Dolenc, D., Romanowicz, B., Stakes, D., McGill, P., and Neuhauser, D., Observations of infragravity waves at the Monterey ocean bottom broadband station (MOBB). *Geochem. Geophys. Geosyst.*, *6*, Q09002, 2005.

Dolenc, D., B. Romanowicz, R. Uhrhammer, P. McGill, D. Neuhauser, and D. Stakes, Identifying and removing noise from the Monterey ocean bottom broadband seismic station (MOBB) data, *Geochem. Geophys. Geosyst.*, *8*, Q02005, 2007.

Romanowicz, B., Stakes, D., Uhrhammer, R., McGill, P., Neuhauser, D., Ramirez, T., and Dolenc, D, The MOBB experiment: A prototype permanent off-shore ocean bottom broadband station. *Eos Trans., AGU 84*(34), 325, 2003.

Romanowicz, B., Stakes, D., Dolenc, D., Neuhauser, D., McGill, P., Uhrhammer, R., and Ramirez, T. The Monterey Bay broadband ocean bottom seismic observatory. *Ann. Geophys. 49*, 607-623. 2006.

Romanowicz, B., McGill, P., Neuhauser, D., and Dolenc, D. Acquiring real time data from the broadband ocean bottom seismic observatory at Monterey Bay (MOBB). *Seism. Res. Lett.*, *80*(2), 197-202, 2009.

Taira, T., Zheng, Z. and Romanowicz, B., On the Systematic Long Period Noise Reduction on Ocean Floor Broadband Seismic Sensors Collocated with Differential Pressure Gauges, *Bull. Seism. Soc. Am.*, in review, 2013.

Webb, S. C., and W. C. Crawford, Long period seafloor seismology and deformation under ocean waves, *Bull. Seis. Soc. Am. 89*, 1535-1542, 1999.

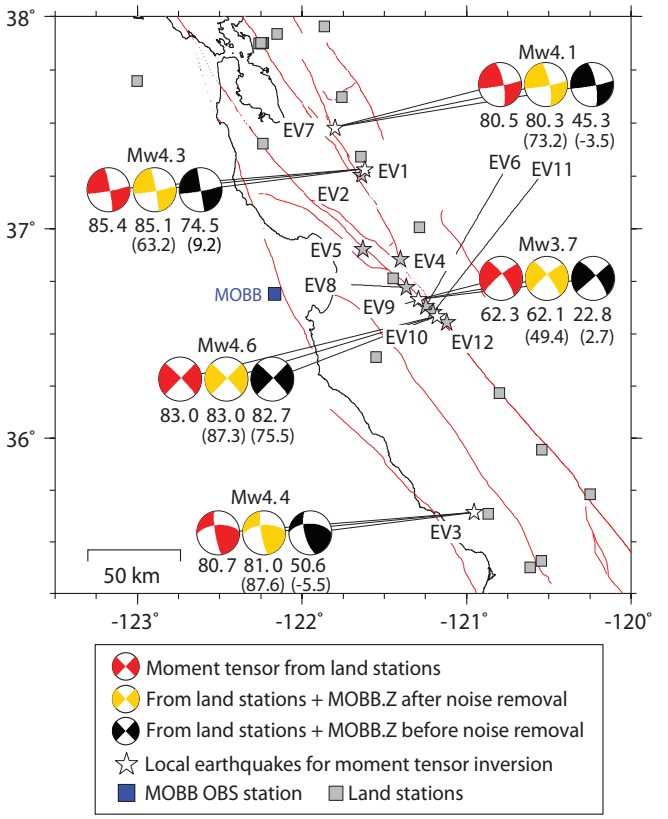

Figure 2.27.3. Comparison of moment tensor solutions with cleaned and uncleaned MOBB data for five local earthquakes. The number below each beachball is the variance reduction (VR) of waveform fit. The numbers in parentheses are the VR when only MOBB is used.

28 Potential Applications Using a Smartphone Network

Qingkai Kong, Richard Allen

Introduction

We are continuing to explore the use of the accelerometer in smartphones to detect earthquakes and the potential scientific applications of using such a dense network. Although the smartphone network does not exist at this point, we are starting to think about how we could use the data for scientific research and applications by using an analogous dataset. We are using the Nodal Seismic Array deployed by the NodalSeismic Company. This array has a nominal station spacing of about 120 m and was designed for active source exploration of petroleum resources. It occupied over 5200 sites with 10 Hz vertical component seismometers in the heavily urbanized area of Long Beach, CA. The dimensions of the array are 7 km by 10 km.

Methodologies

(1) P-wave arrival time residual

We first picked the P-wave arrival time of a magnitude 2.4 earthquake (2011-05-14 04:19:15) for each of the stations using the STA/LTA algorithm (*Allen* 1978) combined with manual picking. Then we extracted a 1D structure model from the 3D velocity model for southern California (*Magistrale et al.* 1996). We used TauP package (*Crotwell et al.* 1999) to predict the arrival time of the P wave using the extracted velocity model. We then subtracted the observed travel time from the predicted time. Removing the linear trend produced the residual travel time map in Figure 2.28.1

(2) Helmholtz Tomography

We implemented the Eikonal/Helmholtz tomography method first proposed by *Lin et al.* 2009. This method uses the Eikonal equation (e.g. *Wielandt* 1993; *Shearer* 1999)

$$\frac{1}{c_i(r)^2} = |\nabla\tau(r_i, r)|^2 - \frac{\nabla^2 A_i(r)}{A_i(r)\omega^2} \qquad (1.1)$$

which is derived directly from the Helmholtz equation. In this equation, c_i is the phase speed for traveltime surface i at position r, ω is the frequency and A is the amplitude of an elastic wave at position r. From this equation, we can directly relate the travel time of the waves with the phase velocity at each station point without doing an inversion. Using the above equation to get the phase velocity is called Helmholtz tomography. If high frequencies are used, or the spatial variation of the amplitude field is small compared with the gradient of the travel time surface, then the second term on the right-hand side can be dropped. This forms the basis of Eikonal tomography. Lin applied this Eikonal tomography to ambient noise of this dense array and then inverted this into a 3D structure. We apply this Helmholtz tomography method to the same earthquake we used above, and get a phase velocity structure as shown in Figure 2.28.2.

Initial results and future work

From the two figures, we can see some evidence of the shallow structure in this area (the depth of the earthquake is 11.9 km, and the distance from the epicenter to the edge of the array is about 6.5 km). Some obvious structures associated with the faults can be seen. With only one small earthquake, it is hard to tell the real structure in this area. But this shows the potential of using the dense network, like the smartphone network, to study the earth structure. We are now developing our 2nd generation application for the smartphones for collecting earthquake data, and building a prototype smartphone network with Deutsche Telecom (Silicon Valley Innovation Center). A network consisting of these smartphones may work as a supplement network to the current traditional network for scientific research and real-time application.

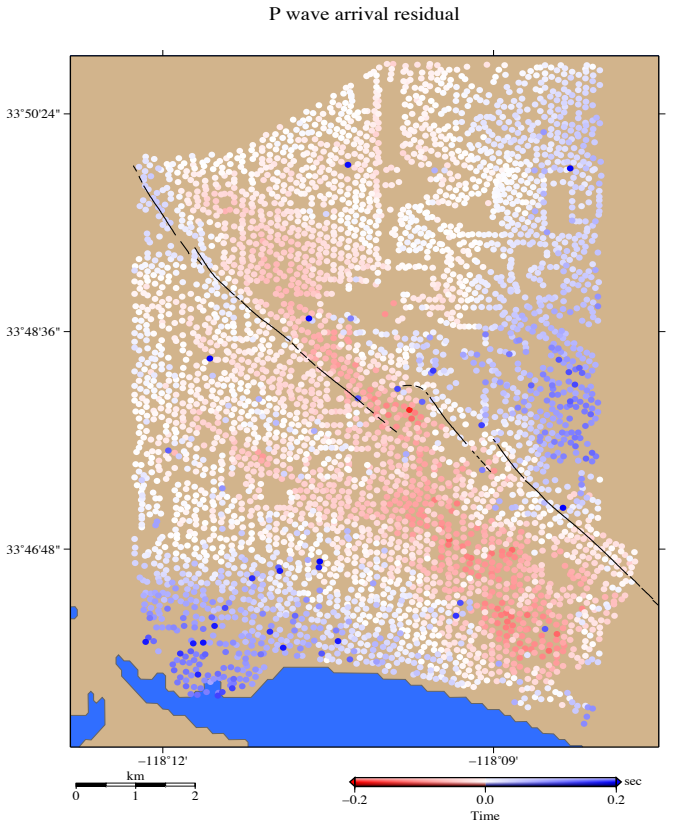

Figure 2.28.1. P-wave arrival time residual from the magnitude 2.4 earthquake. Red dots show the observed arrival time later than the preicted time, and the blue dots are the stations at which the observed p-wave arrival time is earlier than the predicted time. Black lines are the faults in this area.

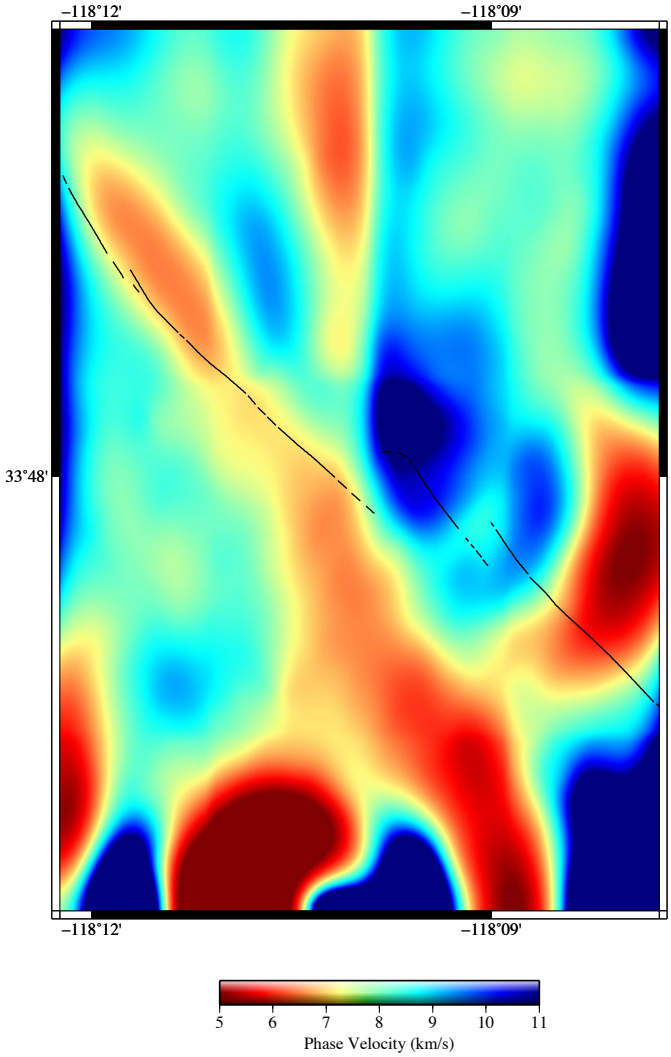

Figure 2.28.2. P wave phase velocity computed from the Helmholtz tomography. The red areas are slow velocities and the blue areas are fast velocities. The black lines are the faults in this area.

Acknowledgements

We thank Dan Hollis from NodalSeismic Company for providing the data for us to analyze. This project is funded by Deutsche Telekom and CITRIS. Patrick McEvoy, Markus Neubrand, Angela Nicoara, Louis Schreier, and Arno Puder from Deutsche Telekom provided the android phones and the myShake application.

References

Allen, R., Automatic earthquake recognition and timing from single traces: *Bulletin of the Seismological Society of America*, 68, 1521-1532, 1978.

Crotwell, H. P., T. J. Owens, and J. Ritsema, The TauP Toolkit: Flexible seismic travel-time and ray-path utilities, *Seismological Research Letters* 70, 154-160, 1999

Lin, F. C., Ritzwoller, M.H. & Snieder, R., Eikonal tomography: surface wave tomography by phase front tracking across a regional broadband seismic array, *Geophysical Journal International*, 177(3), 1091-1110, 2009.

Lin, F., and M. H. Ritzwoller, Helmholtz surface wave tomography for isotropic and azimuthally anisotropic structure, *Geophysical Journal International*, 186, 1104-1120, 2011a.

Magistrale, H., K. McLaughlin, and S. Day, A geology based 3-D velocity model of the Los Angeles basin sediments, *Bulletin Seismological Society of America* 86, 1161-1166, 1996.

Shearer, P., Introduction to Seismology, Cambridge University Press, Cambridge, 1999.

Wielandt, E., Propagation and structural interpretation of non-plane waves, *Geophys. J. Int.*, 113, 45-53, 1993.

29 ShakeAlert: A Unified EEW System for California

Margaret Hellweg, Richard Allen, Maren Böse (Caltech), John Clinton (ETH), Egill Hauksson (Caltech), Thomas Heaton (Caltech), Ivan Henson, Serdar Kuyuk, Doug Neuhauser, Ingrid Johanson, Ronni Grapenthin

Introduction

Earthquake Early Warning (EEW) is a method of rapidly identifying an earthquake in progress and transmitting alerts to nearby population centers before damaging ground shaking arrives. The first few seconds of the initial P-wave arrivals at one or more stations are used to detect the event, and predict magnitude and peak shaking. Detections from several stations are combined to locate the event. A warning of imminent shaking can be used to activate automatic safety measures, such as slowing trains, isolating sensitive equipment, or opening elevator doors. Warnings can also be sent directly to the public via cell phone, computer, television, or radio.

With support from the United States Geological Survey (USGS) and the Gordon and Betty Moore Foundation, the California Integrated Seismic Network (CISN) now moves into Phase III of the ShakeAlert project. This move transitions the focus from creating an end-to-end demonstration system for real time EEW solely in California, to developing a prototype for a West Coast EEW system. The University of Washington now joins the collaboration with the Berkeley Seismological Laboratory (BSL), the California Institute of Technology (Caltech), and the Swiss Institute of Technology Zürich (ETH). Phase III of the ShakeAlert development will provide a blueprint for future public alerts.

Project Status

The ShakeAlert system combines the best aspects of the three methods from the proof-of-concept project. Caltech's *OnSite* algorithm uses P-wave data from the single station nearest the epicenter to provide extremely rapid estimates of likely ground shaking. The BSL's ElarmS algorithm and ETH's Virtual Seismologist use data from several stations around an event epicenter to produce a slightly slower, but more reliable estimate of magnitude and location. Often, ElarmS is the first to send out an alert due to constant improvements to the algorithm made possible in part by Ivan Henson's system performance tools. Combining the three methods produces an algorithm, which has the speed of a single-station method, but is augmented by the confirmation and updated adjustments as additional station data become available.

When an identified event exceeds a defined combination of magnitude, ground shaking intensity, and statistical likelihood, information is broadcast to system users. Currently, during the demonstration and prototype phases, only project participants and a small cadre of beta users receive event information. Recipients include the state's emergency operations center at the California Office of Emergency Services (CalOES), Bay Area Rapid Transit (BART), Google, and the San Francisco Department of Emergency Management (SFDEM). A schematic diagram of the end-to-end system can be found at: http://www.cisn.org/eew/EEWProject.html.

ElarmS Development

The newest version of ElarmS (ElarmS2) began publishing alerts in March 2012 for the entire state of California. The improved algorithm in the new production-grade version of the code maximizes the performance, given the current seismic network configuration, and hardware and software capabilities, improving both the speed of the early warning processing and the accuracy of the result. ElarmS2 successfully detected 26 of the 29 earthquakes (M>3.5) across California and only issued two false alarms in a five-month period. Since April 2012 (for the BK network), and August 2012 (for the CI network), the stations are now equipped to send data in one-second packets to the waveform processing centers and be processed directly, shaving up to 6 seconds off of alert times. Event filters were also added to minimize the publication of false events. With all of these enhancements integrated, an alert can now be issued by ElarmS2 within 12.37 ± 5.21 sec of the origin time (see Figure 2.29.1). The tail in the alert time histogram is mainly caused by events offshore of Cape Mendocino and events located in poorly instrumented areas such as the northern and northeastern regions of California.

G-larmS Development

This year, the BSL has ramped up development of real-time GPS-based approaches to EEW through the use of displacement time series for rapid source parameter estimation. The G-larmS module uses data from GPS stations throughout Northern California to provide estimates of earthquake size and rupture length within seconds following a large (M>7) event. G-larmS is complementary to seismic EEW methods, providing precision for higher magnitude estimates where seismic methods tend to saturate and in turn relies on seismic data to provide event triggering. Preliminary testing of the offset determination module using simulated real-time GPS data from the 2010 M_W7.2 El Mayor-Cucapah earthquake found that the offset estimate stabilized quickly, even in the presence of earthquake shaking, and that the method provides results within 1-2 cm of the expected values. Work continues on the G-larmS module that will invert for fault slip and update magnitude estimates; it should be ready for operation by the end of this year.

Perspectives

This year we are continuing Phase III of the EEW project in collaboration with our partners at Caltech and the University of Washington, with funding from the USGS and the Moore Foundation. We look forward to continuing to maintain, operate, and improve the system as it transitions from a demonstration product to a working prototype. Phase III will highlight the increased importance of the EEW users and their interactions with the system.

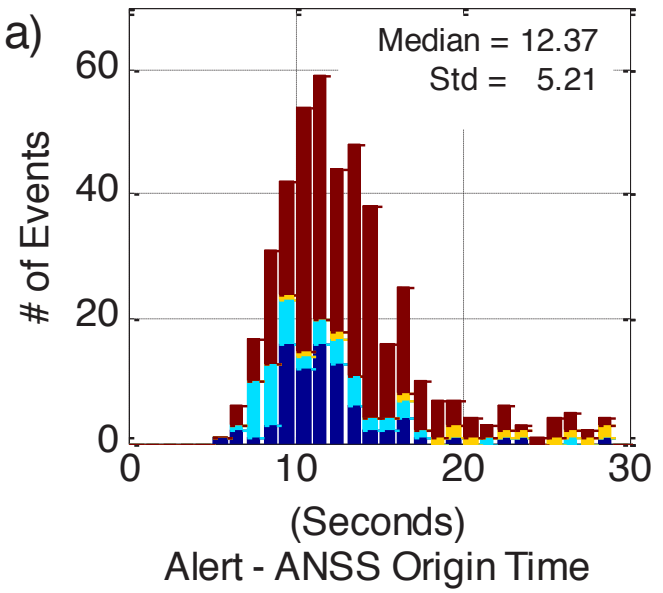

Figure 2.29.1: Latencies reflecting the difference in time between the first alert publication and the origin time of the earthquake in the Advanced National Seismic System (ANSS) catalog tallied for earthquakes detected by ElarmS2 from October 2, 2012 to February 15, 2013. The histogram is color coded by the epicenter's regional location: Bay Area (blue), LA Area (cyan), Offshore (yellow), and all others (red).

Acknowledgements

This project is supported at UC Berkeley by USGS Cooperative Agreement G12AC20348, at Caltech by Agreement G12AC20343, at USC/SCEC by Agreement G12AC20339, and at ETH Zurich by Agreement G12AC20342. Funding from the Gordon and Betty Moore Foundation is under project number GALA 3024.

30 Optimal Seismic Network Density for Earthquake Early Warning: A Case Study from California

H. Serdar Kuyuk and Richard M. Allen

Introduction

One of the challenges with Earthquake Early Warning Systems (EEWS) is minimizing the "blind zone"—the region around an earthquake epicenter where no warning is possible because the strong shaking has already occurred by the time the alert is generated. There are factors that influence the radius of the blind zone area that are simply out of our control. For example, we cannot dictate exactly where and when earthquakes occur and how far individuals are from the earthquake epicenter. However, there are many things we can do to reduce the size of the blind zone. For example, improvements can be made to increase the warning time by some seconds by: a) using the most advanced telecommunication technologies that can potentially decrease the current telemetry delay; b) decreasing data packet size to less than 0.5 seconds; c) improving event detection and alert filtering algorithms; and d) well developed seismic networks with improved station density deployed across seismogenic zones. The degree to which these improvements can be made depends on how close the seismic stations are to the earthquake epicenter, as well as the distance between the warning site and the earthquake epicenter, the depth of earthquake, the density of the seismic network, the telemetry delay, and the time needed for decision making in regards to the type of warning that should be issued. For any practical use, the blind zones will be larger depending on the time required for a specific action.

We estimate how the average blind zone radius changes with varying interstation distances by examining inter-station distances from 1 km to 100 km (Figure 2.30.1). In our calculations, we first model typical California earthquakes, which, on average, have a relatively shallow depth of 8 km. We find that by increasing the station density 10 times (interstation distances from 100 to 31 km), the radius of the blind zone decreases by 57% from 73 km to 32 km. Increasing mesh density an additional 10 times (interstation distances from 31 to 10 km), the blind zone radius drops by another 37% from 32 km to 20 km. Increasing the station density by another factor of 10 (interstation distances from 10 to 3 km) reduces the radius by only 15% from 20 km to 17 km. We can also compute these estimates for the spatial extent of the blind zone area. A decrease of 57%, 37%, and 15% in blind zone radius corresponds to an 80%, 60% and 28% drop respectively in total blind zone area

We explored the distribution of interstation distances within the California Integrated Seismic Network (CISN). At each of the California stations we assign an average interstation distance value, which is computed from the average distance to the three closest stations. From these values we create a contour map of interstation distances using a linear interpolation between stations (Figure 2.30.2a).

We find that ~50% of California have an average interstation distance of 50 km or more (Figure 2.30.2a, primarily yellow

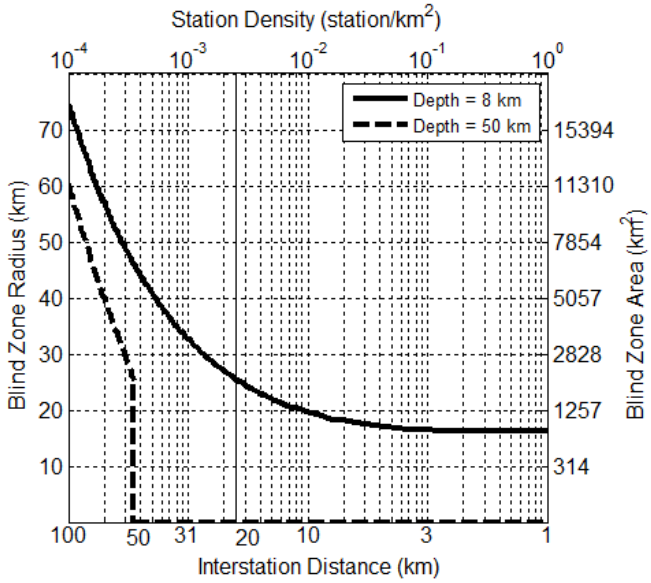

Figure 2.30.1: Relationship between network density (or, equivalently interstation distance) and blind zone radius (or, equivalently area) computed for earthquakes of different depths. The smaller 8 km depth (solid line) is consistent with the average depth of earthquakes in California and the larger 50 km depth (dashed line) is consistent with what might be expected beneath the on-shore regions of the Pacific Northwest of the US from a subduction zone earthquake.

regions), whereas highly populated areas, such as the San Francisco Bay and the Los Angles regions have less than 30 km spacing (Figure 2.30.2a, green colors).

An EEWS should be devised to be the most robust at issuing alerts in regions identified as having high shaking potential from earthquakes, in combination with a large population base from the standpoint of probabilistic seismic hazard. For California, we assess which regions have both a high shaking potential (Figure 2.30.2b) and a large population density (Figure 2.30.2c). The seismic networks have been designed to have higher station densities in the regions of higher population. Qualitatively, regions that have both large populations as well as a high likelihood of experiencing strong shaking include: the extended Los Angeles and San Francisco Bay regions, and the southern part of the San Andreas Fault.

For the southern part of the Central San Andreas Fault (SAF), between San Jose and Los Angeles, we find there are an inadequate number of stations. In this critical part of California, the interstation distance varies from 30 to 50 km

Based on quantitative estimates of the current CISN/EEWS infrastructure, we conclude that the blind zone radius throughout California is very heterogeneous. The minimum blind zone radius is ~16 km for typical California earthquakes with 8 km depth when a system requires at least four station detections

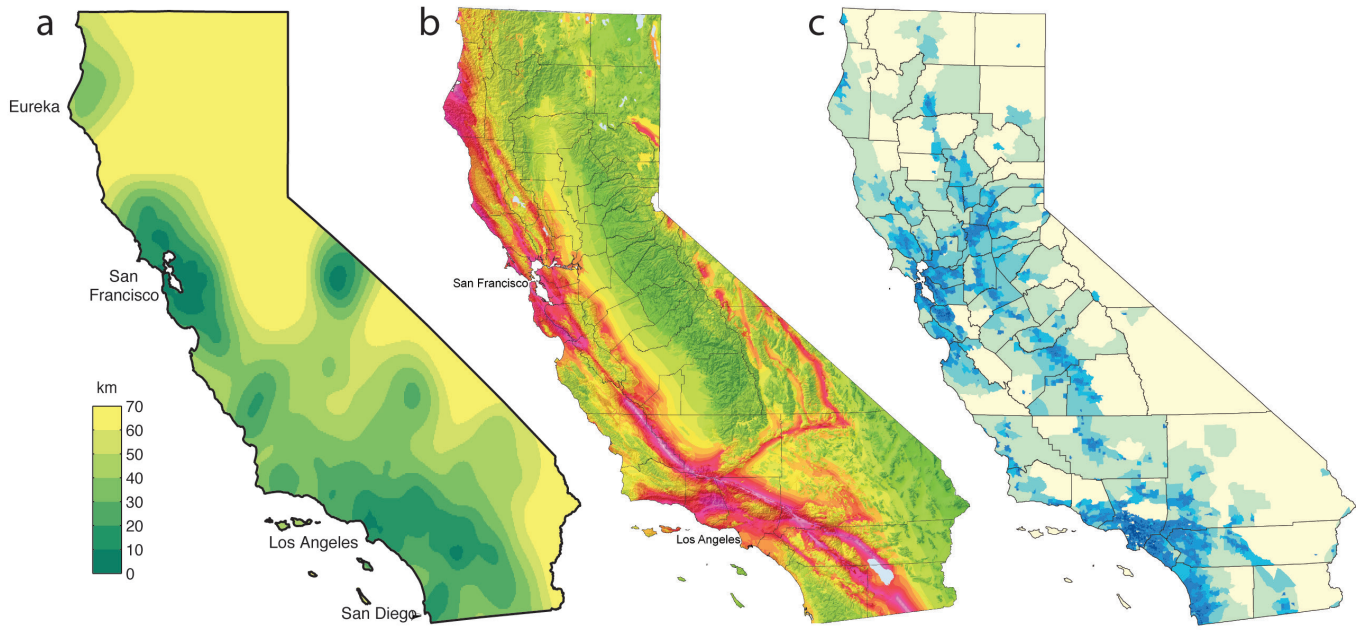

Figure 2.30.2: a) Seismic station interstation density map where yellow colors indicate lower densities. For a given station location, the interstation density is determined by averaging the distance to the nearest 3 stations, b) Probabilistic seismic hazard map (from the State of California), c) Population density of California (from the U.S. Census Bureau). For larger resolution images see the References section that has the appropriate links.

and there is a four second processing/communications delay. Therefore, based on current constraints, there will be no time to issue a warning for any location within 16 km of a large earthquake. This limit of 16 km could be decreased if we address technical and algorithmic issues such as reducing the telemetry delay, decision-making time, etc.

The blind zone radius increases with larger interstation distance. Throughout most of the greater San Francisco Bay area and the Los Angeles area, blind zone radius is less than 30 km. These regions would likely get warnings for earthquakes that occur at distances greater than 20 km. In other regions of California, particularly in Northern California where the station spacing is much sparser (*e.g.*, interstation distances of > 70 km), the blind zone radius is much larger. Our results show that successful warnings could only be issued for earthquakes at distances of 50 km from the earthquake location.

Three key factors which affect the optimization of interstation distance and station distribution are: I) budget, II) population/property distribution, and III) probability of expected earthquakes (past seismicity/known faults). In our budget-limited reality, however, optimum performance is also not achieved by even station distribution. Stations should be (1) densest (~10 km) in the urban areas that are above hazardous faults, (2) fairly dense (~20 km) along hazardous faults away from urban centers, and (3) least dense in other regions. Based on the current distribution of stations and hazards in California, the areas between San Jose and northern LA, and between Eureka and the San Francisco Bay Area need immediate attention if we would like to enhance EEWS in California.

Acknowledgements

This work is funded by USGS/NEHRP awards G09AC00259 and G12AC20348, and by the Gordon and Betty Moore Foundation through Grant GBMF3024 to UC Berkeley.

References

Kuyuk H.S., Allen, R.M., Optimal seismic network density for earthquake early warning: A case study from California, *Seismological Research Letters*, in press, 2013.

State of California, Department of Conservation, Regional Geologic Hazards and Mapping Program, Probabilistic seismic hazard map (http://www.consrv.ca.gov/cgs/rghm/psha/Pages/Index.aspx last accessed 02 March 2013)

U.S. Census Bureau, U.S. Department of Commerce, Economics and Statistics Administration. (http://www2.census.gov/geo/maps/dc10_thematic/2010_Profile/2010_Profile_Map_California.pdf)

31 Designing a Network-Based Earthquake Early Warning System for California: ElarmS–2

H. Serdar Kuyuk, Richard M. Allen, Ivan Henson, Holly Brown, Margaret Hellweg, and Douglas Neuhauser

Introduction

The California Integrated Seismic Network (CISN), funded by the USGS, is developing an Earthquake Early Warning (EEW) system for California. Within this "California ShakeAlert" project, three algorithms are being tested, one of which is the network based Earthquake Alarm Systems (ElarmS) EEW. Over the last 3 years, the ElarmS algorithms have undergone a large-scale reassessment and have been re-coded to solve technical and methodological challenges. The improved algorithms in the new production-grade version of the code (E2) maximize the current seismic network's configuration, hardware, and software performance capabilities improving both the speed of the early warning processing and the accuracy of the result. E2 is designed as a modular code and consists of a new event monitor module with an improved associator that allows more rapid association with fewer triggers, while also adding several new alert filter checks that help minimize false alarms.

Performance of E2

The performance statistics we present here are for the online real-time E2 system, versions E2.3.1 and E2.3.2, which have been running in real-time since October 2, 2012 (Figure 2.31.1.). The changes made in E2.3.2 only affect the performance speed, so we are maximizing the time window and number of events by considering performance for both versions. We find that E2 detected 26 of the 29 Advanced National Seismic System (ANSS) earthquakes which had $M_{ANSS} \geq 3.5$. We also investigate the performance in the most populated and the most instrumented regions of the state, the San Francisco Bay Area and the Los Angeles region and find that in these regions, all events were detected and there was only one false event. E2 also successfully detected most earthquakes just outside the CISN networks, including offshore of Cape Mendocino in Northern California and south of the California/Mexico border. However, the estimates for earthquakes that are at the edge or outside of our network have larger errors than is typical of detections within the network footprint.

E2 issued five false alert messages, none of which were in the highly populated San Francisco Bay Area or Los Angeles region. Instead, these false alerts were caused by events outside of California. One event was the M_w 6.3 earthquake off the west coast of Baja, California on December 14, 2012. This was more than 300 km from the network, yet triggered many Southern California stations. These triggers were associated into four simultaneous separate/split events because the offshore event had a poor initial estimate of location (false events 1a, b, c, d in Figure 2.31.1). The other false event was from a M_w 5.1 earthquake 72 km west of Tonopah, Nevada on December 13, 2012. The closest station to this Nevada event was 80 km away, resulting in a significant initial mislocation. The E2 system did adequately

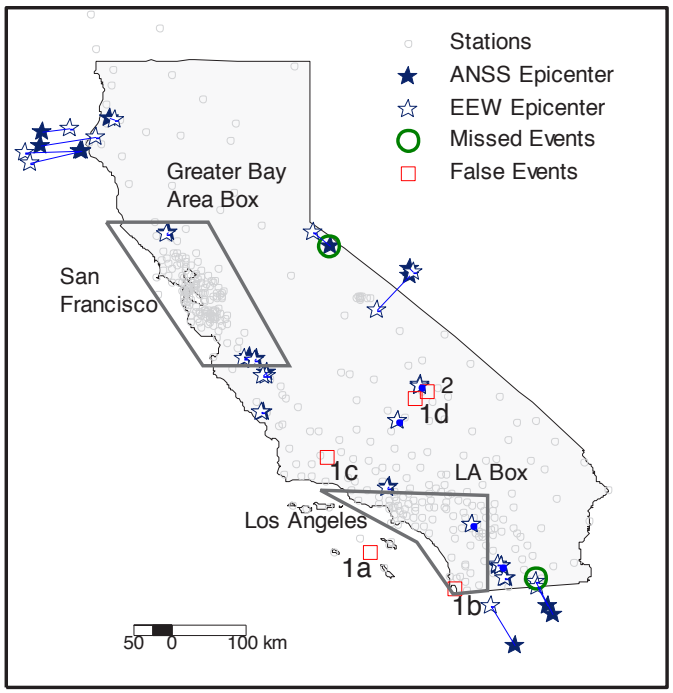

Figure 2.31.1: All detected California events (29), false events (squares, 2), and missed events (circles, 3) with $M_{ANSS} \geq 3.5$ that occurred between October 2, 2012 and February 15, 2013. ANSS epicenters (filled stars) and the corresponding E2 epicenters (open stars) are connected with a line.

locate this earthquake in later iterations; however, later station triggers also
generated another event (false alert 2 in Figure 2.31.1).

The differences between ANSS and E2 source parameters are calculated for $M_{ANSS} \geq 3.5$ and $M_{ANSS} \geq 3.0$ events. We compute errors in earthquake magnitude, origin time and location by subtracting the E2 results from ANSS results (Figure 2.31.2). For $M_{ANSS} \geq 3.0$ events we find the median magnitude error is -0.05 ± 0.39, where the negative -0.05 value indicates that on average E2 slightly overestimates the magnitude by 0.05 magnitude units. For only the larger events ($M_{ANSS} \geq 3.5$) the error is 0.09 ± 0.46.

Errors in origin time and location are both strongly influenced by the location algorithm. The origin time errors are not normally distributed, instead the mean and standard deviations of the origin time errors are -0.29 ± 1.16 for M>3 and -0.10 ± 1.59 for M>3.5. The median error in the epicentral location (*i.e.,* distance between true and estimated epicenters) of E2 is 3.78 km. The median location error decreases to 2.01 km for larger events (M>3.5).

On Nov/Dec 2012, we made some small changes to the waveform processor that makes E2 a little faster:

-No longer process the data aligned on second boundaries. Simply process packets as soon as they arrive.

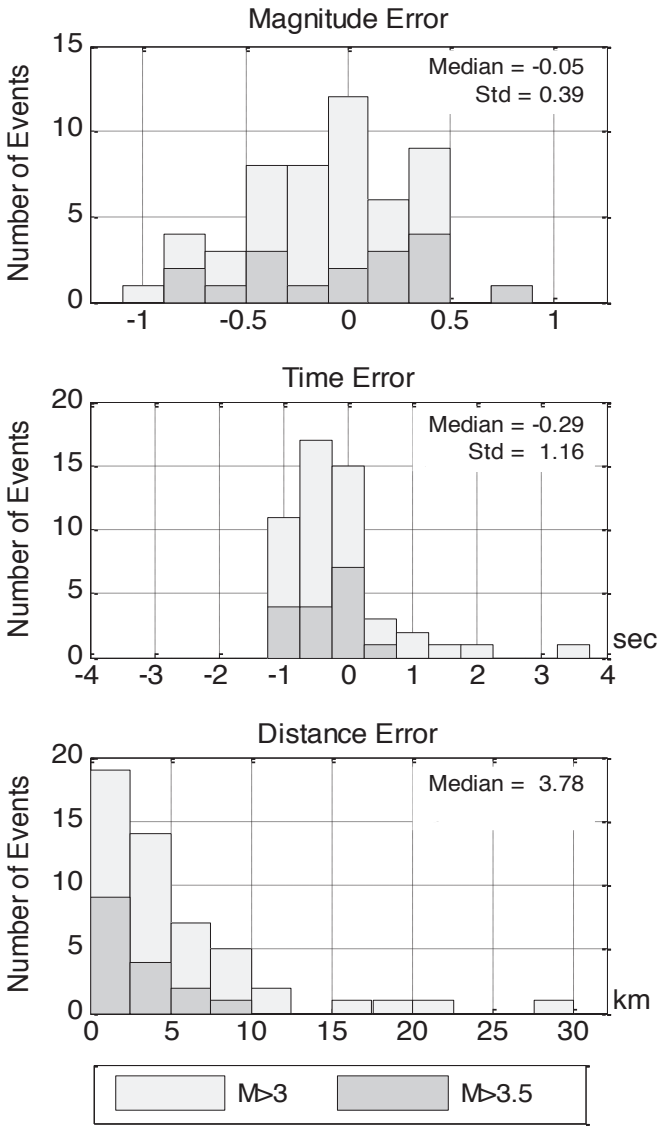

Figure 2.31.2: Histograms of magnitude, time and location errors for E2. The lighter histograms are errors for all events with M_{ANSS}≥3.0 and darker histograms are for events with M_{ANSS}≥3.5.

-No longer wait for a half second before sending a trigger (this was to compute τ_p^{max}). Now send triggers immediately.

-Reduce trigger buffer from 0.5 to 0.05.

These changes probably decreased trigger latencies by 1.0 to 1.5 seconds on average.

In June 2013, the speed of the E2 location algorithm was improved by using four processing threads to do the grid search, instead of one. This makes E2 about three times faster for offline processing. The online performance from October 2, 2012 to February 15, 2013 shows, on average, E2 currently issues an alert 8.68 ± 3.73 s after the first P-wave detection for all events across California. This processing latency, is calculated by the alert time minus the time of the first P-wave arrival at the closest stations (Figure 2.31.3). Currently, E2 processing latency is the smallest in the Los Angeles Area with a median of 6.72±3.96

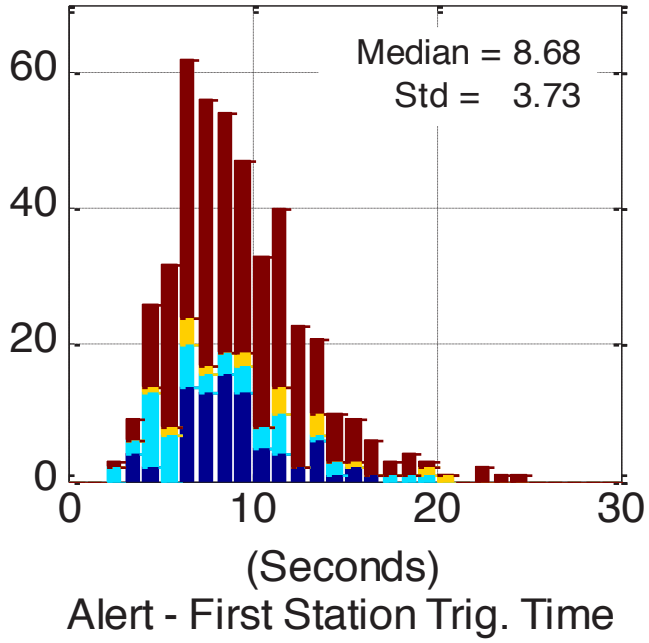

Figure 2.31.3: E2 processing latency, which is alert time minus the time of the first P-wave arrival at a seismic station. This shows the total time the network and E2 require to issue an alert for an event. The median is 8.68 ±3.73 seconds. Alerts are faster for the San Francisco Bay (blue) and Los Angeles area (cyan).

seconds, which is almost two seconds faster than the latency in the San Francisco Bay Area. This is due to the additional delays from NC stations, which make up a large fraction of the stations in Northern California.

Acknowledgements

This project is possible thanks to the collaborative efforts of many people working at the CISN operating institutions: UC Berkeley, Caltech, USGS Menlo Park and USGS Pasadena. This work is funded by USGS/NEHRP awards G09AC00259 and G12AC20348, and by the Gordon and Betty Moore Foundation through Grant GBMF3024 to UC Berkeley.

References

Allen, R.M., Seconds before the big one, *Scientific American*, 2011.

Brown, H., Allen, R.M., Hellweg, M., Khainovski, O., Neuhauser, D., Souf, A., Development of the ElarmS methodology for earthquake early warning: Realtime application in California and offline testing in Japan, *Soil Dynamics and Earthquake Engineering*, 31, 188-200, 2011.

Kuyuk H.S., Allen, R.M., Brown, H., Hellweg, M., Henson, I., and Neuhauser, D., Designing a network-based earthquake early warning system for California: ElarmS-2, *Bull. Seismol. Soc. Am,* accepted, 2013.

32 G-larmS—Integrating Real-Time GPS into Earthquake Early Warning I: Implementation

Ronni Grapenthin, Ingrid Johanson, Richard Allen

Introduction

In an effort to improve earthquake parameter estimation in Earthquake Early Warning (EEW) for large earthquakes (such as moment magnitude and finite fault geometry), the BSL is working to integrate information from real-time GPS, and now generates and archives real-time position estimates using data from 62 GPS stations in the greater San Francisco Bay Area. This includes 26 stations that are operated by the BSL as part of the Bay Area Regional Deformation (BARD) network, 8 that are operated by the USGS, and 29 stations operated by the Plate Boundary Observatory (PBO).

Data from these sites are processed in a fully triangulated network scheme in which neighboring station pairs are processed with the software TrackRT *(Herring et al.,* 2010*)*. Positioning time series are produced operationally for 172 station pairs (Figure 2.32.1); additional station pairs will be added as more real-time stations become available.

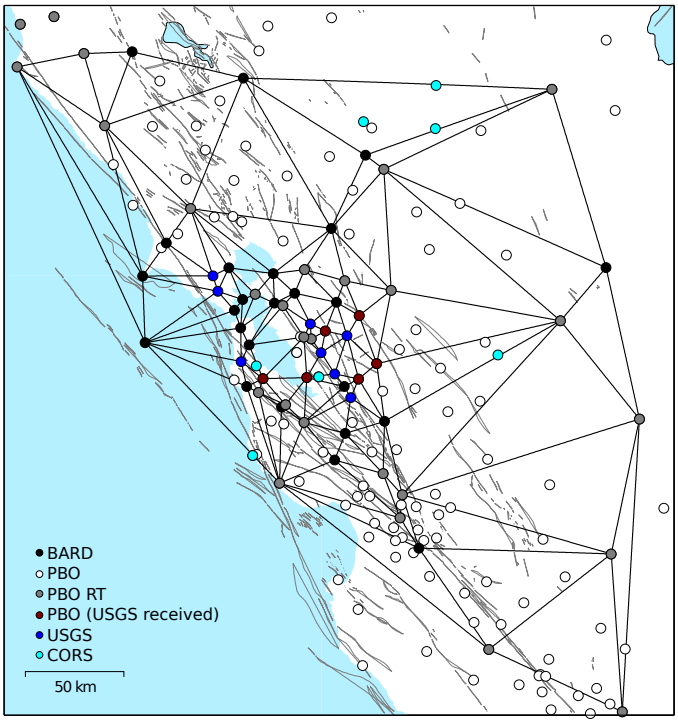

Figure 2.32.1: Map of the greater San Francisco Bay Area with high-rate GPS stations. Lines connecting the stations indicate station pairs (172) we use in the processing. White circles are non real-time PBO stations.

G-larmS, the geodetic alarm system, sits on top of real-time GPS processors such as TrackRT and analyzes real-time positioning time series, determines and broadcasts static offsets from these, and will ultimately derive fault and magnitude information (not fully implemented). This prototype Python implementation is tightly integrated into seismic alarm systems as it uses their P-wave detection alarms to trigger its processing.

Architecture and Data Processing

The G-larmS architecture and process flow are depicted in Figure 2.32.2. Most notably, G-larmS consists of two independent modules for offset estimation and earthquake parameter estimation. Within these, the actual methods to get the respective values are easily exchangeable and could be easily exported to other agencies in other geographic regions.

A list of 172 station pairs (baselines) forms the basis of the Bay Area network. Each of these baselines is processed by an individual TrackRT process to generate position time series. For event response and quality assessment, we consider the most recent 10 minutes of data. Multipath and other noise treatment will be implemented in the future. We categorize time series as 'good' or 'bad' based on a few metrics such as standard deviation over the 10 minute time window. These quality parameters are passed along with the derived offsets.

The GPS system listens to CISN ShakeAlert *(Hellweg et. al.,* 2013*)* to get earthquake alarms. Once the seismic system is triggered, we estimate and publish the offset evolution for a subset of baselines (see below). In parallel, the parameter estimator prepares to ingest these offsets to invert them for rupture length and magnitude.

Offset Estimation

Offset estimation is triggered by the seismic system, which broadcasts messages containing location, and preliminary magnitude information. The magnitude estimate is used to determine a cut-off radius around the alerted epicenter. This defines an area for which we expect static offsets. We limit our analysis to the stations in this region to manage computing resources.

To estimate co-seismic offsets from the east, north, and vertical component of each baseline time series, we implement the following algorithm:

1. Determine pre-event position by averaging time series over 10 minute time window.

2. Estimate S-wave arrival (shaking and static offset arrive).

3. Average each new datum after predicted S-wave arrival to determine post-event position.

4. Update static offset by subtracting average pre-event position from average post-event position.

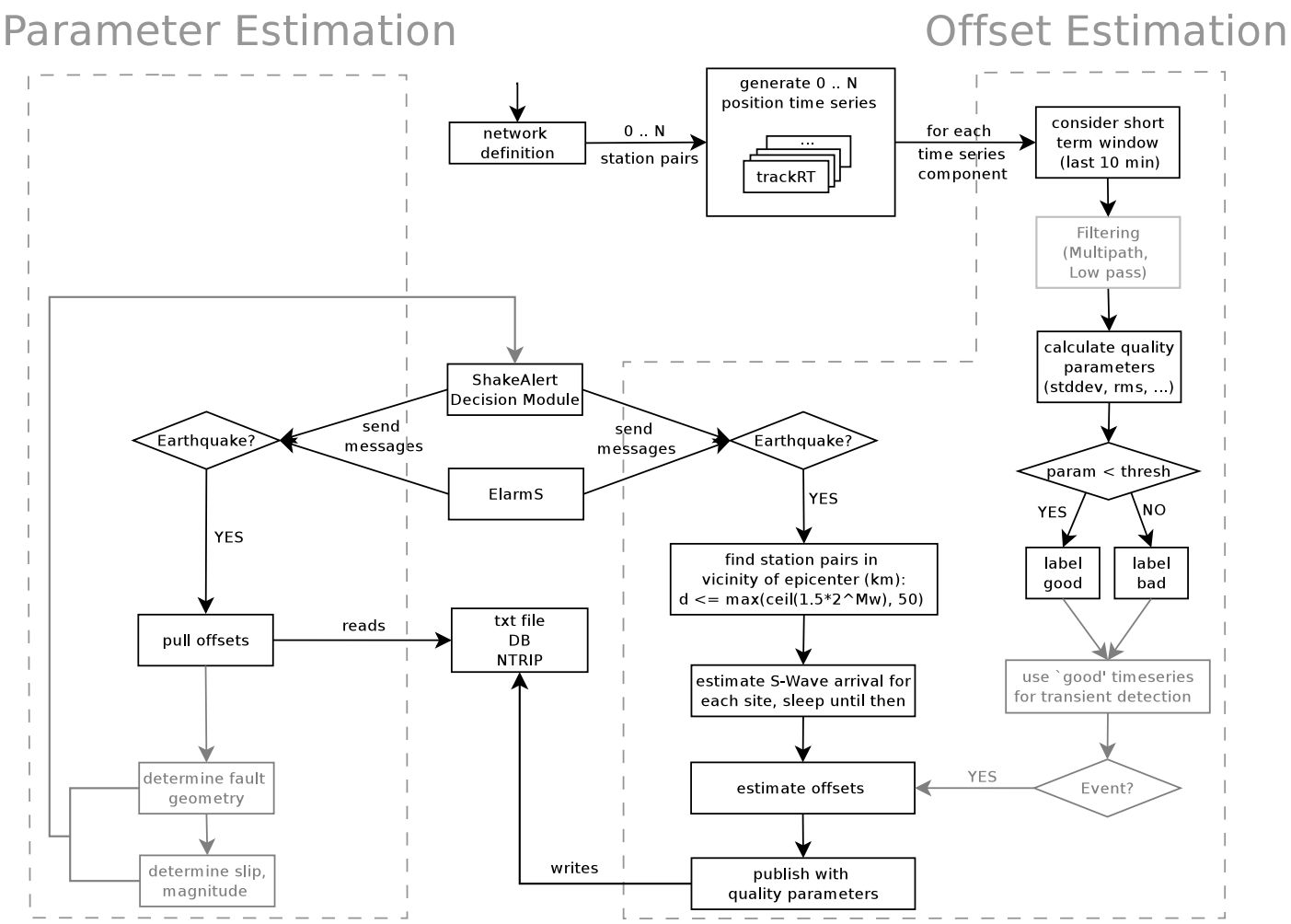

Figure 2.32.2: G-larmS flowchart showing its two independent components for offset and parameter estimation. The light gray boxes indicate planned but not yet implemented components.

Outlook

The plan for the near future includes the finalization of the earthquake parameter estimation module (similar to *Colombelli et al.,* 2013*)* and the implementation of a mechanism to broadcast the results. Once this is in place, G-larmS will be run in test-mode for careful performance evaluation.

In the mid to long term we intend to include sidereal filtering and other methods to eliminate noise in the time series, which will improve the detection limits and likely enable autonomous transient detection. The latter would turn G-larmS into a valuable asset in volcanic environments.

Acknowledgements

This work is supported through the Gordon and Betty Moore Foundation, and CISN partners. We use real time data services provided by the Plate Boundary Observatory operated by UNAVCO for EarthScope (www.earthscope.org) and supported by the National Science Foundation (grants no. EAR-0350028 and EAR-0732947).

References

Colombelli, S., et al., Application of real-time GPS to earthquake early warning in subduction and strike-slip environments, *J. Geophys. Res. Solid Earth*, 118, doi:10.1002/jgrb.50242, 2013.

Herring, R. T. A. et al., GAMIT/GLOBK Reference Manuals, Release 10.4 (*MIT Technical Reports*), 2010.

Hellweg, M. et al., Operating and Improving Earthquake Early Warning for Northern California and the US West Coast, SSA Annual Meeting, 2013.

33 G-larmS—Integrating Real-Time GPS into Earthquake Early Warning II: Testing

Ronni Grapenthin, Ingrid Johanson, Richard Allen

Introduction

Testing the results of real-time GPS for Earthquake Early Warning (EEW) under realistic conditions, and for scenarios that are relevant to the San Francisco Bay Area's tectonic environment, is a major step toward having our work accepted for integration with an operational EEW system. While Northern California has many small earthquakes (*i.e.*, M_w<4) that are used to validate the seismic system, it is only for very large earthquakes (M_w >6.5) that real-time GPS is expected to provide a significant contribution. This is because for larger events, seismic systems need additional information to correctly estimate magnitude and finite fault extent, and because real-time GPS suffers from a lower signal-to-noise ratio than post-processed data.

Here, we follow two strategies to test G-larmS (see Research section 2.32): (1) add simulated static offsets to real-time time series, and (2) replay archived data that contain static and dynamic motion due to a real event. We test the prototype system for the Bay Area using synthetic data for a M_w 6.9 Hayward Fault Scenario and with data for the 2010 M_w 7.2 El Mayor-Cucapah earthquake. Because the earthquake parameter module is in development, tests are limited to offset estimation.

To facilitate testing of the full software stack, we include 3 options in G-larmS: (1) a replay of archived data, (2) adding simulated offsets to replayed or real-time data, and (3) simulate the receipt of CISN ShakeAlert messages, *i.e.* an earthquake alarm.

M_w 6.9 Hayward Fault Scenario

Due to the accumulated slip deficit since the last large earthquakes along the Hayward-Rodgers Creek fault zone, its earthquake probability is the highest of any fault in the San Francisco Bay Area *(e.g., Bürgmann et al., 2000)*. We use this region to test G-larmS' ability to recover static offsets from time series because this is where our network is the densest.

We use Okada's (1985) equations to simulate static offsets (Figure 2.33.1) due to 1 m of slip along the entire Hayward Fault (M_w 6.9) and convert the absolute offsets into offsets along baselines (see Figure 2.32.1). Using G-larmS' replay mode, these relative offsets are added to archived real-time positioning time series after the simulator in G-larmS generates a CISN ShakeAlert alarm. This contains time and location information for the theoretical earthquake. G-larmS estimates the expected S-wave arrival time for each baseline at which the simulated offsets are added to the respective time series. The offset estimation algorithm is triggered in the same way as for a real event. We repeat this offset recovery experiment 224 times and recover offsets close to the simulated values within the variation of real-time noise (±1-2 cm, Figure 2.33.2), which gives us confidence that the algorithms work as expected.

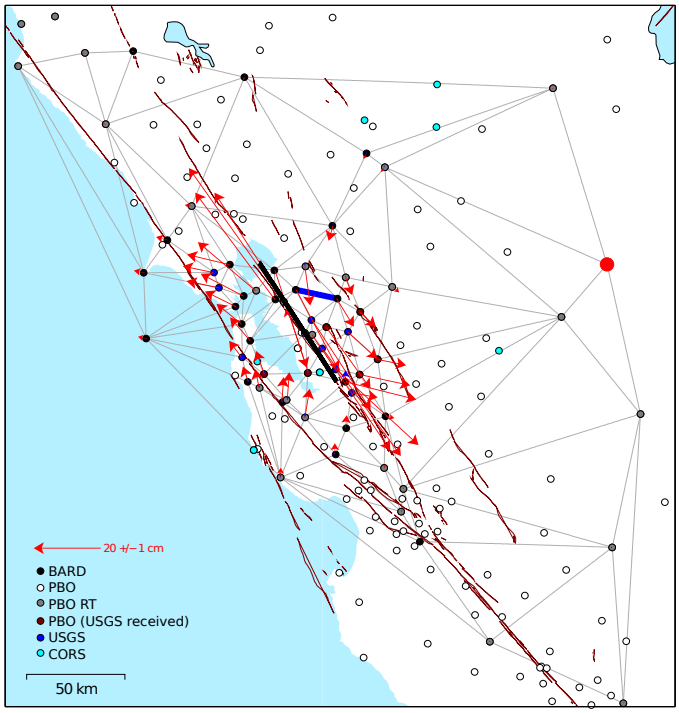

Figure 2.33.1: Simulated co-seismic offsets due to a Hayward Fault scenario of 1 m of slip along the entire fault (the black line is the fault model). The displacements are given with respect to station CMBB (red circle). The blue line marks baseline DIAB-BRIB for which we show the offset evolution below.

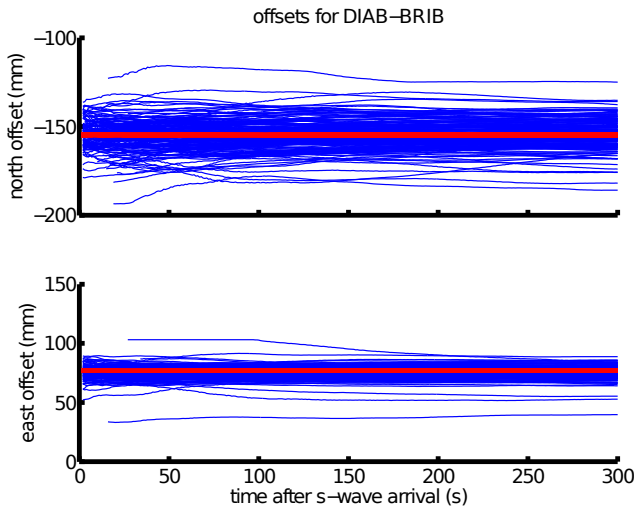

Figure 2.33.2: Time series of offset recovery (blue lines) after adding simulated offsets to archived real-time time series along baseline DIAB-BRIB (see Figure 2.33.1). Time series are with respect to expected S-wave arrival time, though the simulated offsets do not contain any dynamic deformation. The red lines show the simulated offset. 224 offset time series based on randomly selected data between Nov 2012 and Apr 2013. The spread of the results is within data variance; no 'bad' time series have been removed for this experiment.

2010 M_w 7.2 El Mayor-Cucapah

The M_w 7.2 El Mayor-Cucapah earthquake (e.g., *Hauksson et al.,* 2011) occurred on April 04, 2010 at 22:40:47 UTC (USGS) south of the US border in Mexico. This event was well sampled by a dense network of high-rate GPS sites (Figure 2.33.3). We process these data (obtained from SOPAC), which contain static offsets and dynamic motion due to surface waves, with Track-RTr (*Herring et al.,* 2010) and predicted IGS orbits to simulate a real time situation. The resulting time series are analyzed in G-larmS' replay mode. We generate a CISN ShakeAlert message with the final USGS parameters for origin time, location and magnitude for the event. This triggers the offset estimation for the network as detailed above.

Figure 2.33.4 shows the evolution of co-seismic offset estimates along the two blue baselines in Figure 2.33.3 and provides a comparison to the final co-seismic offset estimates from SOPAC (red line). While the dynamic motion impacts these sites to some degree, the results converge quickly to the co-seismic offsets.

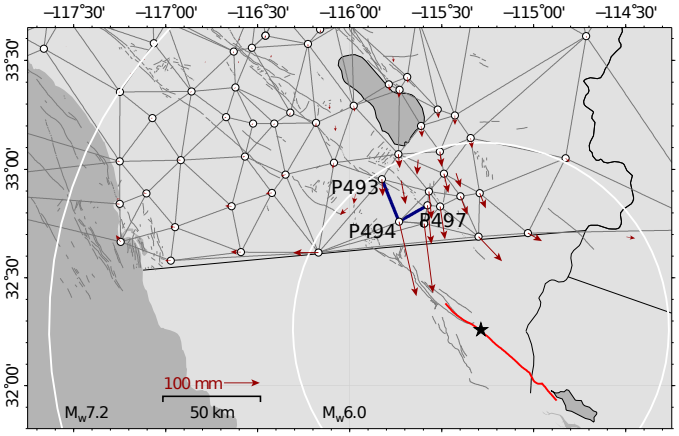

Figure 2.33.3: Subset of baselines used for the El Mayor-Cucapah earthquake. Arrows show absolute offsets, the star marks the epicenter. White circles mark G-larmS' threshold radius for M_w 6.0 and 7.2. The blue lines mark baselines P493-P494, and P494-P497 for which we show offsets in Figure 2.33.4.

Conclusions and Outlook

The tests suggest that G-larmS' offset estimation is implemented correctly and the strategy recovers quickly from dynamic motion due to S-waves. The impact of these results on magnitude estimation will have to be tested in the future. Other future work will include the use of more realistic static offset estimations for the Hayward fault *(provided courtesy Brad Aagaard,* USGS) and investigate the timing of GPS contributions to earthquake early warning in the Bay Area.

Acknowledgements

This work is supported through the Gordon and Betty Moore Foundation, and CISN partners. We use data provided by the Plate Boundary Observatory operated by UNAVCO for EarthScope and supported by the NSF (grants no. EAR-0350028 and EAR-0732947).

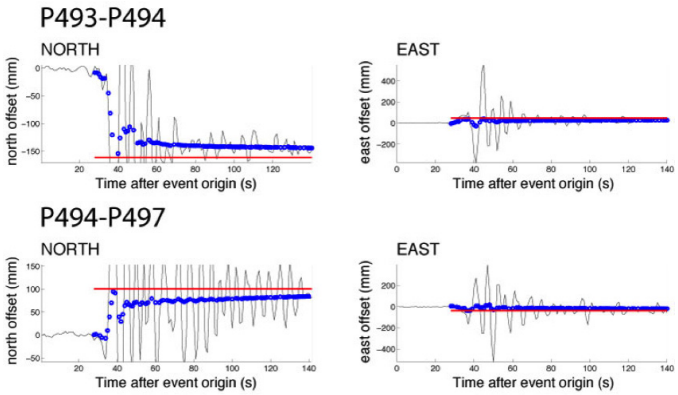

Figure 2.33.4: Offset time series (blue) estimated from displacements (black) shown with respect to event origin time for baselines P493-P494 and P494-P497 (Figure 2.33.3). Red lines are the final co-seismic offset derived from GPS solutions provided by SOPAC. Our results quickly converge to the final solutions even through the dynamic motion.

References

Bürgmann, R. et al., Earthquake Potential Along the Northern Hayward Fault, California, *Science* 289, 1178, DOI: 10.1126/science.289.5482.1178, 2000.

Hauksson, E. et al., The 2010 M_w 7.2 El Mayor-Cucapah earthquake sequence, Baja California, Mexico and southernmost California, USA: Active seismotectonics along the Mexican Pacific margin, *Pure Appl. Geophys.*, doi:10.1007/s00024-010-0209-7, 2011.

Herring, R. T. A. et al., GAMIT/GLOBK Reference Manuals, Release 10.4 (*MIT Technical Reports*), 2010.

Okada, Y., Surface Deformation due to Shear and Tensile Faults in a Half-Space, *BSSA* 75(4), pp 1135-1154, 1985.

34 Application of Seismic Array Processing to Earthquake Early Warning

Lingsen Meng, Richard Allen

Introduction

Earthquake early warning (EEW) systems are essential in mitigating seismic hazard by issuing warnings prior to the arrival of strong ground shaking during an earthquake. Many of the currently operating EEW systems work on the basis of magnitude-amplitude/frequency scaling for a point source, which is invalid for magnitude estimation of M >7.5 earthquakes. This issue is particularly highlighted in EEW performance of the M9.0 Tohoku-Oki earthquake (*Hoshiba et al,* 2011). Failing to take into account the finite rupture propagation, the magnitude estimated by the Japanese EEW system saturated at M8.1. The Japanese Meteorological Agency (JMA) issued warnings of strong seismic intensity only for the Tohoku region. However, the Kanto region experienced much larger ground motions than that predicted by JMA. The example of the Tohoku-Oki earthquake demonstrates the need for characterizing the finite fault dimension in real time for EEW systems of large earthquakes to be successful.

Among the ongoing efforts to determine the finite fault extent in real time, GPS approaches provide more reliable static displacements and thus, magnitude, than do seismic methods (*Colombelli et al,* 2013). The FinDer approach is also proposed to determine linear fault geometry based on the amplitude difference in near/far field seismic waveform, provided dense station coverage.

Alternatively, we explore the concept of imaging the rupture process of large earthquakes in real time using clusters of dense seismic arrays located near an active fault. Back tracing the waveforms of earthquakes recorded by such arrays allows the estimation of the rupture directivity, size, duration, speed, and segmentation, which enables the EEW of M>6 earthquakes. The principle is analogous to the location and tracking of moving sources by antennas in a variety of military and civilian applications. Figure 2.34.1 illustrates the concept of seismic array processing for EEW. Strong, high-frequency (HF) seismic waves usually radiate from the rupture front. Tracking the source of the HF seismic waves during large earthquakes recovers the movement of the rupture front. The trajectory of the rupture front marks the fault extent involved in the earthquake.

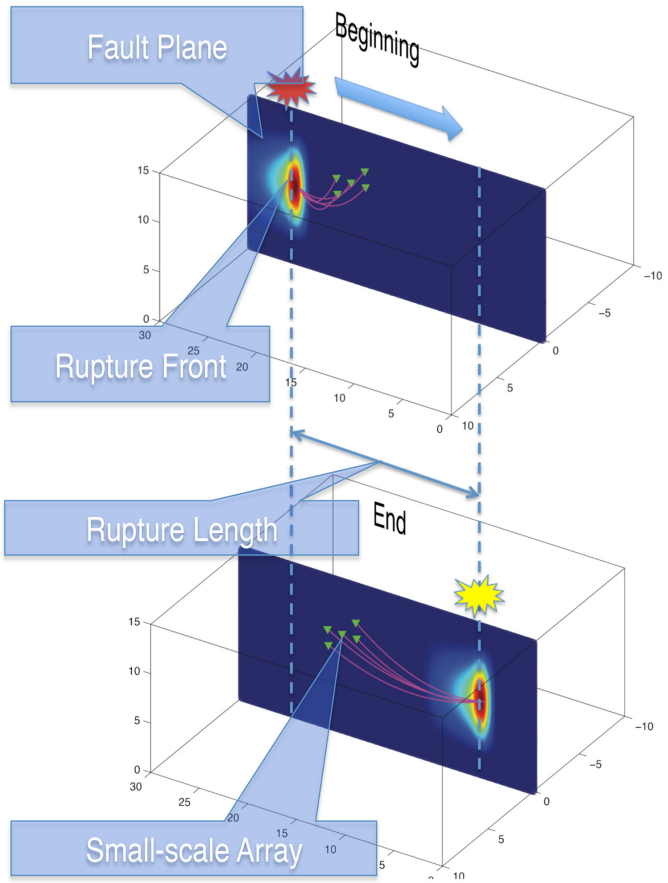

Figure 2.34.1: 3D schematic of imaging seismic rupture with a small scale array. The color contours mark the rupture front with high slip velocity. The red and yellow "bang" symbols represent surface projections of the rupture front. The green triangles are the stations. The pink curve is the ray path of the incoming seismic waves. The dashed lines mark the spatial extent of the rupture.

Method

The direction of the incoming HF waves can be determined by analyzing the phase of coherent seismic signals across an array with various array-processing techniques. For small-scale arrays, the impinging wave front can be approximated as a plane wave. The back azimuth of the plane wave is then projected onto an assumed fault plane to resolve the location of the rupture front. Here, we adopt the correlation stacking technique to perform the array analysis. The correlation stacking beamformes the normalized cross-correlation coefficients instead of the waveforms to improve robustness against scattering and multi-pathing in the shallow crustal environment (*Fletcher et al.*, 2006). The stacked correlation cc_{ij} can be calculated by :

$$cc_{ij} = \left[\frac{\sum_t x_i(t) x_j(t - \tau_{ij})}{\sum_t x_i^2 \sum_t x_j^2} \right]^{1/2}$$

where i, j are station indices, x_i is the seismic signal recorded at the ith station, t is the time, τ_{ij} is the timing delay of a testing wave direction between the station i and j.

The 2004 Parkfield Earthquake

We implemented the proposed methodology to the 2004 M6 Parkfield earthquake in a simulated real-time environment. The earthquake is one of the few big events (M >6) that are recorded by a local small-scale seismic array (UPSAR array). *Fletcher et al*, 2006 shows that the rupture kinematics can be retrieved by

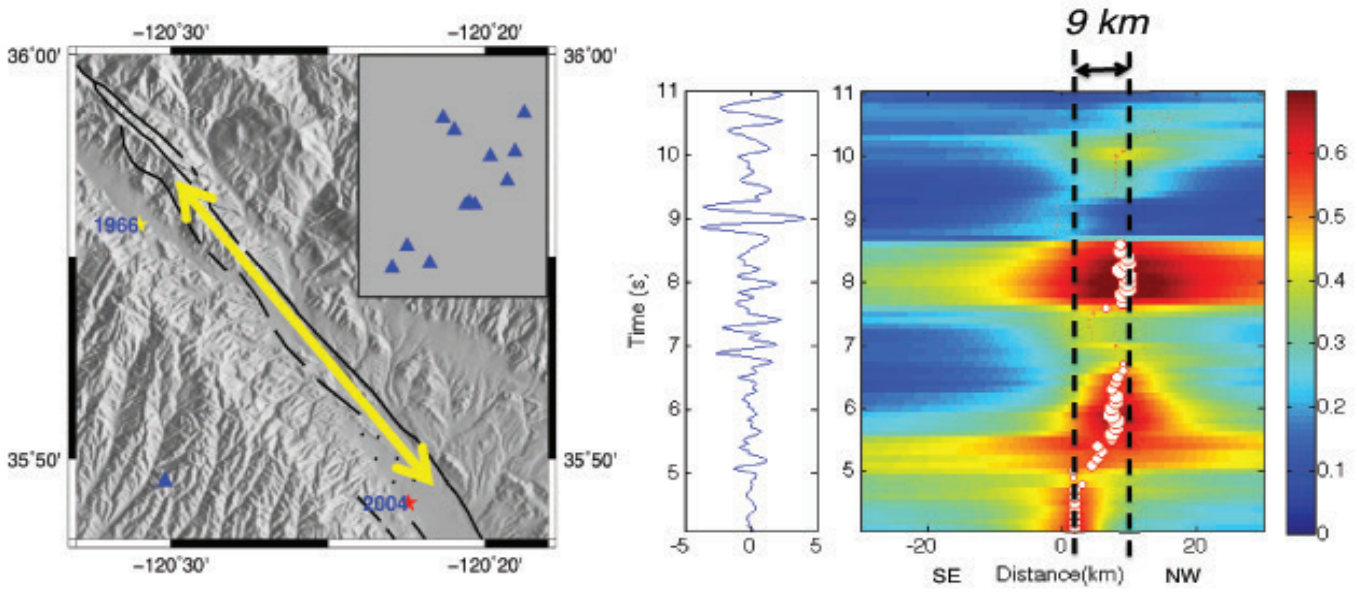

Figure 2.34.2: Array analysis of the 2004 *M*6 Parkfield earthquake. Left: mapview of the Parkfield area. The yellow arrows mark the approximated region of the rupture. The yellow and red stars are the epicenters of the 1966 and 2004 event, respectively. The blue triangle is the location of the UPSAR array with the distribution of the stations in the inset map. Right: stacked correlation coefficient as a function of along-strike position with respect to the hypocenter and time after P wave arrival is shown in color. T he white dots are the peak location in each time frame sized by the correlation coefficient. The black dashed lines mark the beginning and end of the HF energy source which gives a rupture size estimate of 9 km.

the UPSAR array. The earthquake is dominated by a unilateral rupture along the San Andreas Fault towards the northwest. The rupture is composed of three subevents that radiated strong high frequency signals. The first subevent is close to the hypocenter.

The two later subevents are closely spaced in the along-strike location near the end of the rupture. The interpretation is that these two subevents might occur at different depths consistent with the bimodal distribution of the aftershocks. In addition, we find that the dipping layer beneath the array causes the bias of the back azimuth and thus rupture length. After corrections, the estimated rupture length of 9 km is consistent with the distance between the two main subevents identified by back-projection using all local stations.

Conclusion

We explored the possibility of using seismic array processing in real time and developed an efficient methodology for rapid characterization of the earthquake rupture directivity and of the rupture area extent, using a correlation-stacking method. The strategy we propose can potentially prompt more reliable earthquake early warnings for large earthquakes. In terms of the future work, the optimal design of the array geometry and position, and real-time implementation strategy need to be further investigated.

Acknowledgements

We thank Pablo Ampuero for his constructive discussions and suggestions. This work is funded by the Earthquake Early Warning grant of U.C. Berkeley from the Gordon and Betty Moore Foundation.

References

Colombelli, S., Allen, R.M., and Zollo, A., Application of real-time GPS to earthquake early warning in subduction and strike-slip environments, *J. Geophys. Res. Solid Earth*, 118, doi:10.1002/jgrb.50242, 2013.

Fletcher, J., Spudich, P., and Baker, L., Rupture propagation of the 2004 Parkfield, California, earthquake from observation at the UPSAR, *Bull. seism. Soc. Am.*, 96, S129–S142, 2006.

Hoshiba, M., Iwakiri, K., Hayashimoto, N., Shimoyama, T., Hirano, K., Yamada, Y., Ishigaki, Y., and Kikuta, H., Outline of the 2011 off the Pacific coast of Tohoku earthquake (Mw 9.0)—Earthquake early warning and observed seismic intensity, *Earth Planets Space*, 63(7),547–551, 2011.